PHOTO-ELECTRON MOMENTUM DISTRIBUTION AND ELECTRON LOCALIZATION STUDIES FROM LASER-INDUCED ATOMIC AND MOLECULAR DISSOCIATIONS

by

DIPANWITA RAY

B. Sc., Calcutta University, India, 2001
M. Sc., Pune University, India, 2003

AN ABSTRACT OF A DISSERTATION

submitted in partial fulfillment of the
requirements for the degree

DOCTOR OF PHILOSOPHY

Department of Physics
College of Arts and Sciences

KANSAS STATE UNIVERSITY
Manhattan, Kansas
2010

Abstract

The broad objective of ultrafast strong-field studies is to be able to measure and control atomic and molecular dynamics on a femtosecond timescale. This thesis work has two major themes: (1) Study of high-energy photoelectron distributions from atomic targets. (2) Electron localization control in atomic and molecular reactions using shaped laser pulses.

The first section focuses on the study of photoelectron diffraction patterns of simple atomic targets to understand the target structure. We measure the full vector momentum spectra of high energy photoelectrons from atomic targets (Xe, Ar and Kr) generated by intense laser pulses. The target dependence of the angular distribution of the highest energy photoelectrons as predicted by Quantitative Rescattering Theory (QRS) is explored. More recent developments show target structure information can be retrieved from photoelectrons over a range of energies, from $4U_p$ up to $10U_p$, independent of the peak intensity at which the photoelectron spectra have been measured.

Controlling the fragmentation pathways by manipulating the pulse shape is another major theme of ultrafast science today. In the second section we study the asymmetry of electron (and ion) emission from atoms (and molecules) by interaction with asymmetric pulses formed by the superposition of two colors (800 & 400 nm). Xe electron momentum spectra obtained as a function of the two-color phase exhibit a pronounced asymmetry. Using QRS theory we can analyze this asymmetric yield of the high energy photoelectrons to determine accurately the laser peak intensity and the absolute phase of the two-color electric field. This can be used as a standard pulse calibration method for all two-color studies. Experiments showing strong left-right asymmetry in D^+ ion yield from D_2 molecules using two-color pulses is also investigated. The asymmetry effect is found to be very ion-energy

dependent.

PHOTOELECTRON MOMENTUM DISTRIBUTION AND ELECTRON LOCALIZATION STUDIES FROM LASER-INDUCED ATOMIC AND MOLECULAR DISSOCIATIONS

by

Dipanwita Ray

B. Sc., Calcutta University, India, 2001
M. Sc., Pune University, India, 2003

A DISSERTATION

submitted in partial fulfillment of the
requirements for the degree

DOCTOR OF PHILOSOPHY

Department of Physics
College of Arts and Sciences

KANSAS STATE UNIVERSITY
Manhattan, Kansas
2010

Approved by:

Major Professor
Prof. Charles Lewis Cocke

Copyright

Abstract

The broad objective of ultrafast strong-field studies is to be able to measure and control atomic and molecular dynamics on a femtosecond timescale. This thesis work has two major themes: (1) Study of high-energy photoelectron distributions from atomic targets. (2) Electron localization control in atomic and molecular reactions using shaped laser pulses.

The first section focuses on the study of photoelectron diffraction patterns of simple atomic targets to understand the target structure. We measure the full vector momentum spectra of high energy photoelectrons from atomic targets (Xe, Ar and Kr) generated by intense laser pulses. The target dependence of the angular distribution of the highest energy photoelectrons as predicted by Quantitative Rescattering Theory (QRS) is explored. More recent developments show target structure information can be retrieved from photoelectrons over a range of energies, from $4U_p$ up to $10U_p$, independent of the peak intensity at which the photoelectron spectra have been measured.

Controlling the fragmentation pathways by manipulating the pulse shape is another major theme of ultrafast science today. In the second section we study the asymmetry of electron (and ion) emission from atoms (and molecules) by interaction with asymmetric pulses formed by the superposition of two colors (800 & 400 nm). Xe electron momentum spectra obtained as a function of the two-color phase exhibit a pronounced asymmetry. Using QRS theory we can analyze this asymmetric yield of the high energy photoelectrons to determine accurately the laser peak intensity and the absolute phase of the two-color electric field. This can be used as a standard pulse calibration method for all two-color studies. Experiments showing strong left-right asymmetry in D^+ ion yield from D_2 molecules using two-color pulses is also investigated. The asymmetry effect is found to be very ion-energy

dependent.

Table of Contents

List of Figures

Acknowledgments

I can not start my thesis without acknowledging the valuable contribution of a number of people. I owe a lot to each of them.

I have no words to express my sincere gratitude to my thesis advisor, Prof. Lew Cocke. He was much more than just an advisor. Throughout the last 6 years at the Kansas State University, he has guided me through each and every aspect of a graduate student career: from patiently explaining the basic concepts of quantum mechanics to meticulously demonstrating how to troubleshoot a real life experiment. He has taught me how to think like a physicist. He has also sent me to a number of conferences/workshops and encouraged me to participate in large collaborative efforts.

I would like to thank Prof. Igor Litvinyuk for being there throughout my Ph.D. career. He has always been available for stimulating discussions. He has taken keen interest in my research work and has been a huge support. I am grateful to him for being patient in clarifying my doubts, making suggestions for troubleshooting or improving the experiment and all the general friendly advice.

It is not possible to talk about collaborative efforts without mentioning Prof. Matthias Kling, who has played a very important role in my graduate career. I have learnt a lot from the myriad long and fruitful scientific discussions with him. Working with him in the lab also helped me improve my experimental skills. His collaboration has made it possible for me to get exposure to one of the modern detection systems, the Velocity Map Imaging.

One cannot be successful in advanced research without a thorough understanding of the fundamental concepts in the field. The graduate coursework at KSU was ideal for the same, especially the courses offered by Prof. Brett Esry. His AMO courses gave me an opportunity to learn the ABC's of this field and prepared me well for further research. In the following years, whenever I had trouble with some theoretical concepts, I could always count on him as he was always welcoming and happy to help me out.

I would like to thank all the members of our group whom I have worked with during my stay at KSU - Irina Bocharova, Ali Alnaser, Maia Magrakvelidze, Chakra Maharjan, Predrag Ranitovic, Ben Gramkow, Wei Cao, Sankar De and Kamal Singh. It has been great experience to work with all these people, inetract and support each other in our individual projects. I would specially like to thank Dr. Ali Alnaser for the fantastic interaction over the few weeks we worked together. I was lucky to have him around to get me oriented in the lab atmosphere, teach me the basics of COLTRIMS experiments and data analysis. His vast knowledge base, ability to communicate and motivate through physics discussions, and fantastic training capabilities are aspects that I would like to draw inspiaton from in my future postdoctoral career. Towards the end of my career it was great to have Sankar De join the group as Prof. Igor Litvinyuk's postdoctoral fellow. I would like thank Sankar De for being such a great colleague and the support I have received from him in my work. He has been fantastic in designing and assembling the VMI chamber. His expertise with the VMI and also his constant efforts to improve the system has enabled me to carry out some of the experiments described in this thesis. The experience I have gained by working with him, on the collaborative efforts beyong my own thesis work has been tremendous. I would like to thank Irina for being there all along as a great friend and support.

None of the experimental efforts discussed in the thesis would have been possible without the help and support of the KLS group, its past and present members. Prof. Zenghu Chang and his group has been extremely efficient and proactive at maintaining and providing us the best possible laser source for our experiments. Starting from tuning and optimizing the laser for our use to being 'on call' round the clock for solving any glitch has made it possible for us to do our experiments. Special thanks to Chengquan Li, Eric Moon, Hiroki Mashiko, Steven Gilbertson and Wang He. I would like to thank Hiroki for all the support and the interactions which enabled me to design and plan out different optics setup from my experiments.

I would like to thank the AMO theory group without whose help none of the work would

have been possible. This thesis work is majorly based on the theoretical findings of Prof. C. D. Lin and his group: A. T. Le, T. Morishita and Z. J. Chen. Prof. Uwe Thumm and F. He has been very supportive and their work has enabled us to get insight into some of our experimental results. I would like to thank Fatima Anis for being a great help throughout my career.

I would also like to thank all the lab stuff and JRM personnel: Al Rankin, Scott Chainey, Bob Krause, Mike Wells, Russ Reynolds, Kevin Carnes and Vince Nidham. They have been extremely helpful, and supportive.

I would like to express my sincere thanks to Prof. Matthias Kling, Prof. Brett Esry, Prof. Stephen Dyer, and Prof. Ryszard Joukowiak for kindly agreeing to be in my thesis committee. I sincerely appreciate their time commitment and valuable advices.

I would like to thank my parents and sister without whose support I could not have realized my dreams. I would like to thank my close friends and family here and back in India for all their love and support.

Chapter 1

Introduction

1.1 Motivation

The general motivation for pursuing ultrafast strong-field study of atoms and molecules is to gain fundamental understanding of the dynamics, the intermediate processes involved, and internal structures. A large number of practical applications of the laser-matter interaction, e.g. precision fabrication, lithography etc., can benefit from such studies. However the main objective of this work is to contribute towards the fundamental knowledge base.

The development of laser technology over the last decade has rapidly opened up possibilities of new studies. Commercially available Ti:Sapphire laser systems are now capable of providing laser pulses with very high intensity and ultrashort duration. The electric field strength of such a pulse is comparable to that which binds the valence electrons of atoms (5 $\times$ 10^9 V/cm) thus allowing the laser to interact, excite, ionize or manipulate these valence electrons. The huge intensities that can be reached by focusing the laser pulse has brought to light several intriguing non-linear processes that have drawn considerable attention. The availability of pulses with less than sub-10 fs duration has opened up the area of high precision time resolved studies of processes that occur on such timescales, such as molecular vibrational and rotational dynamics. Time resolved study is however not the focus of the work presented in this thesis. As we demonstrate, all the studies that are discussed in the following chapters can be carried out with much longer pulses. Some of the experiments

described do use sub-10 fs pulses, but we later show that similar results are obtained with longer pulses. An additional significance of the short pulse duration in our case is that it squeezes the entire pulse energy into a very short time giving rise to exceptionally large electric field strengths. A systematic study of the processes under investigation in this work and their outcomes as a function of the pulse duration can however be an interesting aspect worth investing some effort to understand.

1.2 Background

When atoms or molecules are subjected to laser pulses of intensity $I > 10^{11}$ W/cm^2, non-linear processes can come into play. Depending on the strength of the laser a single electron can be ionized or multiple ionization may occur. A major part of the work in this thesis focuses on single ionization of atoms and subsequent manipulation of the ionized electron in the laser field to effectively probe the target ion.

The single ionization can occur via a variety of of ionization mechanisms with labels which include "multi-photon" [1,2], "above-threshold" [3], "tunneling" and "over-barrier" [4] . The standard IR laser used (central wavelength of 800nm) has a single photon energy of $\hbar\omega = 1.55eV$ which is not sufficient to overcome the ionization potential I_p of most atoms and molecules. Thus a single photon of the laser pulse cannot put a valence electron into the continuum. If the laser field strength is strong enough, the valence electron can, however, absorb more than one photon, providing an energy sufficient, or in excess of that required, for ionization. This former is known as multi-photon ionization. The latter, called the above-threshold ionization (ATI), was first brought to light by Agostini *et al.*[3]. These experiments recorded photoelectron energy spectra exhibiting peaks separated by the photon energy ($\hbar\omega$) appearing at the energies $E = n\hbar\omega - I_p$, the typical signature of the ATI process. At intensities of 10^{13} W/cm^2 or above the laser electric field can distort the Coulomb potential to such an extent that a barrier potential of finite width is formed enabling the electron to tunnel out.

This phenomenon is known as tunneling ionization and was first analyzed by V. Keldysh[5]. He showed that strong-field ionization mechanisms can be characterized quantitatively by the Keldysh parameter given as:

$$\gamma = \sqrt{\frac{I_p}{2U_p}} \tag{1.1}$$

where I_p is the ionization potential and $U_p = I/4\omega^2$ is defined as the cycle averaged energy of the electron in the electric field of the laser pulse. For $\gamma >> 1$ the ionization is said to proceed through multiphoton ionization, while for $\gamma < 1$ the ionization is said to be dominated by tunneling ionization. This condition indicates that tunneling ionization is favored at low frequencies of the laser field. The ionization rate as derived by Amosov, Delane and Krainov[6], the well-known as ADK-rate, is given as:

$$P_{ADK} = \left[\frac{3e}{\pi}\right]^2 \frac{Z^2}{3n^{*3}} \frac{2l+1}{2n^*-1} \left[\frac{4eZ^3}{(2n^*-1)n^{*3}E}\right]^{2n^*-3/2} exp\left[-\frac{2Z^3}{3n^{*3}E}\right] \tag{1.2}$$

where $n^* = \sqrt{2I_p}$, E is amplitude of the electric field of the laser pulse, Z is the atomic/ionic charge, l is the orbital angular momentum quantum number and e is the electronic charge. Many theoretical calculations discussed in the following chapters for ionization of atoms and also for diatomic molecules have been ADK-rate weighted.

1.3 Focus

The work presented in this thesis has two major themes under the common heading of "controlling the electronic wave packet". The goal of the first theme is to use the electron singly ionized from an atomic target to acquire electron diffraction images of the target ion. The oscillating property of the electric field of the laser is utilized to make the ionized electron in the continuum return to the ion core and diffract from it via elastic rescattering. We investigate the possibility of extracting target structure information from such electron diffraction images. In order to do this we have to understand the rescattering of the electrons. Ch 3 deals with study of experimental diffraction images from atomic targets and analysis of the

target structure by comparison with theoretical calculations involving quantitative treatment of rescattering of electrons[7].

The second theme is to control the development of the electronic wave packet by manipulating the shape of the laser field. By shaping the laser field asymmetrically, electrons ionized from atoms can be made to eject preferentially to the left or right along the laser polarization, thus modifying the diffraction image discussed above. In this thesis we study how this modification depends on the asymmetry of the laser field. Finally the same shaped laser pulse can be used to influence the evolution of the bound state electronic wave packet. We do this through a study of the direction in which an ion is ejected from a molecular dissociation. When a simple hydrogen molecule is singly ionized, the remaining excited electron is initially a delocalized wavepacket moving in the field of two dissociating protons. This wave packet ultimately becomes localized on one or the other proton at end of the dissociation process. Which proton it chooses can be manipulated by controlling the shape of the laser pulse. The first of the two studies is described in Ch 4 and the second in Ch 5. Ch 2 describes the main experimental setups and techniques used in this thesis work.

Chapter 2

Experimental technique

2.1 Introduction

This chapter provides an overview of all the experimental setups and techniques used in the work presented in this thesis. The major components in any laser-matter interaction experiment consist of: (a) A laser source and associated optics to optimize and control the laser pulses, (b) A reaction chamber maintained at high vacuum hosting a source for the gas target and a charged fragment detection system. The following sections present each of these components.

2.2 Laser and optics

In order to study atomic and molecular dynamics it is necessary to provide adequate energy for ionization, dissociation or any other process we wish to observe. Also to do a time resolved study it is vital that the excitation of the probe have a very short duration. An ultrafast laser pulse provides a very effective energy source for doing time resolved strong field studies. The laser used in all our experiments are generated in the Kansas Light Source (KLS) of the J.R. Macdonald Lab. A Ti:Sapphire oscillator-amplifier combination is used to generate 1-1.5 KHz, 2 mJ, 40 fs laser pulse with central wavelength at around 800 nm. The oscillator consists of a Ti:Sapphire crystal pumped by CW laser. The creation of standing waves within the resonating cavity generates discrete frequencies (modes of oscillation).

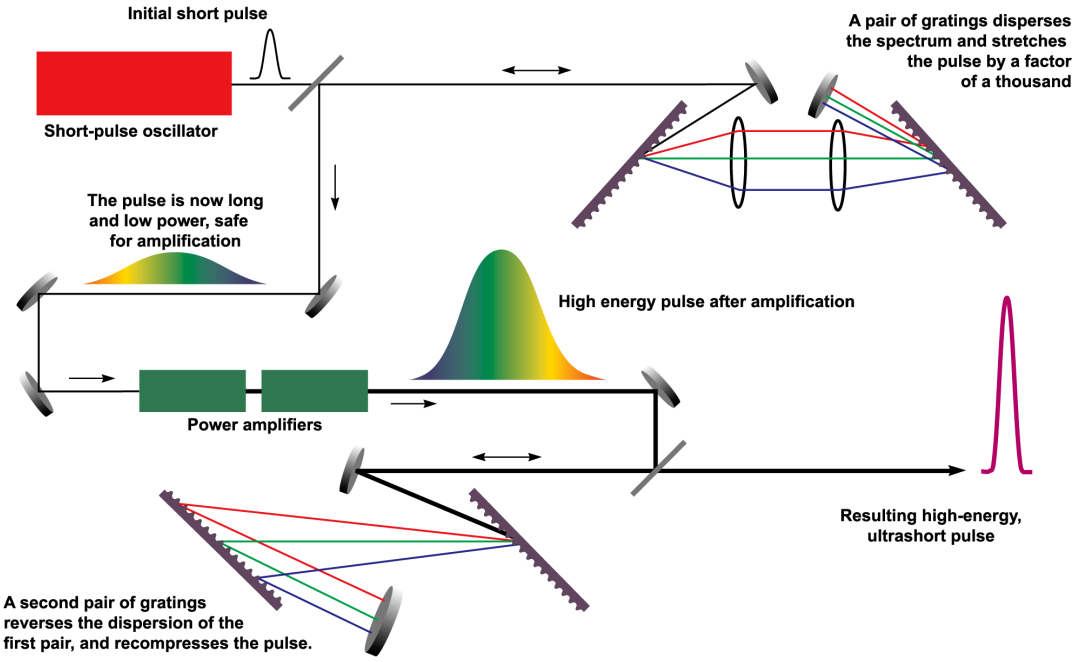

Figure 2.1: *Schematic diagram depicting the principle of the chirped pulse amplification method. The oscillator provides the seed pulse which is first stretched in time to lower the peak intensity of the pulse. Then the pulse undergoes amplification by multiple passage through a Ti: Sapphire crystal. Finally the pulse is compressed to generate a 2mJ 40 fs laser pulse. [Figure Source: http : //en.wikipedia.org/wiki/Chirped_pulse_amplification]*

The mode separation is inversely proportional to the cavity length. The phases of these modes are initially incoherent, but certain methods are used to lock the phases together. This is called "mode-locking". A Pockel cell is used to electro-optically Q-switch this beam, generating a pulsed output beam. This output is passed through a stretcher to create a low power pulse which is stretched out in the time domain. This pulse is used as the input (seed) pulse for the amplifier, as it has been rendered safe to amplify without causing damage to the amplifier crystal. The amplifier consists of a cryogenically cooled Ti:Sapphire crystal. The stretched mode-locked seed pulse from the oscillator gets amplified by undergoing multiple passes (total 14 passes) through the gain medium and is subsequently compressed by a grating-compressor into a 2 mJ 40 fs pulse. Fig 2.1 outlines the different steps of the laser pulse production as described above.

2.2.1 Pulse shortening with hollow core fiber

Some experiments require sub-10 fs duration. To shorten the amplifier output pulse further from 40 fs to 6-8 fs the beam is focused into a hollow core fiber filled with rare gas - Ar or Ne. A mirror/lens with very long focus ($\sim$ 1 m) is used to focus the laser beam into a fiber capillary with inner diameter of 250 μm through a 0.5 mm anti-reflection coated fused silica window. A similar window also seals the exit of the fiber. The fiber acts as a waveguide while the gas acts as the medium for the nonlinear process called self phase modulation resulting in spectral broadening. The fiber is aligned using vertical and horizontal (side-wise) translational controls at the two-ends of the fiber to get the optimum clean round TEM_{00} mode output. A 60-70% transmission ratio after fine tuning the alignment is considered a good input-output coupling of the fiber.

The degree of nonlinearity depends on the gas pressure (the Ne pressure is usually maintained at 25 psi for the experiments discussed in Ch 3). The nonlinearity of the medium is due to the dependence of its refractive index (r.i.) on the laser intensity. The nonlinear r.i. generates new frequency components as the beam propagates through the medium. A phase shift is generated proportional to the time-dependent nonlinearity of the r.i. and also the amount of path the beam propagates through the medium. This generates the additional frequencies. The time derivative of this phase shift accounts for the positive chirp of the pulse. The leading edge of the pulse shows a red shift while the trailing edge is blue shifted. The output pulse from the fiber therefore has undergone a spectral broadening and has a large positive chirp.

The fiber output beam is collimated using a spherical mirror. The chirped pulse is compressed by introducing negative group velocity dispersion (GVD) by reflecting it from a set of "chirp mirrors' (7 Femtolaser and 4 Layertec pairs). The chirp mirrors are basically multi layered mirrors such that the wavelength corresponding to red light reflects from deeper

layers while the blue wavelength reflects from outer layers. Each mirror introduces a GVD of -30 fs^2 for a laser pulse centered at 800nm. It is a common practice to overcompensate the chirp of the pulse in order to account for the additional dispersion of the short pulse when it propagates through air and other optics to the interaction chamber. Any excess negative chirp is compensated to optimize the pulse duration using compensating fused silica plates or variable thickness wedge plates.

2.2.2 Ge plates

Many of our experiments demand a good control of the different laser parameters in order to do an extensive study and achieve a clear understanding of the process in question. The laser intensity is one such important parameter. The most common method of controlling the intensity is to transmit the laser pulse through a gradient absorption-type or reflection-type filter to control the total transmitted power. For absorption-type filters (ND filters) care has to be taken to avoid beam profile distortion by nonlinear processes occurring in the filter due to the large energy absorption. In the case of few-cycle pulses, as described in Sec 2.2.1, passing through any optical component such as filters causes positive dispersion, thereby making the pulse longer. This poses a serious problem in short pulse experiments. In order to overcome this issue, we have devised an alternative method of intensity control in which the intensity is manipulated by reflecting the pulse instead of transmitting it through filters. We use a pair of polished Ge plates parallel to each other. The laser is incident on it very close to Brewster's angle (about 10 °). At this angle, only the s-polarization is reflected and thus the plates serve as a polarization filter. The intensity is controlled by rotating the plane of polarization of the beam incident on the plates. Ge was chosen as it has the least variation in r.i. over the broad wavelength range of a 5 fs pulse and also has very high reflectivity. The incidence at Brewster's angle also ensures selective reflection of only one component of linear polarization, thus eliminating any possible ellipticity present in the beam.

2.2.3 Two-color setup

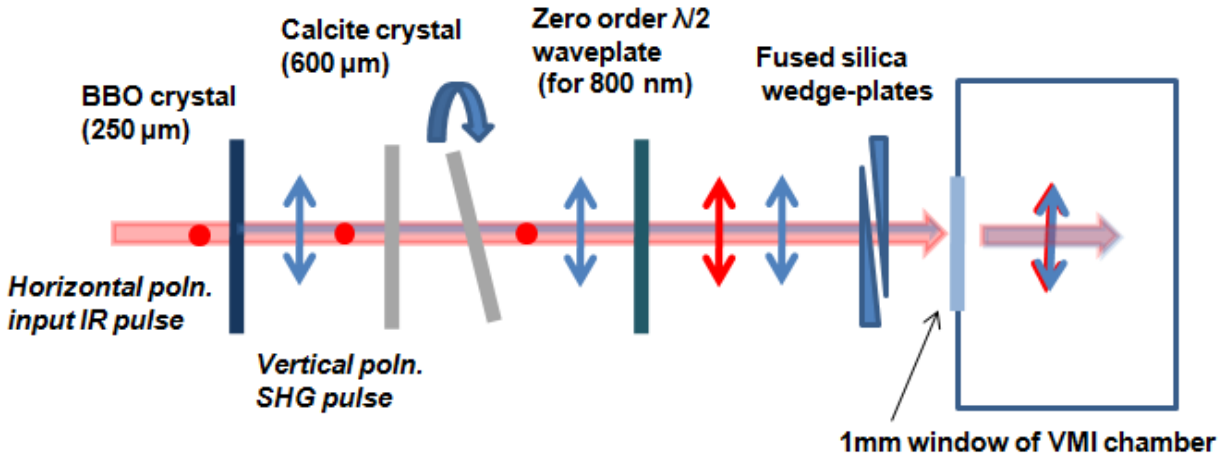

Figure 2.2: *Schematic diagram of collinear two-color setup. When the horizontally polarized IR (800 nm) pulse is incident on the BBO crystal, the second harmonic (SH) (400 nm) pulse is generated with polarization orthogonal to the IR. The quartz half-waveplate rotates the IR pulse to vertical but acts as a full-waveplate for the SH. The birefringent calcite crystal is used to over-compensate for the delay generated between 800-400 nm pulses by all other optics. The variable thickness wedge-plates exactly optimize the relative delays and overlap the two pulses at interaction point. The phase ϕ of the two-color pulse is controlled by rotating one calcite crystal.*

In Ch 4 and Ch 5 we discuss experiments which involve controlling the shape of the laser pulse, i.e., manipulating the electric field shape as a function of time. An effective yet simple way of realizing this control is by combining the 800 nm pulse with its second harmonic 400 nm pulse. This is a technique employed for over a decade[8]. The optics includes: (a) a 250 μm $\beta-$Barium Borate (BBO) crystal, (b) two pieces of 600 μm thick Calcite crystal, (c) a zero-order $\lambda/2$ plate for 800 nm wavelength, and (d) a pair of wedges.

We adapt a collinear configuration for the two-color setup [Fig 2.2]. The 45 fs, 800 nm (IR) pulse from the amplifier output with horizontal polarization is passed through the BBO crystal which generates a second harmonic 400 nm component due to its nonlinear properties. The crystal is cut in a way to ensure that the optic axis has a 29 $^\circ$ tilt with the surface on which the laser is incident. This optimizes the second harmonic generation for

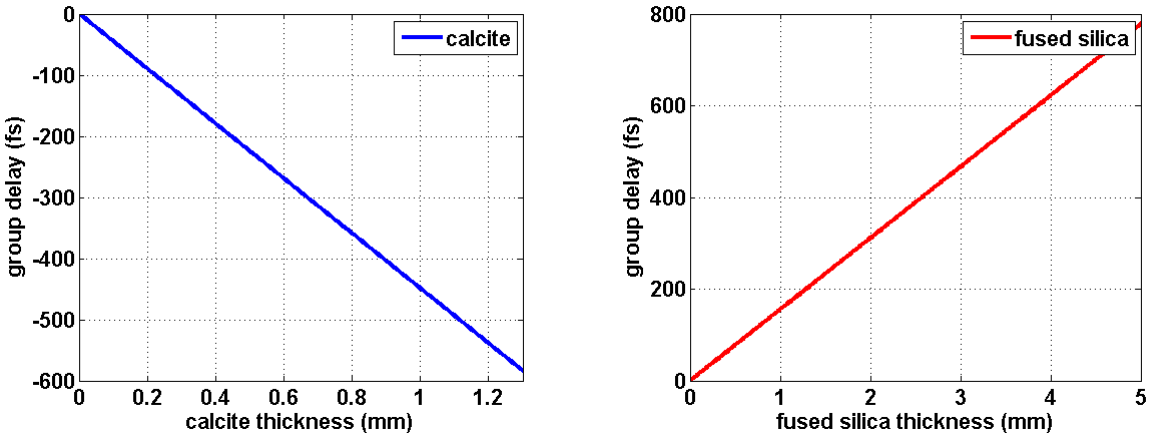

Figure 2.3: *Plots of the group delay generated between the 800 nm and 400 nm pulses on traversing different optical materials: (a) The left panel shows the group delay in a (birefrengent) Calcite crystal oriented such that the shorter(longer) wavelength travels on the faster(slower) axis; (b) The right panel shows the group delay in fused silica which is an isotropic medium.*

800 nm wavelength when the pulse is incident with the polarization along the optic axis. The SH pulse is generated with its polarization orthogonal to the IR polarization, and is also delayed from it by about 60 fs. Due to the difference in the group velocity dispersion of the IR and the SH pulse, the delay between the two pulses keeps increasing (the IR pulse generally travels faster than the SH) as they pass through different optics. In order to compensate for this delay and make the two pulse envelopes eventually overlap in time at the interaction region, the two calcite crystals are introduced in the laser path. The calcite is a negative birefringent crystal, so it has different refractive indices along the ordinary (slow) and extraordinary (fast) axes. The fact that the two pulses are orthogonally polarized is utilized to over-compensate the delay between the two pulses by passing the SH pulse along the fast axis and the IR along the slow. Both pulses are subsequently passed through the zero-order quartz plate which acts as half wave-plate for IR and rotates its polarization by 90°, but acts as full wave-plate for SH. So the beam exiting the quartz plate has both components with polarization along the vertical direction. In order to make the two pulses exactly overlap at the interaction region, a pair of variable thickness fused silica waveplates

are used to exactly compensate for the excess negative time delay from the calcite. In order to vary the shape of the two-color pulse the relative phase between the 800nm and 400 nm carrier pulses is controlled by rotating one of the calcite crystals about an optical axis using a motorized rotation stage in steps of 0.05 fs.

A first-principles calculation of the group delays in the calcite and fused silica [Fig 2.3] allows us to calculate the required thickness of each optical component. The refractive indices are calculated using Sellmeier's equation. Apart from the BBO crystal which generates +60 fs ('+' implies IR ahead of SH), the 1 mm window at the entrance of the chamber also adds +160 fs delay, and the waveplate adds about +40 fs. The two calcite crystals at normal incidence generate a total of about -540 fs. The rest of the negative delay is compensated by 1.7 mm of wedge plate thickness. The spatial walk-off is neglected in this calculation, but still enables us to roughly predict the optics combination.

The two-color absolute phase control is done by scanning the calcite crystal, thus scanning the IR-SH phase delay. The rotation of the crystal away from normal incidence introduces added optical path for the two pulses in the calcite, but it needs to be noted that the thickness and therefore the delay is not a linear function of the rotation angle; it is a quadratic function. The rotation stage was programmed to move in steps of equal time delay. The phase convention used in all discussions is such that the absolute phase $\phi = 0$ when the electric field is maximum towards positive z-direction. The absolute phase calibration is done using the results from Ch 4.

This collinear design has the limitation that the SH pulse intensity cannot be controlled separately. The alternative would be to use an interferometric configuration. However, apart from this constraint, which does not pose a serious problem in our experiments, the present setup produces an effective two-color pulse with robust and reproducible pulse shape control.

The next component in the setup is the interaction chamber: In our case either (i) a Stereo-ATI phasemeter or (ii) a Velocity-Map Imaging Spectrometer (VMI). The interaction chambers are vacuum tight chambers with very low gas-pressures inside. The laser is focused onto the target gas inside this chamber, and the fragments from the interaction are imaged. A detailed description of the two spectrometers is presented in the following sections.

2.3 Stereo-ATI Phasemeter

The Stereo-ATI phasemeter (Fig 2.4) was developed by G.G.Paulus[9] a decade ago with in order to measure asymmetric electron emission from CEP (Carrier-Envelope Phase) stabilized pulses (explained in Ch 4).

The Strereo-ATI phasemeter has the following major components as shown in Fig 2.5:

(a) Gas cell and laser propagation tube

(b) Spectrometer: Flight tube and detector assembly

(c) Pump stage

The most important component of this compact apparatus is a pair of identical 40mm micro channel plate detector assemblies (MCPs) placed symmetrically across from a gas cell facing towards each other. The cubic gas cell at the center has a 2 mm$\times$0.5 mm vertical slit on opposite surfaces each facing a detector. A 2 mm cylindrical hole connects the other two faces of the cube (the top and bottom face). The cell is exactly centered such that the slits are centered on the axis normal to the detector front surfaces. It is held in place by press-fitted groove connections with 1 inch diameter stainless steel tubes running perpendicular to the detector-axis and horizontal to the surface of the optics table. This 1 inch tube acts as the laser propagation path and the outer end has a 0.5 mm thick anti-reflection-coated fused silica window at the beam entrance end and a similar 1 mm window at the exit end. A gas line connected to the exit side of the laser tube supplies the target gas and maintains the 'gas cell- laser tube' enclosure at a desired pressure controlled by a needle valve.

The laser beam is aligned through the laser tube and is focused inside the gas cell with

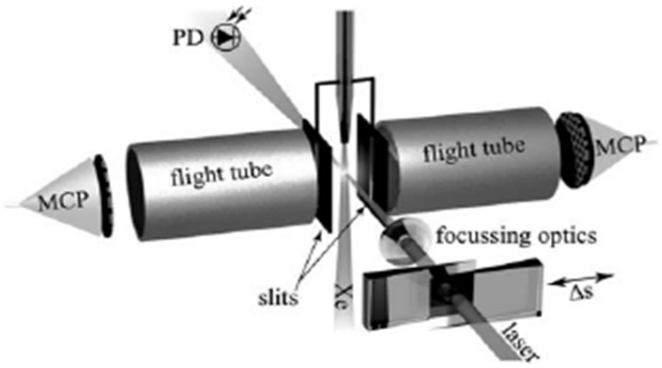

Figure 2.4: *Schematic diagram of Stereo-ATI phasemeter. Ref: M. G. Schatzel et. al., Appl. Phys. B, 79, 1021-1025 (2004)*

a silver coated spherical mirror of focal length 25 cm placed outside the entrance window. The laser ionization produces electrons that pass through the slits in the gas cell and fly towards the two detectors. Each detector front face is 15 cm away from the interaction point. These 15 cm long flight electron flight paths are shielded by μ-metal tubes which renders the interior free of the earth's magnetic field. A grounded mesh at the end of the μ-metal tube ensures that there is no electric field acceleration in the flight tube. A second mesh between the ground mesh and MCP front face can be biased at a small negative voltage to act as a repeller for electrons with very low energy.

The micro channel plates (MCPs) are time sensitive detectors. Each plate consists of an array of miniature electron multipliers oriented parallel to each other but at a small angle ($\sim 8^\circ$) to the axis normal to the plate surface. This angle ensures that each charged fragment reaching the plate hits the tube wall and sets off an avalanche of electrons, therefore amplifying the original signal by orders of magnitude. The MCPs in the phasemeter are assembled in a chevron configuration (V-shaped): the V-connotation comes from the fact that it consists of a pair of matched MCP-plates stacked together with the pores aligned to form a V-shape across the cross-section. The detector assembly also consists of an anode plate placed behind the back-MCP. In order to bias the detector to collect an electron signal, the front plate is maintained at +100 V, the back plate at about +1900 V and the anode

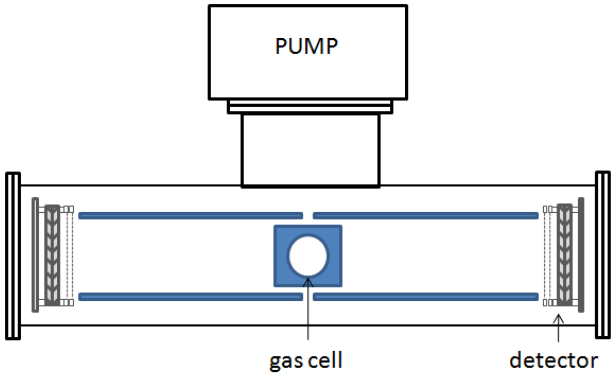

Figure 2.5: *Schematic of Stereo-ATI phasemeter: a cross-section view. The gas cell is situated at the center. The laser is focused into the gas cell through the laser propagation tube (not shown in diagram, perpendicular to plane of the page). The two MCP detectors are located on either ends. The flight paths in between the gas cell and the detectors are shielded by mu-metal tubes. A turbo pump placed above maintains the entire system below (10^{-8} Torr) when no target gas is present.*

plate at +2300 V.

To detect the fragments from the target gas ionization accurately the chamber has to be maintained under high vacuum. This gets more crucial in the case of electron detection since there is no way to differentiate between electrons from the target gas and from background gas. Also due to high voltage biasing of the detectors the pressure in the detector region needs to be maintained at 10^{-6} Torr or lower. The entire apparatus is maintained at high vacuum using a turbo-pump (speed 230 ℓ/s) connected to the T-arm above the gas cell. The turbo-pump is backed with a roughing pump to extract the residual gas load out of the vacuum system continuously. Under experimental conditions the gas cell has no direct opening to the pump except through the narrow slits. This allows us to maintain a high pressure (10^{-2} Torr) inside the gas cell assembly while the rest of the spectrometer is maintained at 10^{-6} Torr. This has the advantage over spectrometers using gas jets that we can use a very large target gas density, thereby producing a very high electron count rate. This is especially important for the measurement of rescattered electrons which are a small fraction of the total electron emission. A bypass connection from the gas cell assembly

to the pump stage across a valve allows us to dump the residual gas from the laser-target interaction in between data acquisitions. This helps to speed the flushing of the cell when switching target gases.

2.3.1 Event-mode data acquisition

The amplified signal from the back-MCP or the anode is first passed through a decoupling box (an R-C circuit which filters the AC signal from the DC biasing voltages). This device enables us to tune the impedance matching and minimize the reflections of the fast signal. The signal is then further amplified through a fast-amplifier and fed into a constant fraction discriminator (CFD) unit. Inside the CFD the incoming signal is duplicated, delayed by a fixed time, inverted and added to itself. A NIM signal (standard negative logic signals of 10 ns width and 1 V in size) is produced at the zero-level crossing of this resultant pulse. The timing of such a pulse is independent of the height of the original detector pulse. All the timing signals are measured with respect to a start signal (reference) for each laser shot. This reference signal is generated by a photodiode collecting scattered laser light in the input path before the laser is focused into the phasemeter.

All the timing signals are digitized using a 32-channel multi-hit Time-to-Digital Converter (LeCroy 3377 TDC). It has 0.5 ns timing resolution. Once initialized by the start signal the TDC records all the hits within a time-window of 32 μs. This is the maximum time-range per laser shot (event) over which the TDC can record hits and thus defines the maximum range of the time-of-flight spectrum. For electron acquisition the time-of-flight range needed is much shorter ($>$ 400 ns). The pulse-pair resolution of the TDC depends on the width of the raw signals from the detector. This is about 10 ns for most of our experiments and thus the TDC cannot resolve two electron hits separately unless they are separated by 10 ns from each other.

In case of the experiments discussed in Ch 3 care was taken to keep the number of hits of the highest energy electrons (rescattering electrons) to one or two per event. Also the gas

pressure in the cell for a given laser intensity was adjusted very carefully to avoid amplitude saturation of the pulses. If the average spacing of electron hits becomes less than 10 ns (very high count rates), a hole can develop in the spectrum due to the dead time of the CFD after the detection of a first hit.

The phasemeter was originally designed to measure one dimensional timeof-flight spectra. Usually the polarization of the incident laser beam is kept horizontal, that is parallel to the detector axis, since the laser ionizes preferentially along the polarization. In order to use this apparatus to acquire full momentum spectrum, an achromatic half-wave plate with a motorized dial is introduced in the beam and rotated in 1° steps. This rotates the polarization in steps of 2°. The electrons ejected at different angles with respect to the polarization are collected as a function of dial rotation. Knowing this dial angle for each recorded event, all the events are combined using the offline analysis to produce the full vector momentum spectrum.

2.3.2 Data analysis

The event-mode digitized data processed in the TDC is fed to the acquisition computer. The CAMAC-crate-to-computer interfacing is done by LabVIEW software (National Instruments product). LabVIEW also allows us to do online analysis and saves the data in binary format. Offline analysis is done using PAW analysis software developed by CERN. The LabVIEW designing and all the programs for offline analysis were originally written by Timur Osipov[10]. The program that does the final histogram plots has been modified as per requirement of the individual experiment.

The subroutine called "analysis" calls each event separately and the timeof-flight, momentum or energy information corresponding to all the hits in that event are stored as data points in the relevant histograms. In order to do the momentum or energy calculation, the parameters used in the experiments are entered in the program: flight distance, mass and

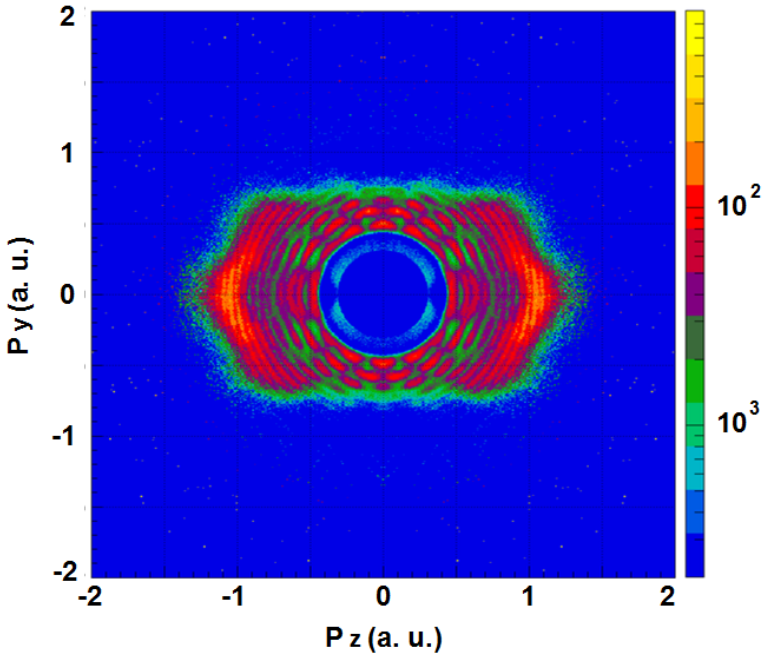

Figure 2.6: *Density plot showing the momentum distribution of electrons from Xe gas taken with the phasemeter. The laser used has peak intensity* 5×10^{13} W/cm^2 *and a pulse duration of 40 fs. The laser polarization is along z-axis, and the laser propagation direction is perpendicular to the momentum plane.*

charge of fragment. Knowing these parameters the momentum vector can be calculated:

$$p = \frac{ms}{t} \tag{2.1}$$

Here t is the time signal recorded by the MCP with respect to the photodiode start signal, m is mass of the fragment and s is the distance between the interaction region and the detector. A time-zero t_0 adjustment to the time information is incorporated to correct for the signal travel time through cables. The momentum components parallel and perpendicular to the polarization can be calculated knowing the angle between the polarization vector and the detector axis. The detailed momentum calculation and data analysis is discussed in Ch 3 for the relevant experiment. (The program code can be found in Appendix A.)

A typical momentum plot from Ar target is shown in Fig 2.5. The data is taken in the phasemeter using a 40 fs pulse . The laser propagation direction is normal to the plane of the

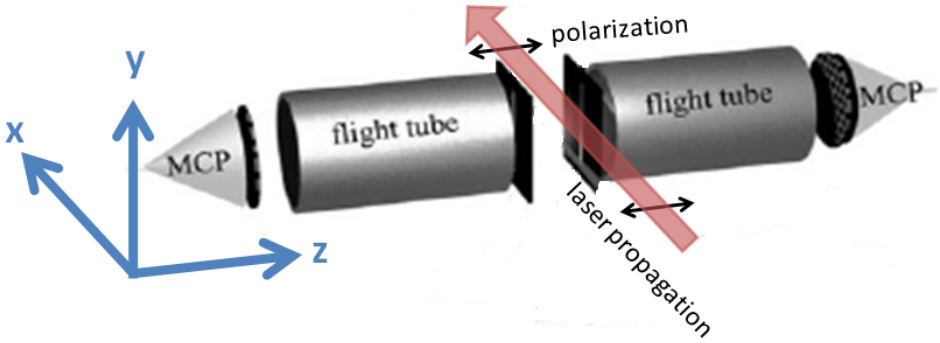

Figure 2.7: *Phasemeter diagram indicating the lab frame. The x-axis indicates laser propagation direction, and laser polarization is along z-axis. Modified from Ref: M. G. Schatzel et. al., Appl. Phys. B, 79, 1021-1025 (2004).*

momentum distribution. p_z is along the detector axis, ie along laser polarization direction. The co-ordinate convention followed in this plot and in all future discussions of phasemeter experiments is illustrated in Fig 2.7. The laser propagates along x-axis. The laser polarization is along z-direction which is also the detection axis. In case of two-color discussions $\phi = 0$ would mean the electric field is peaked along positive z-direction.

2.4 Velocity Map Imaging

The velocity map imaging technique (VMI) was disussed by Eppink and Parker[11]. The VMI spectrometer used for the experiments discussed in this thesis was built by S. De. This instrument measures the transverse components of the velocity of fragments created in the interaction region. It projects the transverse velocities of a 3D distribution onto a detection screen. The 3D distribution can be reconstructed based on the fact that it has cylindrical symmetry about some known axis. The detection principle of VMI, same as all detection spectrometers, involves the presence of an electric field to direct the fragments onto a detec-

tion screen. However the distinct feature of VMI is the presence of a non-uniform electric field which effectively acts as a weak electrostatic lens. The same vector velocities from different points in the interaction volume are mapped to the same radial position on the detector. Thus the lens removes any blurring due to the finite source size.

The exact ion-optics design and voltage assignments were determined by S. De using

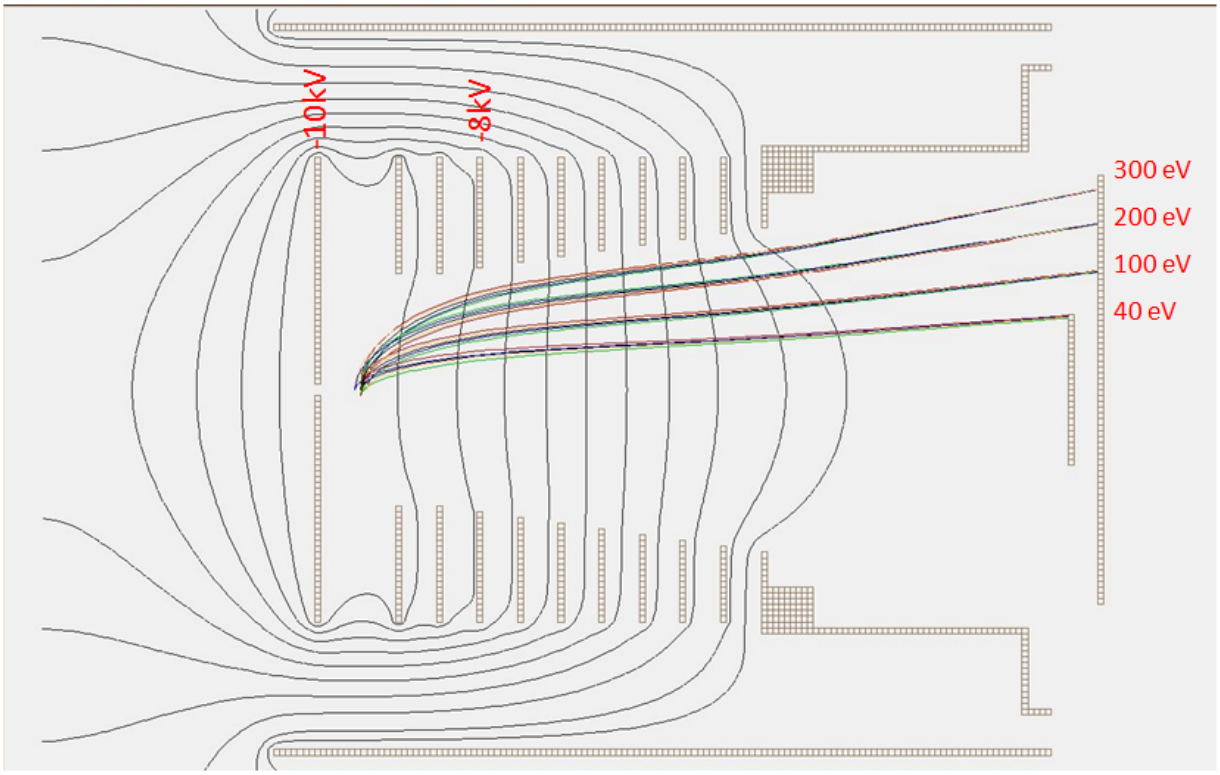

Figure 2.8: *The SIMION simulation of the multi-electrode VMI spectrometer showing the electric fields and the trajectories of the charged particles. Fragments ejected with different energies perpendicular to the spectrometer axis focus on the MCP-Phosphor assembly. The simulation shows that fragments emitted with the same energy, ejected perpendicular to the ion-optics axis and originating even 3 mm apart get focused to the same radius on the detector. The SIMION simulation is also used to establish the energy calibration of the spectrometer. credit: Sankar De, N. G. Johnson, A. Wirth.*

SIMION software. Given a certain configuration of electrodes with voltages and relevant particle initial conditions, SIMION solves Laplace's equations to calculate the electric fields and the trajectories of charged particles. The software can display fragment the flight paths

and the equipotential surfaces. Fig 2.8 shows the SIMION simulation for our multi-electrode VMI.

The simulation shows that fragments with different energies ejected perpendicular to the ion-optics axis fall at different radii on the detector. Similar fragments created even 3 mm apart having the same energy can be focused well to the same radius of the detector.

The VMI consists of:

(a) The ion-optics

(b) MCP-Phosphor assembly

(c) An effusive gas source

(d) A cooled camera

Fig 2.9 shows a schematic design with all the salient components mentioned above and an image of the ion-optics and detector assembly.

The VMI spectrometer is completely cylindrically symmetric and has three electrodes: a repeller, an extractor and a ground. The repeller is a flat circular plate with a small hole through which the target gas enters the chamber. The extractor is an annular flat plate followed by a similar ground plate electrode. The target gas flows in through the effusive jet on the repeller and a laser beam is focused on it in the gap between between repeller and extractor. Together the voltage combination on the repeller, extractor and ground form a weak converging electrostatic lens. The charged fragments formed in the interaction region fly apart rapidly at first and then are velocity focused onto the detector.

Our VMI follows a design by M. F. Kling but consists of a total of 11 (rather than 7 in the Kling design) electrodes including the repeller. The larger number of electrodes gives a better control over the field distribution along the spectrometer, has smoother field gradients and thus better energy resolution. The repeller voltage, when ramped up to 10 kV,can image fragments with energy per electronic charge as high as 300 V.

The target gas is supplied by an effusive gas jet. A $30\mu m$ aperture at the center of the

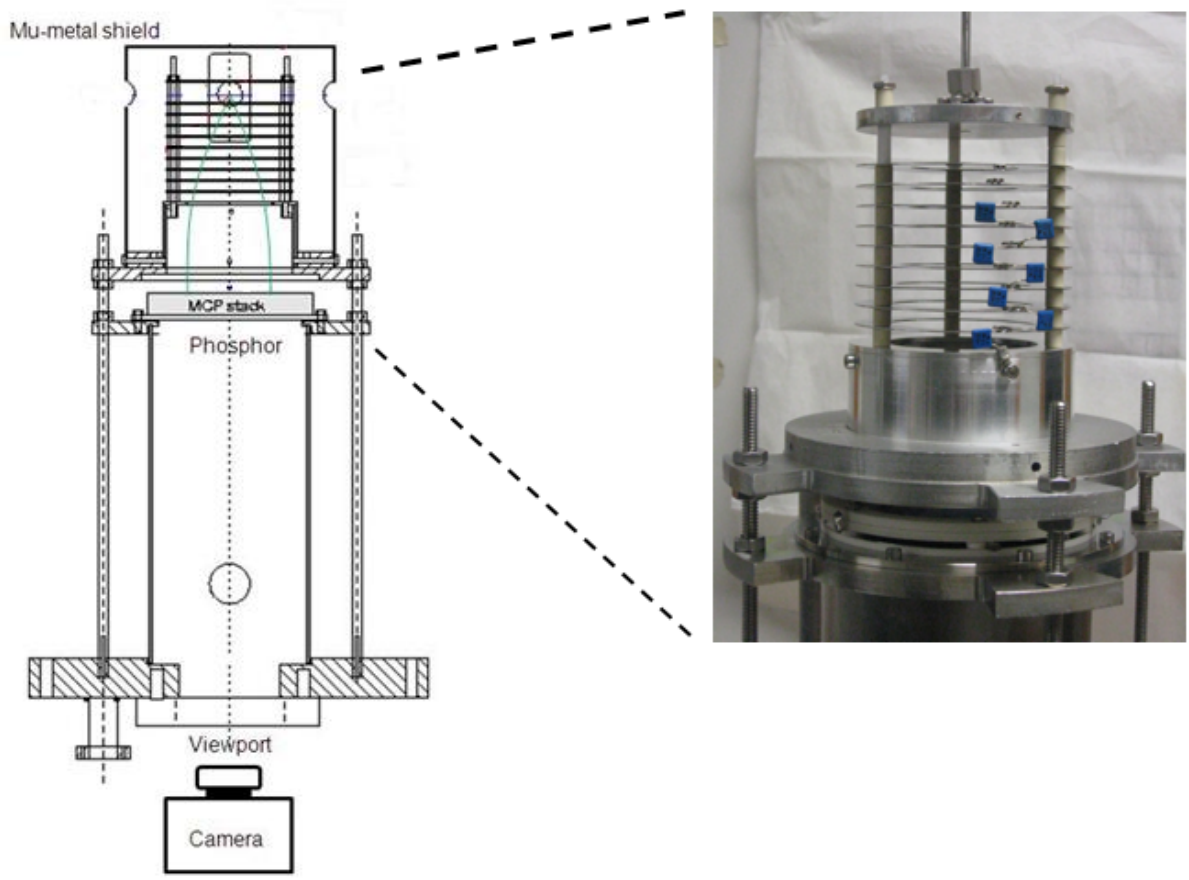

Figure 2.9: *Design of the multi-electrode VMI spectrometer (line drawing on the left) and a picture of the spectrometer assembly (on the right). The basic components shown are as follows: (i) the ion-optics, comprised of an Al repeller plate with the effusive gas jet (top thick plate in the picture), nine stainless steel plates separated by a fixed gap (the bottom seven are connected with adjacent ones with resistors) and a grounded flight tube; (ii) MCP-phosphor assembly; and (iii) a camera outside the chamber focused on the back of the phosphor through a view port. Design credit: Sankar De.*

repeller connected to the gas manifold allows the gas to form an effusive jet between the repeller and the first electrode, along the ion-optics axis. The 1" ceramic insulator with a capability of isolating up to 6 kV insulates the gas line from the HV repeller. Following the "Paschen Curve" the pressure in the gas line is maintained at 1 atm or above to avoid HV breakdown.

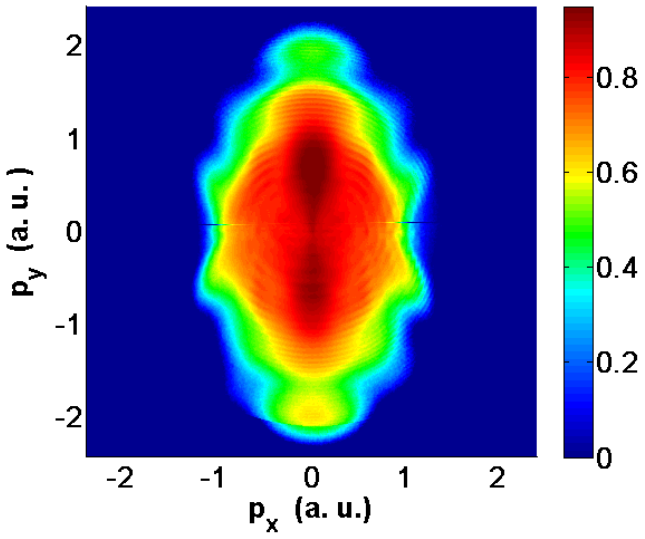

Figure 2.10: *A density plot showing a typical electron momentum image for a Xe target at a laser peak intensity of 1.0* $\times 10^{13}$ W/cm^2 *acquired with the VMI spectrometer. This is a projection of the 3D interaction distribution as captured on the phosphor screen.*

2.4.1 Data acquisition

In case of electron acquisition the repeller is maintained at maximum negative voltage (-2 to -4 kV depending on the laser intensity we are studying). The consecutive electrodes have gradually decreasing negative biasing. The field ratio of the repeller to 4th electrode is 0.8 and the electrodes in between have equal voltage steps down. From 4th to 10th electrode the field gradient is sharper but again in equal steps down to 0 v on the last electrode. The remaining flight tube from the last electrode to the detector assembly is also at ground voltage. So the electrons from a photoionization process fly towards the detector and are velocity mapped on it. The signal gets amplified across the MCPs and falls onto the phosphor screen. The MCP back is maintained at about 1.8 kV and the phosphor screen is biased at a 2 kV difference, so at 3.8 kV. The image on the phosphor screen averaged over several shots is captured by a camera placed outside the vacuum chamber and focused on the back of the phosphor screen through a glass window.

For ion extraction the spectrometer is biased accordingly with maximum positive voltage on

the repeller and the voltage gradually decreasing to 0 V on the 11th electrode. A repeller voltage of about 1 kV is usually sufficient to get the highest energy ions on the detector.

A fast high voltage switch along with a delay generator is used to time gate the MCP-phosphor voltage. The gate mostly with a 150 ns width is set at a desired delay in order to selectively collect ion fragments with a specific massto-charge ratio. In the case of electron acquisition the switch helps to keep the background counts low.

The camera used is a Sensicam QE cooled digital 12 bit CCD camera system. It is constantly cooled by thermo-electric cooling (Peltier) down to -12 ° C which keeps the noise level very low. The resolution is as high as 1376×1040 pixels. The exposure time is usually set at fractions of a second to 1 second, so that counts on the phosphor are averaged over that time at the readout rate of 10frames/second (16 MHz).

A typical 2-D projection of the momentum distribution of electrons from Xe atoms is presented in Fig 2.10. The axis convention used throughout in all experiments is as follows: The laser propagates along the positive y-axis. The polarization is along z-axis. The fragments fly to the detector assembly after ionization along the x-axis.

2.4.2 Efficiency correction

The MCP detectors in our VMI system suffered damage due to excess electrons incident on it along a central line in the polarization direction. This surface damage rendered the acquisition efficiency of the detector to be non-uniform, thus introducing error in the acquired electron momentum distribution. We correct for this effect to retrieve the actual distribution. We normalize all 'raw' images (the 2D projections acquired on the phosphor) by dividing it by a correction image. In Fig 2.11 the upper panel shows an example of images (left to right) before and after correction. The lower left panel image shows the efficiency correction matrix. The correction image is derived from a detector image taken with the polarization pointing towards the detector. Such an image is expected to create an angularly uniform distribution. Departure from that, as shown in the lower right image

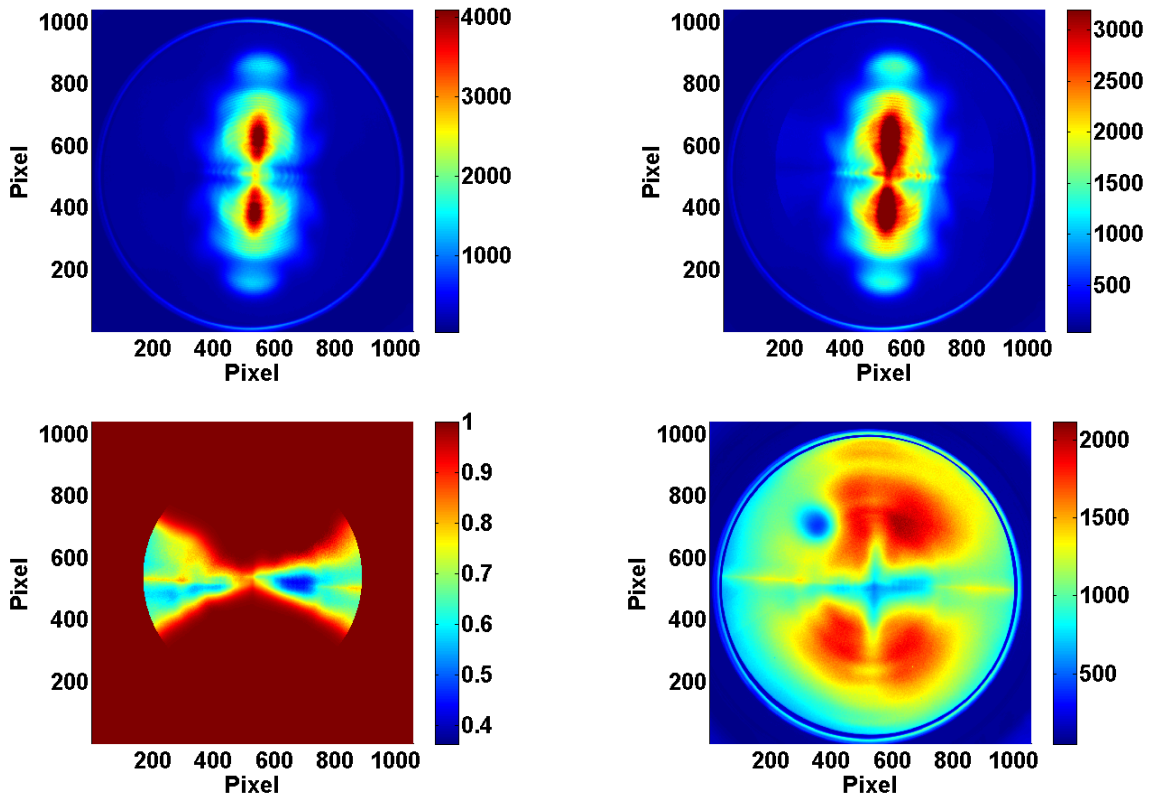

Figure 2.11: *Example showing the detector efficiency correction. Upper panel: (i) (upper left) The raw image of photoelectrons from Xe target acquired with the VMI, and (ii) (upper right) The same momentum image after the detector correction factor has been applied. Lower panel: (iii) (lower left) The correction matrix: Each element of the raw image matrix is divided by the corresponding element of this correction matrix to get the efficiency corrected image. In the correction matrix all elements corresponding to undamaged detector are 1 and fractional values along the central line (horizontal) are proportional to the amount of damage on the detector in that area. (iv)(lower right) The image of electron distribution on the detector when the laser polarization points towards the detector. For an undamaged detector the image should be independent of angular variation. Departure from that shows damage to the detector. This image is used to derive the correction factor.*

accounts for the detector damage. In the correction image undamaged detector areas are represented by the value 1. The correction is done only for the damaged region along the central line. The fractional values represent detector damage and are proportional to the amount of damage.

This correction is relevant and critical only for Ch 3 where we are dealing with photoelec-

tron momentum distributions. The data analysis in Ch 4 and Ch 5 do not require this correction step as we focus on data integrated about the polarization over a certain angle. This completely excludes the damaged regions from consideration.

2.4.3 Inversion

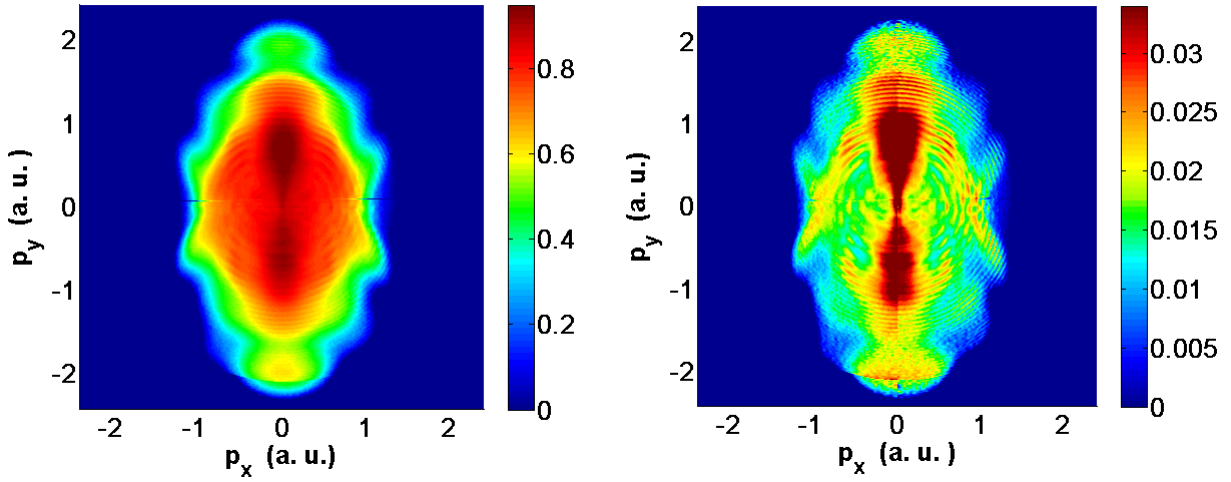

Figure 2.12: *VMI images of photelectron momentum distribution from Xe gas before(left) and after(right) image inversion by iterative method. Before inversion the image represents the 2D projection of the 3D momentum distribution. After inversion the image is equivalent to a slice through this 3D distribution along a plane containing the axis of symmetry.*

The data acquired on the phosphor screen of the VMI is a 2-D projection of the 3-D interaction distribution. The general dynamical information and some salient features can be observed directly in the 'raw' 2-D image. However to do an accurate analysis and extract all information from the data we need to reconstruct the 3-D velocity distribution from the projection. This can be done by two approaches:(i) inversion methods, or (ii) forward convolution methods. Both methods use the fact that the 3-D distribution has cylindrical symmetry about an axis parallel to the phosphor (in this case, the polarization vector). The algorithm used in our data analysis follows the second principle known as iterative method[12].

In the iterative inversion algorithm a 3-D velocity distribution, following the radial and angular distribution of the experimental 2-D image to be inverted, is generated. The 2-D projection of this 3-D distribution is then calculated and compared with the experimental 2-D image. A correction factor derived from this comparison is applied back on the 3-D distribution. Several iterations of this process is carried out till the experimental and calculated 2-D images agree well. A typical momentum image from Xe gas before and after inversion is shown in Fig 2.12.

2.4.4 Energy Calibration

The momentum images acquired with the VMI system requires an energy-calibration to convert the image axes from pixel numbers to the correct momentum or energy values. This is done using the SIMION simulation. From Fig 2.8 the transverse energy per charge versus the radius on the phosphor screen can be plotted.

For a fragment of energy E, and charge q ejected perpendicular to the detection axis, the radius R on the detector at which it will be detected can be given by the equation:

$$R = k\sqrt{E/qV} \tag{2.2}$$

where k is a calibration constant, and V repeller voltage. From the SIMION plots the value of the constant k is calculated. It is also cross-checked by comparing the known KER spectrum of D^+ ions acquired by COLTRIMS with that acquired in VMI under the same conditions.

For $q = 1$ (electron), E in eV, V in kV, and R in number of pixels, the constant is found to be, $k = 88$. This is the calibration factor used throughout this thesis.

1000 pixels of the camera corresponds to 78mm diameter of the phosphor screen, i.e., 1 mm = 12.82 pixels. If R is measured in 'mm' the constant is calculated as k = 6.3.

2.5 Intensity calibration

For all the experiments it is important to know the peak intensity of the laser pulse. The intensity is a crucial parameter that we often vary to study the response of the atomic and molecular dynamics at different peak intensities. The peak intensity can be estimated from a first-principles calculation by knowing the pulse parameters. These are the beam diameter, the total energy per pulse, the pulse duration, the wavelength and the focal length of the lens used to focus the beam on the target. Alternatively the intensity can be evaluated *in situ* from the atomic physics: by knowing the energy cut-off from an electron momentum spectrum, or by analysis of relative peak strengths in the KER spectrum from ionization of D_2 [13].

The first-principles approach is discussed in the following section. A systematic comparison of the intensity calibration using the different methods is included in Appendix A.

2.5.1 Laser Intensity

The intensity profile of the laser beam is assumed to follow a Gaussian profile as shown in Fig 2.13. Considering the origin to be at focus $y_0 = 0$, and y-axis as the propagation

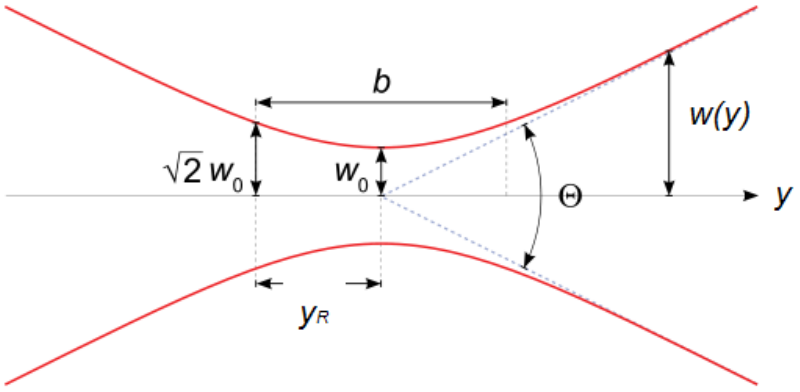

Figure 2.13: *Schematic diagram of the Gaussian beam focusing geometry.The $1/e^2$ beam radius $w(y)$ as a function of y is shown. w_0 is beam waist (beam diameter at focus), y_R is Rayleigh range and θ is the total angular spread. [Figure Source: http : //en.wikipedia.org/wiki/Gaussian_beam]*

direction the $1/e^2$ beam radius can be written as:

$$w(y) = w_0\sqrt{1 + (\frac{y}{y_R})^2} \tag{2.3}$$

The radius of curvature of the wavefront at any distance y is given as

$$R(y) = y + \frac{y_R^2}{y} \tag{2.4}$$

The Rayleigh range y_R is defined as the distance from the focus over which the beam radius increases by a factor of $\sqrt{2}$ from waist:

$$y_R = \frac{\pi w_0^2}{\lambda} \tag{2.5}$$

If a collimated beam is focussed by a mirror of focal length f the collimated beam radius related to beam waist as:

$$w = \frac{\lambda f}{\pi w_0} \tag{2.6}$$

The wavelength, focal length, collimated beam radius and total power are the known parameters in our experiments. Knowing these we can calculate the focusing geometry and intensity at the focus. The beam collimation can be controlled to vary the waist width and y_R and intensity.

The intensity of the laser pulse at any point (x, y, z) is given by the expression:

$$I(x, y, z) = \frac{2P/F}{\pi\omega(y)^2\tau} e^{(-2(x^2+z^2)/w(y)^2)} \tag{2.7}$$

where $w(y)$ is the beam diameter at that y, τ is the pulse duration (FWHM). The energy per pulse is the ratio of the average DC power P and the repetition rate F.

Chapter 3

Photoelectron Momentum Studies

3.1 Abstract

We measure the full vector momentum spectra of high energy photoelectrons from atomic targets (Xe, Ar and Ne) generated by intense laser pulses. Comparing Quantitative Rescattering Theory with our experimental investigations we confirm that accurate elastic differential scattering cross-sections can be retrieved from electrons rescattered with a maximum energy of $10U_p$ at different peak intensities. More recent studies show that information about the target structure, namely elastic differential cross-sections for the scattering of free electrons from the corresponding ionic core, can be retrieved over a range of energies, from $4U_p$ up to $10U_p$, independent of the peak intensity at which the photoelectron spectra have been measured.

3.2 Introduction

When an intense laser pulse is focused on an atomic target one or more electrons can be ionized. These electrons can get accelerated in the laser field and leave the vicinity of the parent ion creating "direct" electrons. Some of the electrons can also be driven back to the parent ion due to the presence of the oscillating electric field of the laser and interact with the core in various ways: they can (a) undergo elastic scattering (diffraction)[14–20] which accounts for the high energy ATI "plateau" electrons in the energy spectra; (b) inelastically scatter, creating excitation and/or ionization of the core[21–25] or (c) recombine with the core ion, causing high harmonic generation[26–29]. This sequence of phenomena was first proposed as a "three-step-model" by Corkum[29] and Schafer *et al.*[22] , and is illustrated in Fig 3.1. A

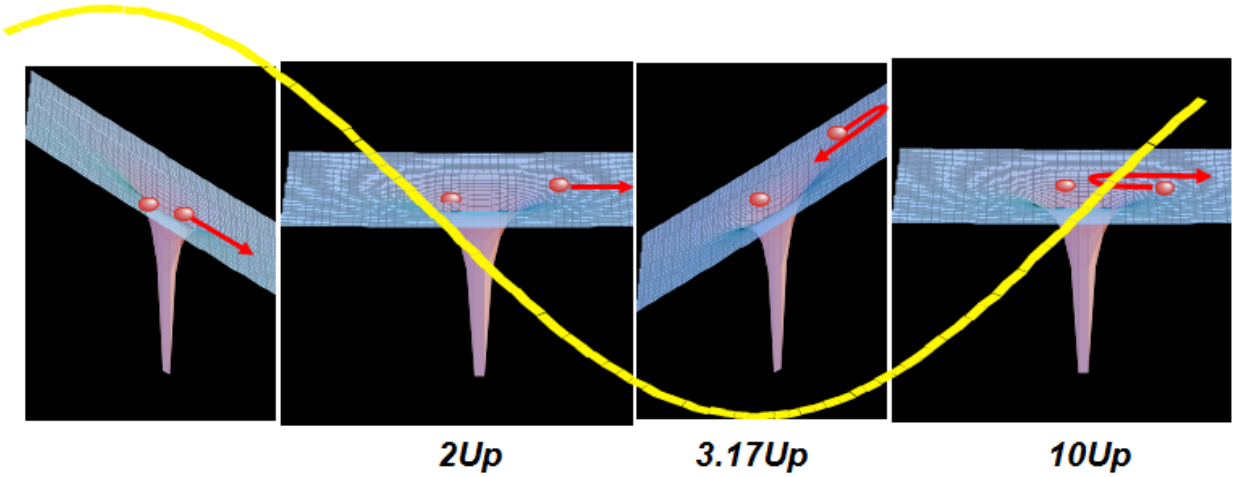

Figure 3.1: *Schematic presentation of three-step model. The electron is shown to tunnel ionize and move out of the potential well. The laser field drives the electron back to the ion core. On its return it is shown to be elastically rescattered. The maximum energy that can be gained is indicated at each step in units of U_p (where $U_p = E^2/4\omega^2$ is cycle-averaged energy of the electron in the laser electric field). Modified from: P. Corkum and F. Krausz, Nature Phys. 6, 323 (2007).*

simple semi-classical calculation predicts the energy acquired in each step of the sequence. The electron when ionized starts from rest and is subsequently acted upon by the laser field. The calculation shows that these "direct" electrons can gain up to a maximum energy of $2U_p$

depending on the birth phase of the particular electron in question (where U_p is the cycle averaged quiver energy of a free electron in an the electric field). The returning electrons can gain up to a maximum energy of $3.17U_p$. The "plateau" electrons generated by elastic rescattering of the returning electrons can gather a final energy ranging from $4U_p$ up to $10U_p$. These steps are explained in further detail in the next section. Fig 3.2 represents a typical photoelectron energy spectrum from an atom target showing the two distinct energy regions of direct and plateau electrons and a cutoff at $10U_p$. It can be noted from the spectrum that the direct electrons account for the majority of the photoelectrons generated. The rescattered electrons have a much weaker yield, several orders of magnitude smaller than the direct electrons and are therefore harder to study experimentally. The rescattered electrons have a very distinctive feature: the fairly flat yield over the entire energy range of $4U_p$ to $10U_p$ where it is dominant, which is why they are also known as "plateau" electrons. It has been of great interest for over the last few years to use these returning electrons as an

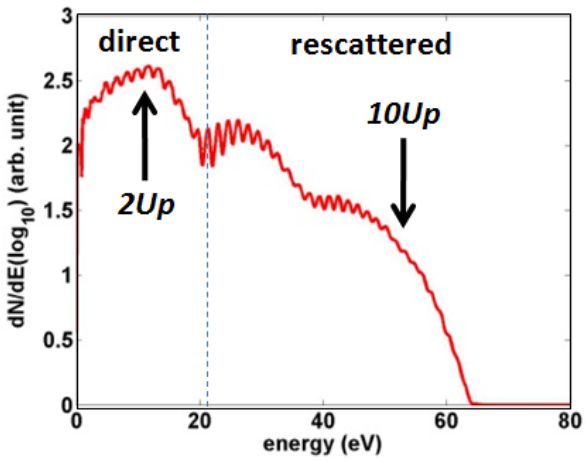

Figure 3.2: *A typical experimental photoelectron energy spectrum for single ionization of Ar by 40 fs laser pulses at peak intensity of* 1.0×10^{14} W/cm^2. *The two regions: direct and rescattered electrons are indicated.*

effective tool to do structural study of target atoms or molecules. Due to the huge flux of the returning electrons[25], much higher than available free electron sources provide, many efforts are underway to use these returning electrons to image the parent ion. Recent theoretical

investigations have revealed that by focusing on the rescattered high energy photoelectrons, accurate target structure information can be retrieved[30]. A complete solution of the time-dependent Schrödinger equation including rescattering also corroborates this statement. It further establishes that the structure along the outer ridge of the backwards hemisphere of the photoelectron momentum spectrum contains the differential scattering cross-section of free electrons from the parent atom and is thus very target dependent. In the first half of the chapter, I will discuss the experimental validation of these predicted features[31].

To some extent the diffraction effects that will be discussed here were anticipated by studies more than a decade ago. Yang *et al.*[32] first reported the result that the angular widths of the ATI spectra showed a broadening near $9U_p$ and suggested that this had to do with the characteristics of the rescattering cross section from the ionic core. Similar observations and theoretical analysis followed[19,20,33–40]. It was also known that the atomic structure of the target must play an important role in the exact nature of the backscattering from the observation that the electron spectra for different for different gases are quite different[19]; similar marked differences have been seen for K and Na[40]. The key role played by the marked differential backscattering cross section was previously suspected[32,41] but not previously examined.

3.2.1 Classical one-dimensional rescattering theory

In order to understand the kinematics involved in the rescattering phenomena, a semi-classical model tracing the classical behavior of the electrons in the laser field is explained here following the model discussed in Paulus *et al.*[20]. A simple classical model is considered where the atom is at origin and a single electron is ionized at time t_0 by the laser field. The binding potential of the atom is neglected henceforth while tracing the trajectory of the electron. Its motion in the continuum is assumed to be solely governed by the laser electric field. Depending on the phase of the laser at which the electron is ionized (ωt_0) the electron

will either revisit the ion and may scatter at some angle θ or will never return. The electric field and vector potential (Fig 3.3) are of the form:

$$\mathbf{E}(t) = E_0 \cos(\omega t)\hat{\mathbf{z}} \tag{3.1}$$

$$\mathbf{A}(t) = -\frac{E_0}{\omega} \sin(\omega t)\hat{\mathbf{z}} + \text{const} \tag{3.2}$$

The equation of motion of the electron (in a.u. units) can be described as:

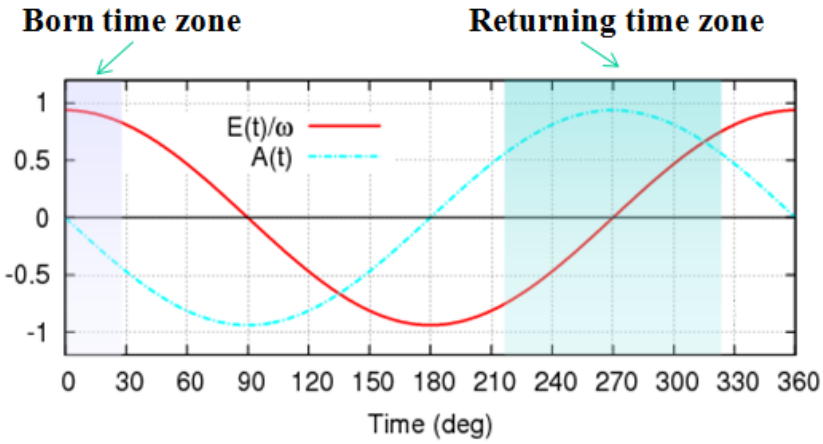

Figure 3.3: *Electric field and vector potential for a laser intensity of* $1.0 \times 10^{14} W/cm^2$ *and wavelength of 800nm. The born time and returning time zones are marked. Ref: Z. Chen et. al., PRA 79, 033409 (2009).*

$$\ddot{z}(t) = -E_0 \cos(\omega t) \tag{3.3}$$

Integrating the above equation we get the expression for velocity as:

$$\dot{z}(t) = \dot{z}(t_0) - \frac{E_0}{\omega} [\sin \omega t - \sin \omega t_0] \tag{3.4}$$

Consequently the the position of the electron would be:

$$z(t) = z(t_0) + \frac{E_0}{\omega} \sin(\omega t_0)(t - t_0) + \dot{z}(t_0)(t - t_0) + \frac{E_0}{\omega^2} [\cos(\omega t) - \cos(\omega t_0)] \tag{3.5}$$

Now if we consider the initial conditions that the electron is born at time t_0 at the origin, ie $z(t_0) = 0$, with zero velocity: $\dot{z}(t_0) = 0$ then for the time t_r when it first returns to the

origin satisfies the relation:

$$(\cos\omega t_r - \cos\omega t_0) + \omega \sin\omega t_0 (t_r - t_0) = 0 \tag{3.6}$$

Fig 3.4 plots out Eq.(3.5) for different birth phases. It is clearly evident from the plots that

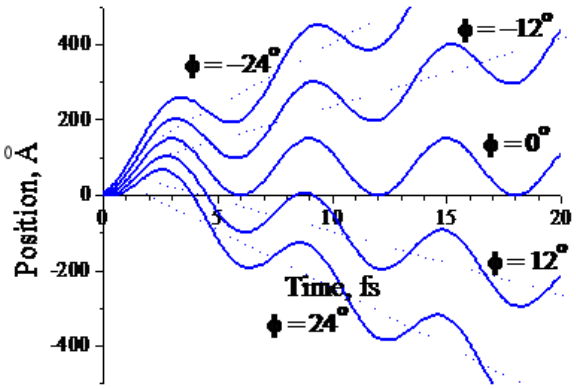

Figure 3.4: *Electron trajectories (in units of Å) in the electric field of the laser pulse for different birth phases ($\omega t_0 = \phi$). The plots indicates that for all $(\omega t_0) < 0^\circ$ the electron never returns to the core, while for positive values of the birth phase it may return once or more than once. The possibility of return is determined solely by the electric field.*

if the electron is born before the peak of the electric field it never returns to the origin. If it is born after the peak it can return more than once to the core. Since second and higher returns contribute very little to the yield we will focus only on the first return. Moreover we would want to focus on electrons which end up with the highest energy in this rescattering process based on the theoretical findings that the structural information is contained in the outermost ridge of the backscattering hemisphere, which consist of the highest energy cutoff electrons.

From Eq.(3.4) the velocity and therefore the momentum in a.u. of the electron at the time of return t_r can be written as:

$$\dot{z}(t_r) = -\frac{E_0}{\omega}\left[\sin\omega t_r - \sin\omega t_0\right] = \left[A(t_r) - A(t_0)\right] \tag{3.7}$$

Eq.(3.2) shows that the momentum can be expressed simply in terms of the vector potential. This results from the fact that the momentum gained by the electron between any two times

is the (negative of) the time integral of the laser field. Since the laser field is the negative of the time derivative of the vector potential, this integral is equal to the difference between the values of the vector potential at the two times.

Assuming elastic scattering by an angle θ on collision of the electron with the target ion, the velocity or momentum components of the electron at a time t after the return time t_r would be given by:

$$p_z = \dot{z}(t) = [A(t) - A(t_r) + \cos\theta(A(t_r) - A(t_0))] \tag{3.8}$$

$$p_y = \dot{y}(t) = [A(t_r) - A(t_0)] \tag{3.9}$$

Solving Eq.(3.5) for different t_0s reveal that electrons with birth phase within 4° and 25° are found to return between 231° and 309° and therefore receive a momentum kick greater than $0.75A_0$ due to the vector potential at the collision time (the regions are indicated in Fig 3.3). Thus these electrons can be expected to have very high final energy. Further using Eqs. (3.8) and (3.9) the photoelectron energy with which the electrons end up can be calculated. The results shows that electrons born at $\omega t_0 = 15^\circ$ gain the maximum achievable returning energy of $3.17U_p$ corresponding to a momentum of $1.22\mathrm{A}_0$. These $3.17U_p$ electrons return at a time when the vector potential is almost maximum and therefore receive a huge momentum kick to ultimately end up with the maximum final energies. In terms of their momentum vectors (since in the following sections we will be dealing with momentum spectra) the vector addition of the momentum for these high energy electrons can be expressed as:

$$\mathbf{p} = \mathbf{p}_{boost} + \mathbf{p}_{ret} \tag{3.10}$$

where $\mathbf{p}_{boost}$ is the momentum kick due to the action of the laser field after rescattering (first term in eq. 3.7) and $\mathbf{p}_{ret}$ is the momentum with which the electron is rescattered from the core (second term in eq. 3.7). The locus of these events in the momentum plane can be expected to trace out a semicircle shifted from the center of interaction by $\mathbf{p}_{boost}$ with a radius equal to the $\mathbf{p}_{ret}$ as shown in the schematic drawing in Fig 3.5. The angle θ in the figure indicates the scattering angle with respect to the incident direction as

discussed above. When θ is 180 ° ie. the electron experiences a backward scattering, it gains the maximum achievable momentum, $p_{cutoff} = 0.95A_0 + 1.22A_0$ and a maximum energy of $E_{cutoff} = 10.0U_p$. This distinct feature of the highest energy electrons backscattered at different scattering angles θ forming the semicircular rings on either side along p_z (also clearly evident in the typical electron momentum spectrum from background gas in Fig 3.5(b)) is called the Back-Rescattered Ridge (BRR).

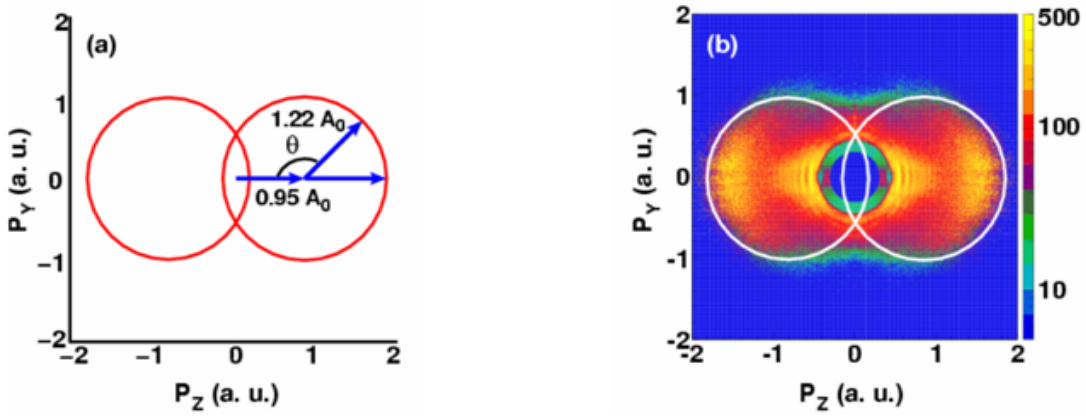

Figure 3.5: *(a) Schematic showing the relative sizes of the momentum vector of a returning electron with maximum energy and the momentum shift which this electron will receive from the laser field after recollision, at 8.3 x 10^{13} W/cm^2. (b) Experimental electron momentum image from a 7 fs pulse of this intensity on the background gas of water vapor and hydrocarbons.*

3.2.2 Quantum Mechanical approach: QRS theory

So far we have discussed in great detail a semi-classical picture describing the origin and creation of the highest energy rescattered electrons, namely the BRR. But before we proceed further we need to pose a key question: What is the huge significance of these BRR electrons - why are we at all interested? To answer this question and understand the essence of this whole discussion let us look at some Time-dependent Schrödinger equation calculations of momentum spectra for different gas targets. Fig 3.6 features photoelectron momentum plots in the plane which contains the laser polarization and is perpendicular to the laser propaga-

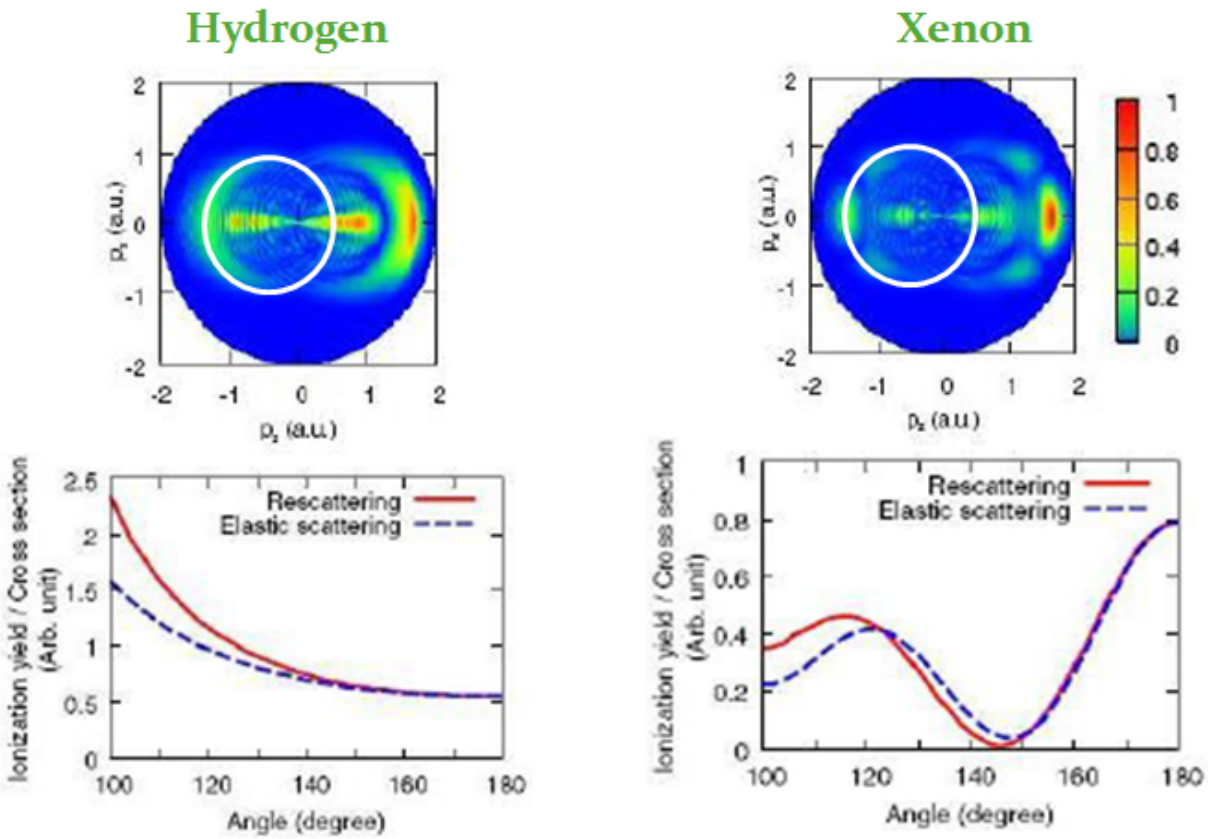

Figure 3.6: *Electron momentum spectra calculated by solving the TDSE for H and Xe atoms using a five-cycle laser pulse with peak intensity 5* $\times 10^{13} W/cm^2$ *and a central wavelength of 800 nm. The upper left plot shows H spectra and right one Xe spectra. The images are renormalized such that total yield at each photoelectron energy is unity. The white rings indicate the BRR in both spectra. In the lower panel the angular distribution along the BRRs for H and Xe (left and right plots respectively) are compared to their respective free electron differential elastic scattering cross-sections. Plots taken from: T. Morshita et. al., New J. Phys. 10, 025011 (2008).*

tion direction. These momentum images have been generated theoretically by Morishita *et al.*[42] by solving the TDSE for H and Xe atoms using a laser pulse of 5 fs and peak intensity of 5x10^{13} W/cm^2. The spectra are normalized such that the yield for each photoelectron energy sums up to unity. They both exhibit the familiar feature of shifted circles. The white rings in both H and Xe spectra trace out the BRR. But what is remarkable is, while for the simple H atom the BRR shows no structure, when we look at the BRR from a more

complicated Xe atom we see very interesting structure along the ring. The clear peaks and minima along the BRR show that some sort of interference phenomena occur in Xe and are are absent for the H atom. Further a comparison of the yields along the individual BRRs with their corresponding differential elastic scattering cross-sections for the scattering of free electrons from the respective target ions shows good agreement, as is shown in the lower panels of Fig 3.6. Thus the rescattering from the H-atom can be pictured essentially as simple Rutherford scattering from single protons[43], while that of the Xe can be visualized as more of a diffraction structure due to interference between scattering from the Coulombic potential and that from the repulsion present due to the valence electron shell. This implies that just by running a table top experiment of laser ionization of atoms and molecules we can generate an *in situ* source of returning electrons with very high current density which can rescatter from the target ions and image the same by tracing out the differential scattering cross-section in the angular distribution. Thus this calculation establishes the theoretical claim about the significance of the BRR electrons and motivates our experimental investigations.

Now let us invest little more time in discussing the quantum mechanical approach to simulating the high energy rescattered electrons. It needs to be appreciated that a full TDSE calculation as presented in Fig 3.6 is achievable for the H-atom but for more complicated many-electron atomic models this calculation becomes quite tedious and time-consuming. An alternative way can be to execute a second-order Strong-Field Approximation (SFA2) calculation which is relatively faster. The first order Strong-Field Approximation, SFA1, treats the motion of the electron quantum mechanically but in the approximation that the laser field is sufficiently strong that the atomic potential can be neglected. The SFA2 adds the interaction of the electron with the core, but only as to first order as a perturbation. Such a calculation does represent the interaction of the electron with the core, and thus does produce rescattering. However, it has been found to be inadequate to provide a good description of the rescattering, since the interaction of the electron with the core is much

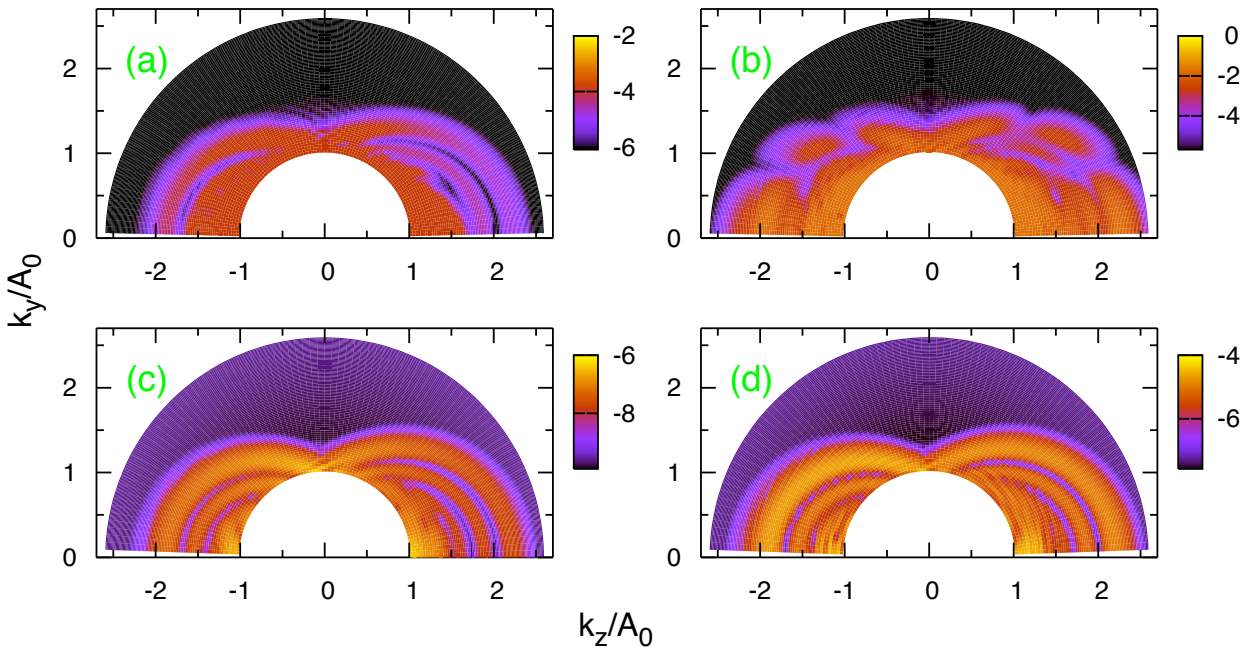

Figure 3.7: *TDSE and SFA2 results of electron momentum distributions for H and Xe atom using a 5 fs laser pulse with peak intensity of 1.0 × 10^{14} W/cm^2 at 800 nm (a) TDSE and (c) SFA2 results for H; (b) TDSE and (d) SFA2 results for Xe. Ref: Z. Chen et. al., PRA 79, 033409 (2009)*

stronger than perturbative. Fig 3.7[7] shows a comparison between TDSE and SFA2 calculations for H and Xe-atoms. Subplots (a) and (b) in the upper panel are the TDSE images for H and Xe respectively while (c) and (d) in the lower panel are for SFA2 calculations. It can be immediately seen from the images that while the SFA2 reproduces the semicircular ridge formations along increasing energy the angular structure along the BRR in Xe showing the maxima and minima are not reproduced. In fact one cannot possibly see any structure difference in the BRR structure between the SFA2 calculations of H and Xe-atoms. Thus it is clearly not possible to compare the full momentum spectra from SFA2 calculation with experimental spectra in order to get a complete understanding of the intrinsic phenomena or target structure of any system.

In search of an effective alternative to do an efficient numerical quantum mechanical calcu-

lation to generate atomic and molecular momentum and energy spectra theory, the group of Prof. C. D. Lin came up with Quantitave Rescattering Theory based on the "three-step-model" for rescattering electrons[30]. The rescattering theory has been around for nearly two decades. It was mainly based on semi-classical predictions and was not supported by a detailed numerical calculation. The QRS model puts this qualitative model into quantitative form. The essence of this model is based on the equation

$$I(k,\theta) = W(k)\sigma(k,\theta) \tag{3.11}$$

where $I(k,\theta)$ is the vector momentum spectrum, $W(k)$ is the returning electron wave packet, and $\sigma(k,\theta)$ is the elastic scattering differential cross section (DCS)[44] between the target ion and free electron.

The first step of this model calculation involves determining the wave packet. This can be done by deriving $I(p,\theta)$ using a basic Coulombic target potential for a given set of electric field parameters following the SFA2

$$f_2(\mathbf{k}) = -\int_{-\infty}^{\infty} dt \int_{t}^{\infty} dt' \int d\mathbf{p} \langle \chi_{\mathbf{k}}(t')|V|\chi_{\mathbf{p}}(t')\rangle \times \langle \chi_{\mathbf{p}}(t)|H_i(t)|\Psi_0(t)\rangle \tag{3.12}$$

According to the QRS theory, if the laser parameters are identical, the returning wave packet should be identical (ie, independent of the target). This target- independent radial wave packet $W(p_r)$ can thus be extracted from Eq.(3.11) as $I(k,\theta)/\sigma(k,\theta)$. This procedure is valid if the DCS is calculated using first order Born approximation for a spherical potential, which corresponds to the same level of approximation as is used in the SFA2.

Having found the wave packet from this procedure, it is now sufficient to determine the differential cross section without the restrictive (and generally insufficient) Born approximation. This is done by solving the time-independent Schrödinger equation

$$[\nabla^2 + k^2 - U(r)]\Psi(r) = 0, \tag{3.13}$$

where $U(r) = 2V(r)$ is the reduced potential (which describes the full interaction of the electron with the core potential) and k is the electron momentum. This equation is solved

under the boundary condition

$$\Psi^{+}(r)_{r->\infty} = \frac{1}{(2\pi)^{3/2}}\left[\exp(ikz) + f(\theta)\frac{\exp(ikr)}{r}\right] \tag{3.14}$$

where θ is the scattering angle with respect to the incident direction and z is the the axis of incident wave vector consistent with our axis convention for laser polarization direction. The factor $f(\theta)$ is the scattering amplitude. The elastic scattering cross-section (DCS) is given by

$$\sigma(k,\theta) = |f(\theta)|^2 \tag{3.15}$$

A product of the target independent radial wave packet and the DCS generates the full photoelectron momentum spectra for different atoms. The resultant spectrum has accuracy comparable to that calculated from TDSE. Using the QRS theory reduces the computational time significantly.

The atomic model potential $V(r)$ is calculated in two ways. The potential can be determined by fitting and optimizing the calculated binding energies from an analytic form to the experimental binding energies of the ground state and the first few excited states of the target atoms . The parameters of the analytic expression are optimized for the best fit to data, and are listed in Tong *et al.*[45]. Alternatively, $V(r)$ can also be determined by modifying the potential in Garvey *et al.*[46] to give accurate binding energy for the valence electrons of the target atom. The former is referred to as Tong's potential and the latter as Green's potential.

3.3 Experimental observations

We use a 7 fs pulse with central wavelength around 800nm for studying the BRR electrons. The few cycle pulse is produced by passing a 35 fs pulse through a Ne-filled fiber, followed by a set of chirped mirrors and a compensating glass [Sec 2.2.1]. A pair of Ge plates is set right after the 'fiber-chirped-mirror' setup to reflect the beam at Brewster's angle, thereby acting as a polarization filter by selectively reflecting only the s-component. We are able to control

the intensity of the laser pulses by adjusting the incident polarization angle without adding undesired positive chirp [Sec 2.2.2]. A spherical mirror with focal length of 25 cm is used to focus the pulses to intensities of 4-9$\times 10^{13}$ W/cm^2 into a the gas cell of the Stereo-ATI Phasemeter with target gas maintained at 0.2-2 m Torr. The ionized electrons emerge from 0.5 mm slits on either side of the gas cell and travel field-free towards either detector. The electrons subtend a maximum solid angle of $\pm 4.6^\circ$ at the detectors. In order to acquire the full momentum spectra in the plane perpendicular to the laser propagation direction an achromatic half-waveplate is used to rotate the laser polarization with respect to the detector axis to collect electrons emitted at any chosen angle. The waveplate is set on a motorized dial and the electron signal is recorded for equal time-buffers over a complete angle range of 180° about the polarization direction in angle steps of 2°.

The detectors are biased with about 400 volts on the front channel plate, about 2 KV on the back channel plate and 2.3 KV on the anode. A grounded mesh in front of each detector ensures that the electron flight tube is field free. A repeller mesh placed right behind the grounded mesh is biased at -6 eV to block the lowest energy electrons. Thus the electrons having energy higher than 6 eV can reach the detector and create a signal. The individual electron pulse signals are subsequently discriminated with constant fraction discriminators (CFD) and fed to a multi-hit time-to-amplitude converter. The momenta ($\mathbf{p}$) were calculated from the flight times on an event-mode basis (discussed in detail in [Sec 2.3.2]). The locus of each event in the momentum plane can be determined knowing the momentum vector and the angle at which it is emitted with respect to the polarization direction, governed by the simple equations:

$$p_z = \mathbf{p} \cdot \hat{\mathbf{z}} = |\mathbf{p}| \cos\theta' \tag{3.16}$$

$$p_y = \mathbf{p} \cdot \hat{\mathbf{y}} = |\mathbf{p}| \sin\theta' \tag{3.17}$$

where p_z is the component along the polarization and p_y is perpendicular to it, and θ' is the angle of electron emission with respect to the laser polarization.

A typical spectrum taken with the cell containing water vapor and hydrocarbons, the back-

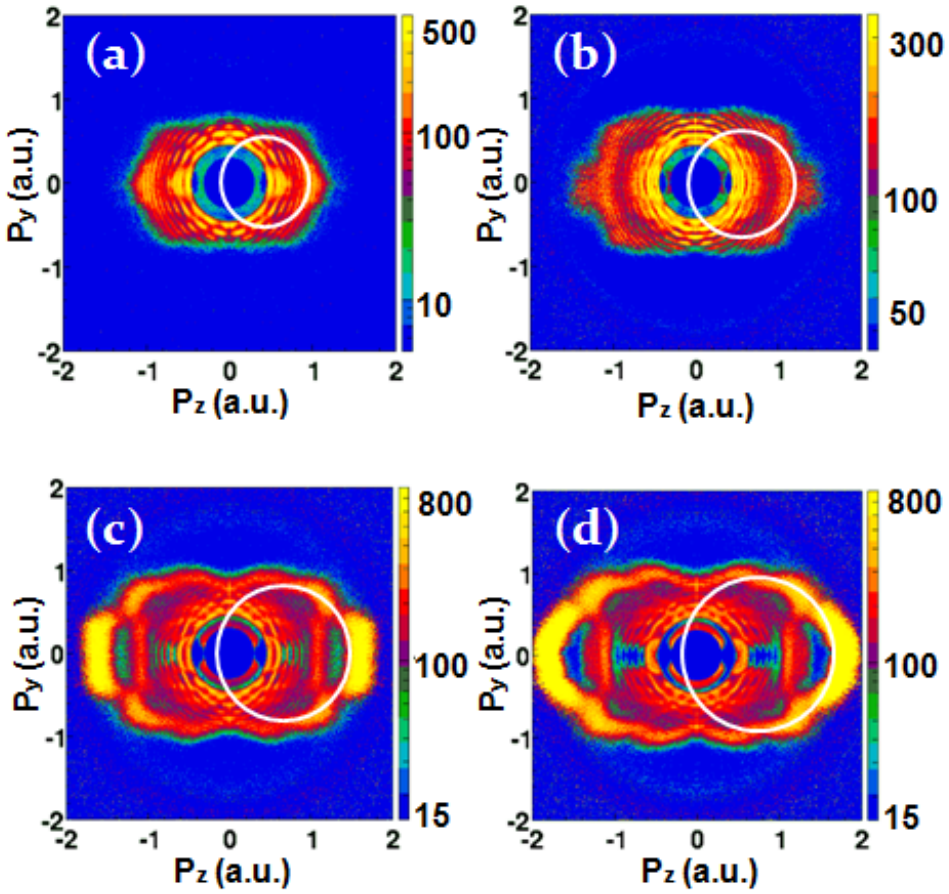

Figure 3.8: *Density plots of electron momentum spectra at different laser intensities for 7 fs pulses on Xe. The intensities (in units of 10^{13} W/cm^2) and corresponding values of p_0 (in a.u.) are, respectively, (a) 4.18, 0.74; (b) 5.8, 0.86; (c) 7.1, 0.95; and (d) 8.3, 1.03. The white circles show the inner edges of the regions from which the differential cross sections were extracted.*

ground gas in our system (evaluated using residual gas analyzer) is shown in Fig 3.5. All momentum images have been normalized to emphasize larger electron energies (E_e), similar to the normalization done in the theory, in order to compare the two. The electron momentum image from background gas (Fig 3.5) shows a clear signature of the BRR (indicated by the white ring). For each laser intensity the energy cutoff is determined from the corresponding background scan. The position p_0 of the shifted center of the semi-circular

BRR pattern for a given intensity can be calculated knowing the semi-classical relation $p_{cutoff} = 0.95A_0 + 1.22A_0$, or momentum shift $p_0 = 0.95p_{cutoff}/2.17$ where p_{cutoff} is the momentum at the corresponding energy cutoff. So the center-of-mass is shifted from the interaction center along p_z by p_0. The approximate differential cross-sections for electron

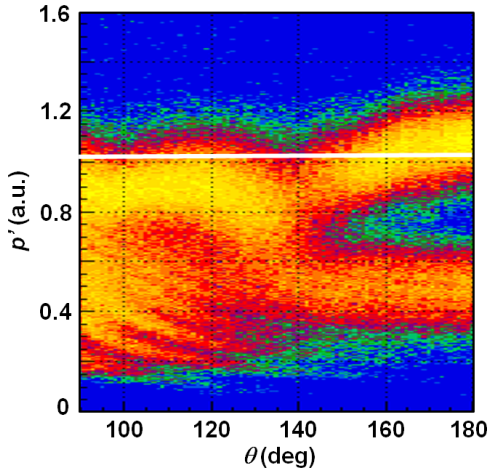

Figure 3.9: *Density plot showing p' vs. θ for laser intensity 8.3 X 10^{13} W/cm^2. The p_0 for this intensity is 1.03 a.u., and is indicated by a white line. The angular distribution is plotted by summing all the counts above this white line as a function of the scattering angle θ.*

scattering along the BRR is extracted by the following process. All electrons with $|\mathbf{p}|$ greater than p_0 are mapped onto a p' vs. θ histogram plot in an event-by-event basis (Fig 3.9). Here θ is the electron scattering angle (as indicated in Fig 3.5). p', θ relates to p_z, p_y via the equations:

$$p'^2 = (p_z - p_0)^2 + p_y^2 \tag{3.18}$$

$$\theta = (180 - 57.29 \times \arctan\left(p_y/(p_z - p_0)\right))^\circ \tag{3.19}$$

From the p'-θ plot the yield along a slice at $p' = p_r$ should in principle give the angular distribution along BRR. But in order to avoid huge error in the distribution due to low statistics we integrate the yield of all events starting from slightly below p_r (10%-15%) and extending to infinity and plot it as a function of θ. On the momentum image this is

equivalent to the total yield of events on a circular slice from radius slightly less than p_r and shifted from the center($p_z = 0,\ p_y = 0$) along p_z by p_0 (white rings in Fig 3.8) to infinity. This region approximately represents those events from the BRR corresponding to maximum laser intensity in the volume.

3.4 Results and discussions

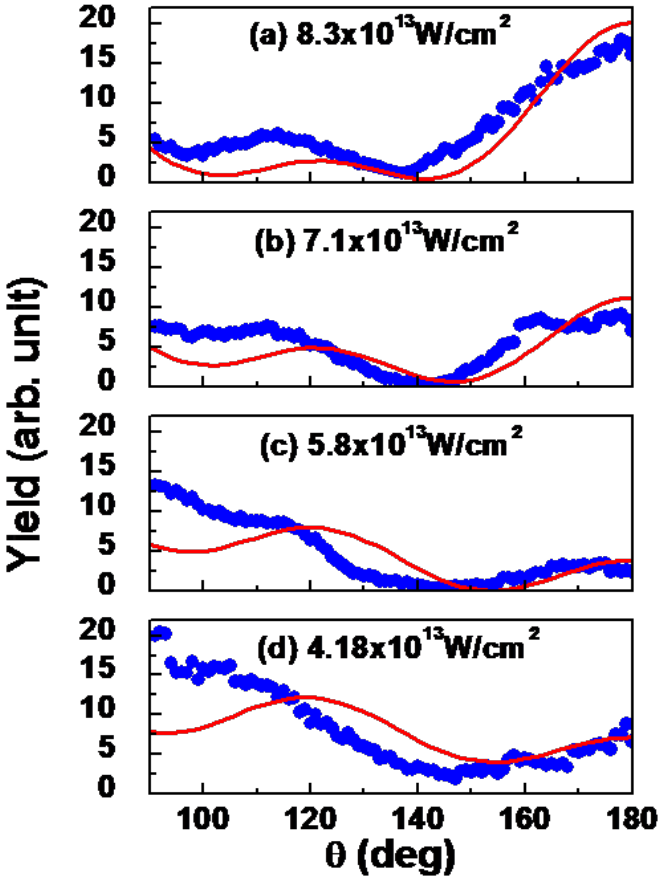

Figure 3.10: *Experimental angular distributions extracted from the data of Fig 3.8. The solid lines show the theoretical calculations of differential cross sections for free electrons scattered in the backwards direction from Xe^+. The momenta of the back scattering electrons, p_0, are, from top to bottom, 1.03, 0.95, 0.86, and 0.74 a.u. The vertical scale is the theoretical one in atomic units and the data have been normalized to match the theory.*

Fig 3.8 shows the momentum images for a Xe target at four different intensities. The momentum image from background gas (Fig 3.5) that we have discussed before has a clear BRR ridge but shows no structure in it. Contrary to that, the Xe spectra in Fig 3.8 show a clear minimum at θ of 140 ° and a weaker minimum near 100 °. These features are consistent and clearly visible at all the intensities. The whole momentum picture expands with increasing intensity, as expected, since A_0 increase. In Fig 3.8 the peak intensity I_0 and p_r vary as (a) 4.18×10^{13} W/cm^2, 0.74 a.u.; (b) 5.8×10^{13} W/cm^2, 0.86 a.u.; (c) 7.1×10^{13} W/cm^2, 0.95 a.u.; and (d) 8.3×10^{13} W/cm^2, 1.03 a.u. Although the structures along the BRR are apparent, the ridges themselves look like discs rather than the distinct isolated ridges as seen in theory (Fig 3.6). This is not surprising, since the experimental images have the effect of volume averaging across the Gaussian beam profile, and thus represents the yield over a range of intensities beginning at maximum intensity. The apparent ridge-like appearance in Fig 3.8(c) and (d) is not real. The gaps are artifacts created due to saturation of electron counts causing dead time in our electronics (effects of the CFD). The electronics also causes the high energy fast electrons to saturate and thereby artificially suppress the low energy electrons. This generates an additional enhancement of the high energy electrons compared to the direct electrons making it easier to focus on the high energy features. The central hole has been created on purpose by applying a repelling voltage of 6eV in order to block the very high yield of direct electrons. The outer ridge (lying outside the white rings) of each disk has the correct aspect ratio of $1.22A_0$ radius to $0.95A_0$ shift for the respective peak intensities, consistent with classical calculations for the BRR. The peak intensities have been cross-checked and stand consistent with an independent calculation based on focusing geometry and total measured power.

The experimental angular distributions along the BRR extracted from the Xe momentum images are shown in Fig 3.10 (blue data points). The red solid lines are the theoretical calculations for free electron scattering from Xe^+ target at a collision momentum of p_r. The experimental data has been normalized in order to roughly match the theory. The

data shows a strong minima at 140 ° and a weaker on at about 100 ° at all the intensities. However at the lower intensities Fig 3.10(c) and (d) the minima at 100 ° is predicted to be quite weak and barely shows up in the experimental data. The experimental data is less consistent with the theory at smaller scattering angles. This is because there is stronger contribution from the forward scattering of the opposite end at the lower angles which is not taken into account in the theory. This is why we plot the angular distributions only down to 90 °. The overall experimental angular distributions also might be somewhat dependent on the choice of the circular cut, ie on the estimation of A_0, but the major features remain robust independent of the choice.

In Fig 3.11 we compare the angular distributions for Xe, Kr, and Ar at the intensity

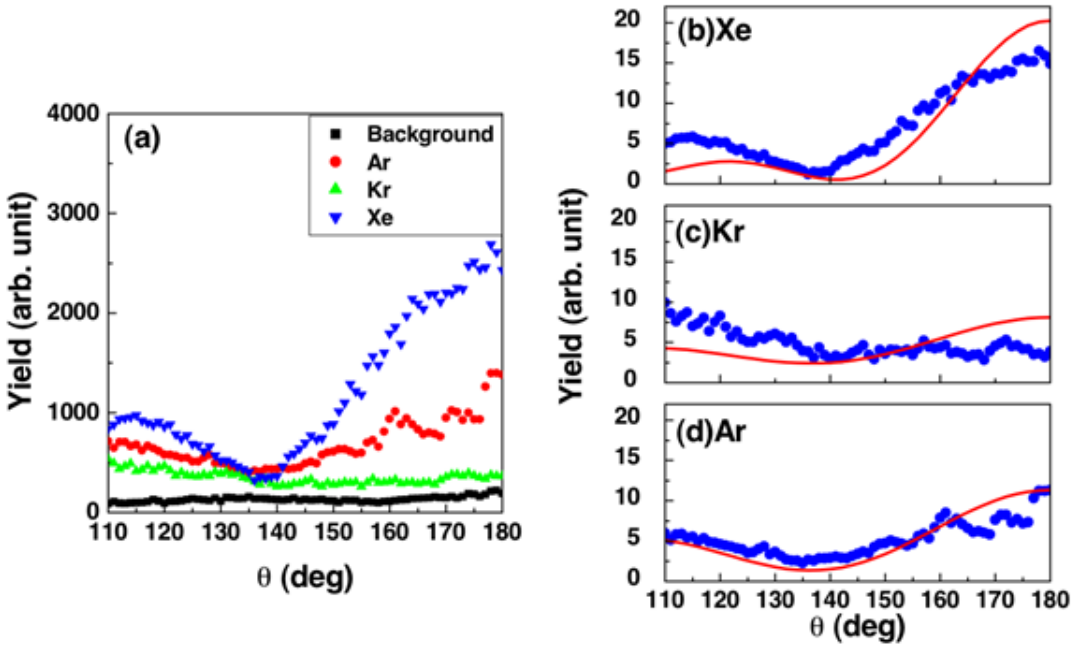

Figure 3.11: *(a) Experimental angular distributions for background, Ar, Kr, and Xe at 8.3 X 10^{13} W/cm^2. (b)-(d) Background-subtracted and normalized angular distributions, compared to theoretical differential cross sections (in a.u.) for backscattering of 14.4 eV free electrons (p_0=1.03 a.u.)*

of 8.3×10^{13} W/cm^2. Fig 3.11(a) includes the background scan at the same intensity.

Fig 3.11(b) are the background subtracted normalized angular distributions from the different target. All the distributions show good agreement with theoretical prediction, thus a clear target dependence. The Xe is seen to have a very strong backscattering peak (at 180 °) and the minima discussed before. Kr has a the weakest backscattering peak. The minima at around 140 ° is same for all targets. The weak backscattering of Kr has been observed before and can now be attributed to the atomic structure.

The distinct maxima and minima features in the angular distribution can be roughly understood as due to the presence of the electron shell. In case of hydrogen atom the scattering would just be same as Rutherford scattering from a Coulombic potential (as seen from theoretical calculation).But for the bigger atoms there is interference of the wave packets scattered from the nuclear center and that from the electron cloud thereby resulting in interference patterns that we find in the angular distributions. Along the same lines it can be predicted that since Xe, with the highest atomic number, has the maximum number valence electrons it has the strongest backscattering peak. But this is overly simplistic picture and does not hold good to explain all the features.

3.5 Generalization of QRS theory:

Up to this point we have focused our study on the electrons that return to the ion core with the highest energy of $3.17U_p$ and subsequently rescatter to form the Back-Rescattering-Ridge. More recent theoretical investigations[7,47] predict that the QRS theory is valid for not only the BRR region but over the entire energy range of $10U_p$ down to $4U_p$, ie for all rescattered electrons. In the following sections, we compare experimental data to theory in an attempt to evaluate the recent theoretical findings.

3.5.1 Experimental observations

In order to carry out a detailed analysis of the QRS theory we retook momentum images for different noble gas targets at different intensities using a more efficient data taking device: the Velocity Map Imaging Spectrometer (VMI). A 45 fs laser pulse with central wavelength at 800nm and a repetition rate of 1.5 KHz is used. The collimated laser beam enters the spectrometer chamber through a 1mm thick AR coated glass window and is focused back onto an effusive gas jet by a spherical mirror of focal length 7.5 cm. The ionized electrons are momentum focused onto a MCP-phosphor screen assembly. The images are captured by a high resolution camera focused on the back of the phosphor screen through a viewing window. This enables us to acquire the complete momentum picture at all angles without having to scan the laser polarization. An image averaged over about 30secs to 1 min gives a very robust well resolved momentum picture. So any error in angular distribution due to intensity fluctuation during scanning through the polarization angles (in the previous method) is eliminated. The artifacts due to the electronics dead time are also removed. This is extremely critical for the generalized study of all rescattered photoelectrons: previously since we were focusing only on the outermost ridge which was unaffected by the dead time issue we could afford to ignore the problem, but in order to correctly compare the lower energy rescattering electrons all such artifacts had to be removed. Thus VMI offers a more accurate and time efficient method for performing photo-electron momentum studies.

It should be noted though that the VMI method images the true dynamics since there is no artificial enhancement and preferential acquisition of the high energy electrons due to electronics saturation as was the case earlier. This makes it a little difficult to study the high energy electrons. Care has to be taken to get a good statistics of the high energy electrons yet not saturate the direct electrons. A typical Xe momentum raw image taken with VMI is shown in Fig 2.10. The raw images are projections of the interaction sphere. In order to extract a momentum slice from it in the plane of the laser polarization and perpendicular to the laser propagation the data is Abel-inverted.

The high efficiency of the VMI instrument unfortunately comes with a cost: the MCP can easily be damaged by the high flux of electrons. After some use, we observed that the MCP became damaged due to the large number of electrons hitting it along the axis parallel to the polarization vector of the laser. The result was to produce a region along this axis which had a lower efficiency than that for the remainder of the MCP. A temporary solution to this problem was to rotate the MCPs by 90 ° so that this damaged line was aligned perpendicular to the polarization direction . This ensures that the damaged region no longer lies in our main region of interest. However, finally in order to completely eliminate this problem and get the accurate full momentum images, we divided each raw image by an efficiency factor (as discussed in detail in Sec 2.4.2).

3.5.2 Results and discussions

In Fig 3.12 and Fig 3.13 we present the detailed comparison of the photoelectron momentum spectra of Xe at different intensities. The peak intensity is varied as: (a) $5.5 \times 10^{13}\ W/cm^2$ (30 mw power), (b) $6.6 \times 10^{13}\ W/cm^2$ (40 mw power), (c) $7.7 \times 10^{13}\ W/cm^2$ (50 mw power), (d) $8.8 \times 10^{13}\ W/cm^2$ (60 mw power), and (e) $10.0 \times 10^{13}\ W/cm^2$ (70 mw power). The first column of these figures shows the Xe momentum images at different intensities presented in the same way as the theory momentum plots in Fig 3.7. The laser polarization

is directed along p_z. The p_z scales from -2.5 a.u. to 2.5 a.u. while p_y values run from 0 a.u. to 2.5 a.u. Only positive p_y values are plotted, since the negative p_y half is simply a mirror image of this plot and therefore redundant. The $p_z = 0; p_y = 0$ is the interaction center. At each intensity electrons with energy less than $4U_p$ are not plotted, forming the central circular hole in the momentum image. The energy spectra along the polarization (integrated over 10° about the polarization) is shown in the third column. We can get the cutoff from these energy spectra, and calculate $4U_p$ from the cutoff for each intensity.

From the p_z -p_y matrix the center-of-mass p_r-θ distribution is obtained following the transformation equations:

$$p_y = p_r \sin\theta \tag{3.20}$$

$$p_z = p_r(1/1.22 - \cos\theta) \tag{3.21}$$

The second column of Fig 3.12 and Fig 3.13 shows the p_r-θ distributions for each intensity. This center-of-mass distribution is plotted for scattering angles 0° to 180° and p_r from 0.6 to 1.3 a.u following the transformation equations above. This accounts for electrons with positive p_z and p_y only. Since we are using a 45 fs laser pulse (not a Carrier-Envelope-Phase locked few-cycle pulse) we have symmetric electric field in the positive and negative z-directions, and so the rescattered electron distribution in -p_z direction can be expected to have the same p_r-θ distribution as $+p_z$ electrons. The central hole in the momentum image (the $4U_p$ cut discussed above) creates the curved line limit on the density plot beyond which all readings go to zero. This automatically ensures that when we extract the angular distribution cuts the value automatically goes to zero at the $4U_p$ limit beyond which a comparison with QRS theory is invalid. The Jacobian for the p_z-p_y to p_r-θ transformation is given as:

$$J = p_r(1 - \cos\theta/1.22) \tag{3.22}$$

However plots in Fig 3.12 and Fig 3.13 do not have the Jacobian incorporated. A discussion of the Jacobian will follow in the next section.

Contrary to Fig 3.9 for BRR studies where the distribution was plotted for a fixed p_r and

so a slice for only $p' = p_r$ was relevant, in the present p_r-θ distributions the shifted center-to-radius ratio of 1:1.22 is valid for all p_rs. So in other words, a cut along any p_r from the p_r-θ distributions of Fig 3.12 depicts the differential scattering cross-section of free electrons incident on the ion with momentum p_r.

The laser intensities given in Fig 3.12 and Fig 3.13 are calculated from the cutoff energies in the energy spectra (in the third column). A comparison between the momentum images in the first column illustrates how the photoelectron distribution expands as the peak intensity is increased, i.e. increasing A_0 (as seen previously). The salient features however remain consistent throughout all the intensities: the angular distribution exhibits a strong peak around 180 ° a strong minimum at about 140 ° and another weaker minimum at 100 °. These features are more easily seen in the p_r-θ plots in the second column. We had observed the same major features in the BRRs (Sec 3.4) but here we see that they not only exist at the outer ridge but persist over the range from 1.2 a. u. down to 0.8 a.u. irrespective of the peak intensity of the spectrum. The spectra also show marked and systematic structure in p_r. Along 180 ° we observe a clear dip for p_r near .85 a.u. which persists for all peak intensities. This node is also seen very clearly in the energy spectra, where it appears at the corresponding energy of 33 eV. An additional dip is observed at around 20 eV. These features will be discussed in further detail later in this section.

Fig 3.14 and Fig 3.15 show the angular distribution along different p_rs extracted from Xe momentum images taken with different laser intensities. Similar to Fig 3.10 the experimental distributions are compared with theoretical calculations for free electron differential scattering cross-section (DCS) from a Xe^+ target at a collision momentum p_r. The theoretical calculations are plotted as black solid lines, while the experimental curves are presented in color coded solid lines for different intensities. The distributions are plotted over the angular range of 90 ° to 175 °. The experimental yield over the range 175 °-180 ° is not dependable due to errors accumulated along the central line in the momentum image during

the inversion and symmetrization processes, and therefore has not been plotted. All the experimental angular distributions have been normalized to scale with the theoretical curves. The experimental yields extracted for a fixed p_r from different intensity momentum images are in very good agreement with each other.

The theoretical DCS plots in the left panel of Fig 3.14 and Fig 3.15 uses Green's potential, and in the right panel they are derived using Tong's potential. A comparison between the left and the right panels indicates that the locations of the nodes are predicted well by DCS from Green's potential. However the experiment shows more pronounced minimum at 100° for the high p_r values than the theory predicts. For the DCS from Tong's potential the relative peak heights agree better with experiment, but the nodes are slightly shifted compared to the experimental nodes. These observations suggest that the correct potential is somewhere between Green's and Tong's potentials.

A few more comments about Fig 3.14 and Fig 3.15 are worth mentioning. It needs to be kept in mind that in the low intensity momentum images there are no counts at high p_r values so we can extract angular distributions only for low p_rs. Also for the low p_rs (0.8, 0.9 a.u.) the distributions from very high intensity spectra do not agree well with those from the lower intensity spectra. A close scrutiny reveals a definite trend: the angular distributions extracted from the lower intensity images are in better agreement with the theory. For instance, in the plot for p_r=1.0 a.u., the angular distribution at the intensity of 6.5 $\times 10^{13}$ W/cm^2 (red curve, total power 40 mw) has clearer nodes and agrees with theory best, while the one from 1.0 $\times 10^{14}$ W/cm^2 (magenta curve, 70 mw power) has very only very weak nodal structure. This is possibly because of the fact that for higher intensities the same p_r is closer to the $4U_p$ limit, so there can be a greater pollution of the yield from direct electrons which wash out the diffraction features of the rescattered electrons.

Fig 3.16 and Fig 3.17 shows a comparison between experimental angular distributions

with and without the Jacobian transformation incorporated. The left panel shows the angular distributions extracted from the p_r-θ density plots without the Jacobian transformation, while the right panel shows plots where the same has been applied. The transformation incurs very minor changes to the overall distribution. The multiplication by p_r causes a normalizing of the distribution enhancing the higher p_r yield relative to the lower p_rs. This only amounts to a different normalization factor for the high p_rs. The $\cos\theta$ factor changes the relative peak amplitudes only slightly, suppressing the smaller angle yield relative to yield along 180 °. It should be pointed out that the the use of the Jacobian results from the assumption that ratio of the center-of-mass momentum p_r to vector potential $A(t)$ is exactly constant (1.22) for all p_rs. But this assumption is an approximation and, especially since the Jacobian involves derivatives of the laboratory coordinates with respect to the center-of-mass coordinates, it is very doubtful that the use of the Jacobian is either justified or necessary. Since we see that the Jacobian does not change the distributions significantly we can safely leave out this transformation from future discussions and analysis.

Now we can proceed to study other atoms under the same conditions. A similar analysis has been carried out for an Ar target. Fig 3.18 and Fig 3.19 shows the Ar photoelectron momentum images, p_r-θ and energy spectra same as Fig 3.12. The intensity here is varied from (a)6.6 $\times$ 10^{13} W/cm^2 (40 mw power), in similar increment steps as before to (f) 13.0 $\times$ 10^{13} W/cm^2 (90 mw power). From the momentum images and p_r-θ plots of Ar it can be instantly noted that the rich diffraction features seen in Xe are absent.

In Fig 3.20 and Fig 3.21 we compare the experimental angular distributions for Xe and Ar for p_r 0.8 a.u. to 1.2 a.u. The left panel shows the Xe plots and the right panel shows the Ar plots. The strong high frequency fluctuation of the experimental data about the mean specially visible in Ar is because of ATI structures. The peak at 180 ° for Ar is weaker compared to Xe. The first minimum in Ar appears around 130 °. The Ar angular distributions agree very well with the theoretical DCS (plotted in black) for all p_rs. The angular distributions for Ar are quite different from those for Xe, showing a strong target dependence.

The energy dependence of the measured momentum spectra show marked features which are partially caused by the energy dependence of the wave packet and partially by the energy dependence of the DCS. The returning wave packet, which is target independent, is found to have marked dips. These minima are caused by interference between electrons traveling via short and long trajectories and ending up with same energies. At certain return phases these electrons interfere destructively thus creating the dips. These dips are seen to occur at around 20 eV and 36 eV, evident in the energy spectra of Fig 3.12, Fig 3.13, Fig 3.18, and Fig 3.19. However in case of Xe the observed dips are not solely due to the wave packet features. A comparison of the theoretical DCS calculated for Xe and Ar (left), with 3D representation of the experimental p_r-θ distribution (right) is shown in Fig 3.22. The theoretical DCS distribution only contains the atomic structure information, while the experimental data contains both the wave packet and the atomic structure information. The Xe DCS exhibits strong maxima and minima features. These features are seen to dominate the experimental Xe distribution. The Ar DCS, on the other hand, does not show any marked dips. So the minima seen around 0.8 a.u. in Ar can be attributed to the dip in the wave packet.

3.6 Summary

In this chapter we have presented experimental evidence establishing the validity of the QRS theory for: (i) the BRR electrons, and (ii)for all high energy rescattered photoelectrons from laser-matter interaction. We have observed strong angular structure in the rescattered photoelectron momentum distributions. These structure exhibit a target structure dependence. The angular distributions were interpreted as due to the characteristics of the differential cross sections for elastic scattering of free electrons from the corresponding ion core.
The angular distributions for the same target but extracted from photoelectron momentum distributions for different laser peak intensities were found to agree very well and also

compare well with theoretical DCS for the same p_r This observation established that the angular distribution for a fixed center-of-mass momentum is independent of the laser pulse parameters.

Both Xe and Ar angular distributions were found to be extremely consistent, independent of the laser parameters. The Xe distributions were compared to DCS calculated from two different potentials, and was found to agree partially with both. It is therefore possible now to derive a new, more accurate, analytic form of the potential by fitting to the experimental data.

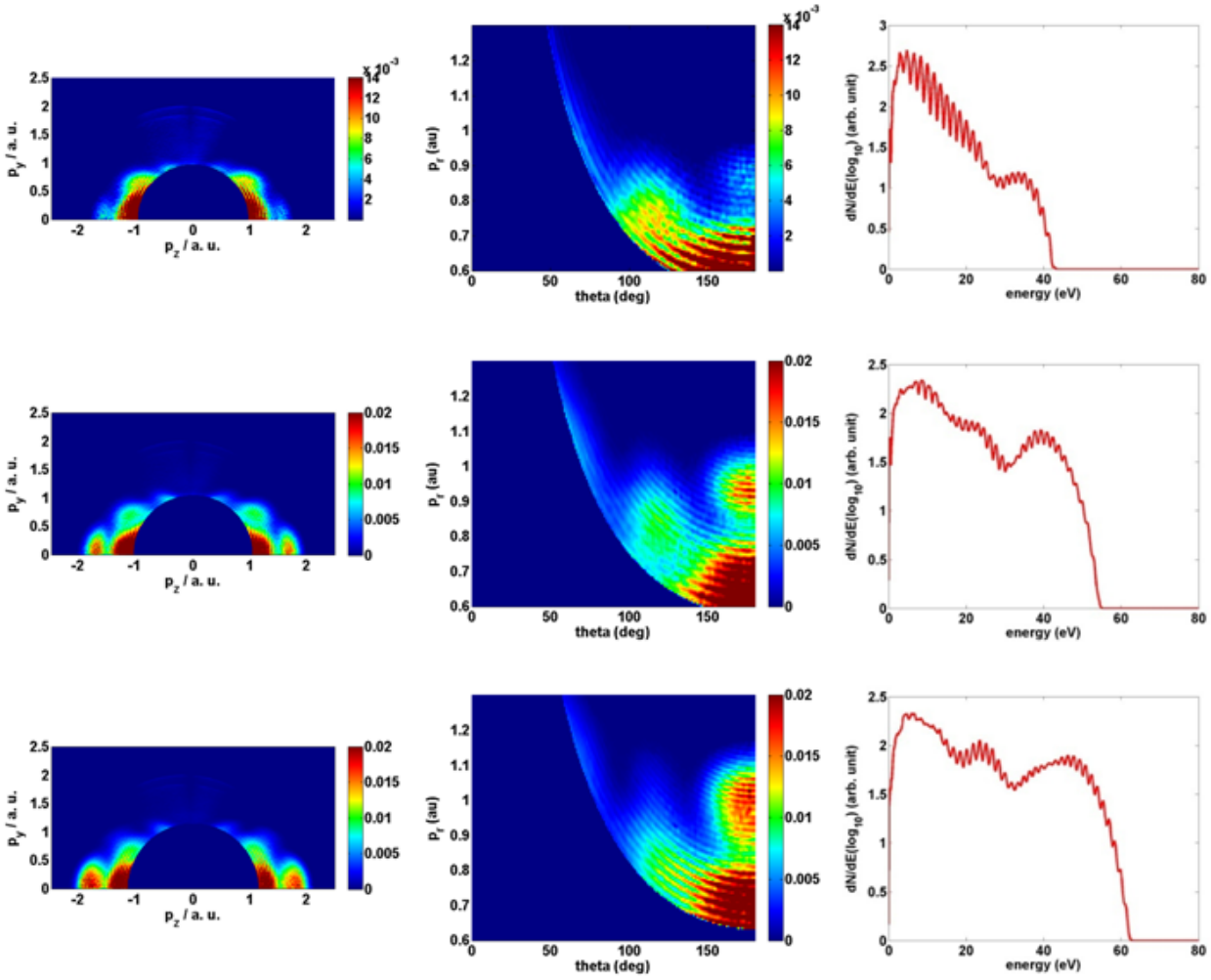

Figure 3.12: *A compilation of photoelectron momentum images for a Xe target at different intensities. The first column shows the density plots of the p_z-p_y momentum distribution. The second column consists of the center-of-mass distribution, p_r-θ plots. The third column presents the photoelectron energy spectra integrated over 10° around the laser polarization direction. The intensities (in units of 10^{13} W/cm^2) and corresponding values of experimental power measured (in mW) are, respectively, (a) 5.5, 30; (b) 6.6, 40;and (c) 7.7, 50. (continued in Fig 3.13*

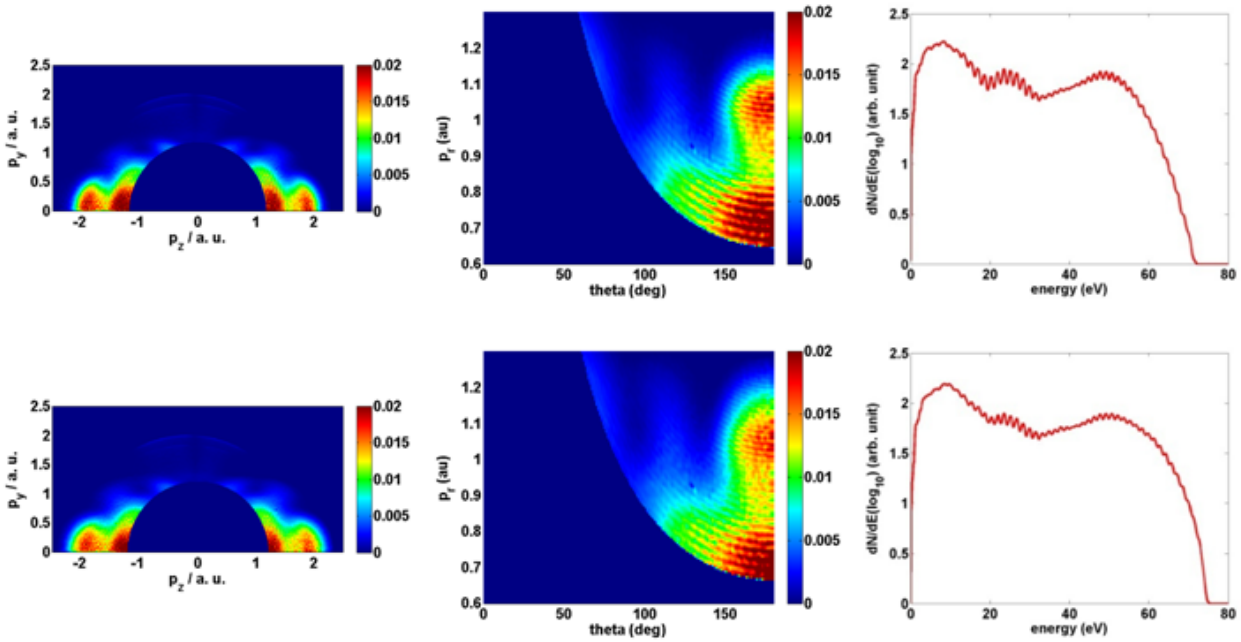

Figure 3.13: *(same as Fig 3.12) The intensities (in units of* ^{13} *W/cm^2) and corresponding values of experimental power measured (in mW) are, respectively, (d) 8.8, 60; and (e) 10.0, 70.*

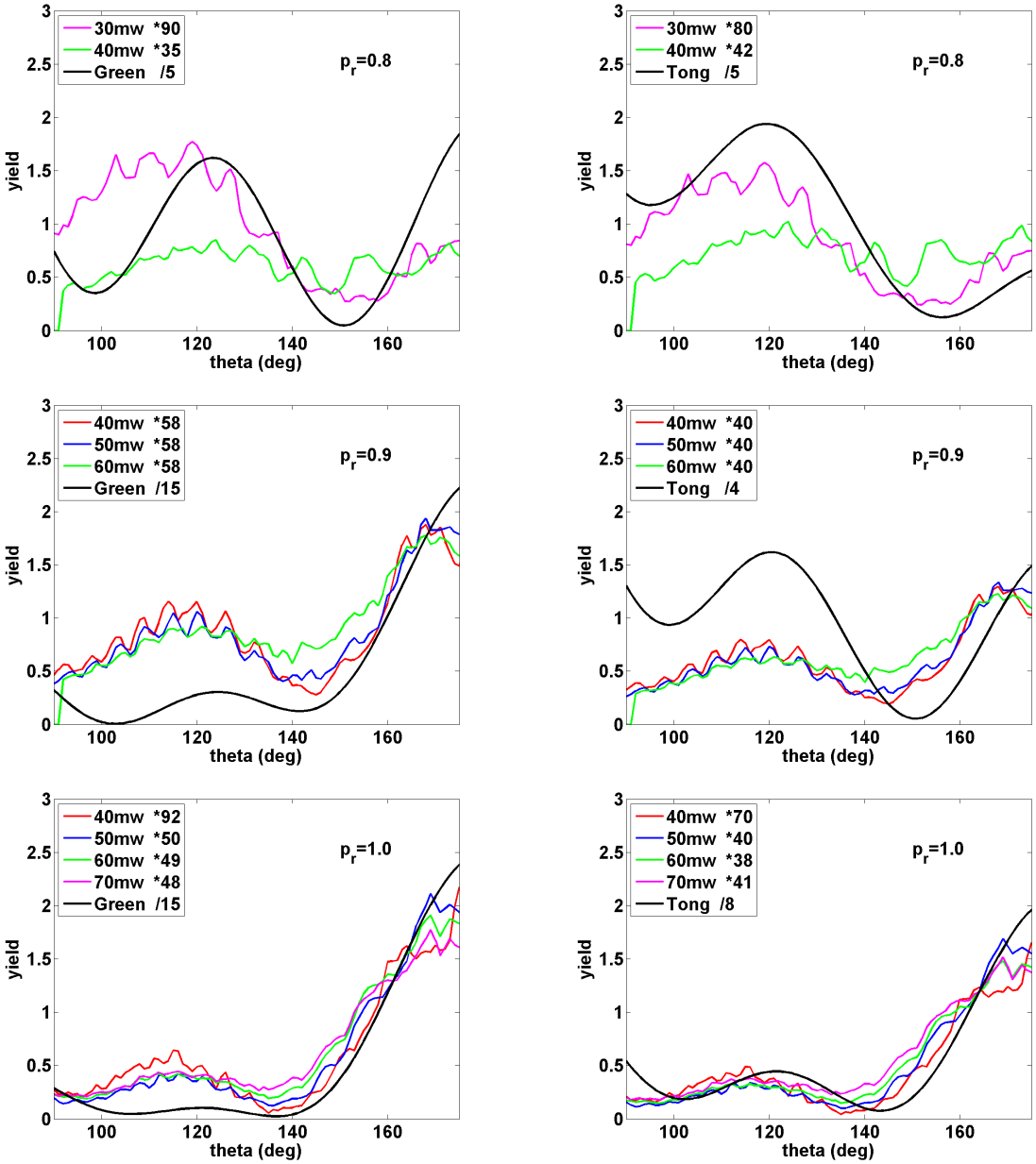

Figure 3.14: *Experimental angular distributions extracted from the data of Fig 3.12. The solid black lines show the theoretical calculations of differential elastic scattering cross sections for free electrons from Xe^+ and color coded solid lines represent experimental data at different intensities. Each column compares the experimental data with, (left): theoretical DCS from Green's potential; and (right): theoretical DCS from Tong's potential. The momenta of the back scattering electrons, p_r, are, from top to bottom, 0.8, 0.9, and 1.0 a.u. The vertical scale is the theoretical one in atomic units and the data have been normalized to match the theory. (continued in Fig 3.15)*

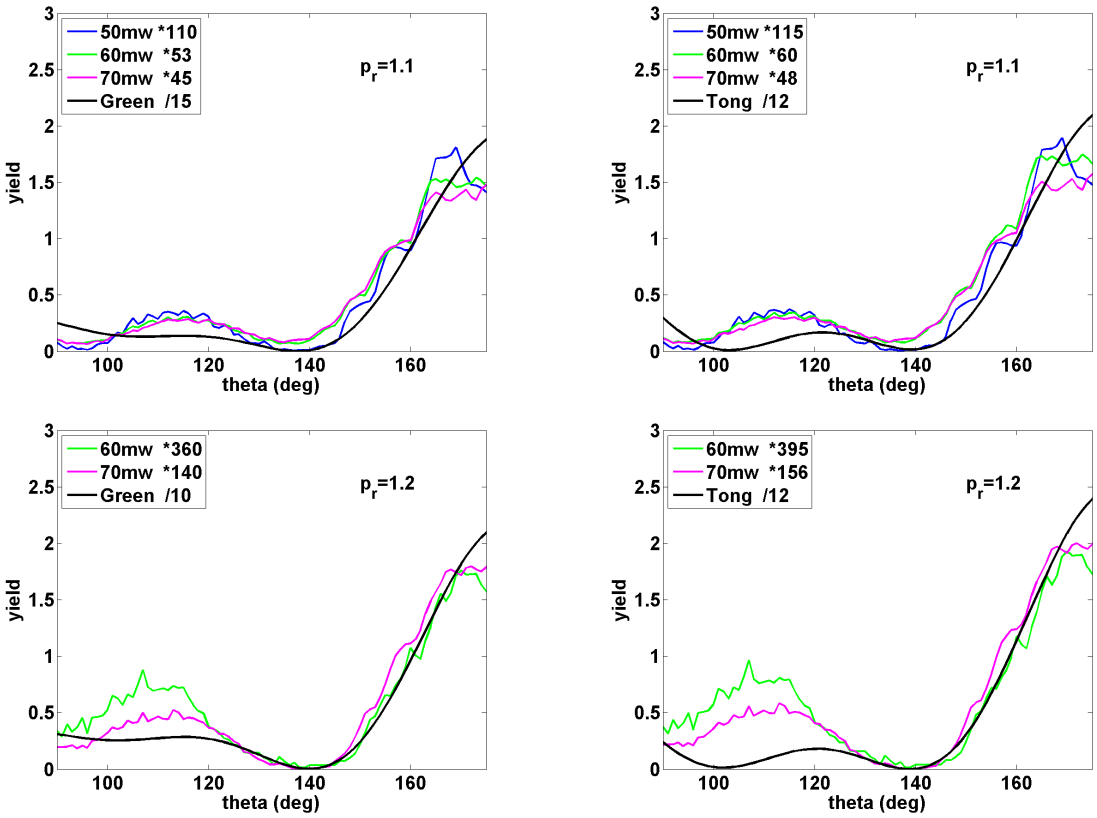

Figure 3.15: *(Continued from Fig 3.14) The momenta of the back scattering electrons, p_r, are, from top to bottom, 1.1, and 1.2 a.u.*

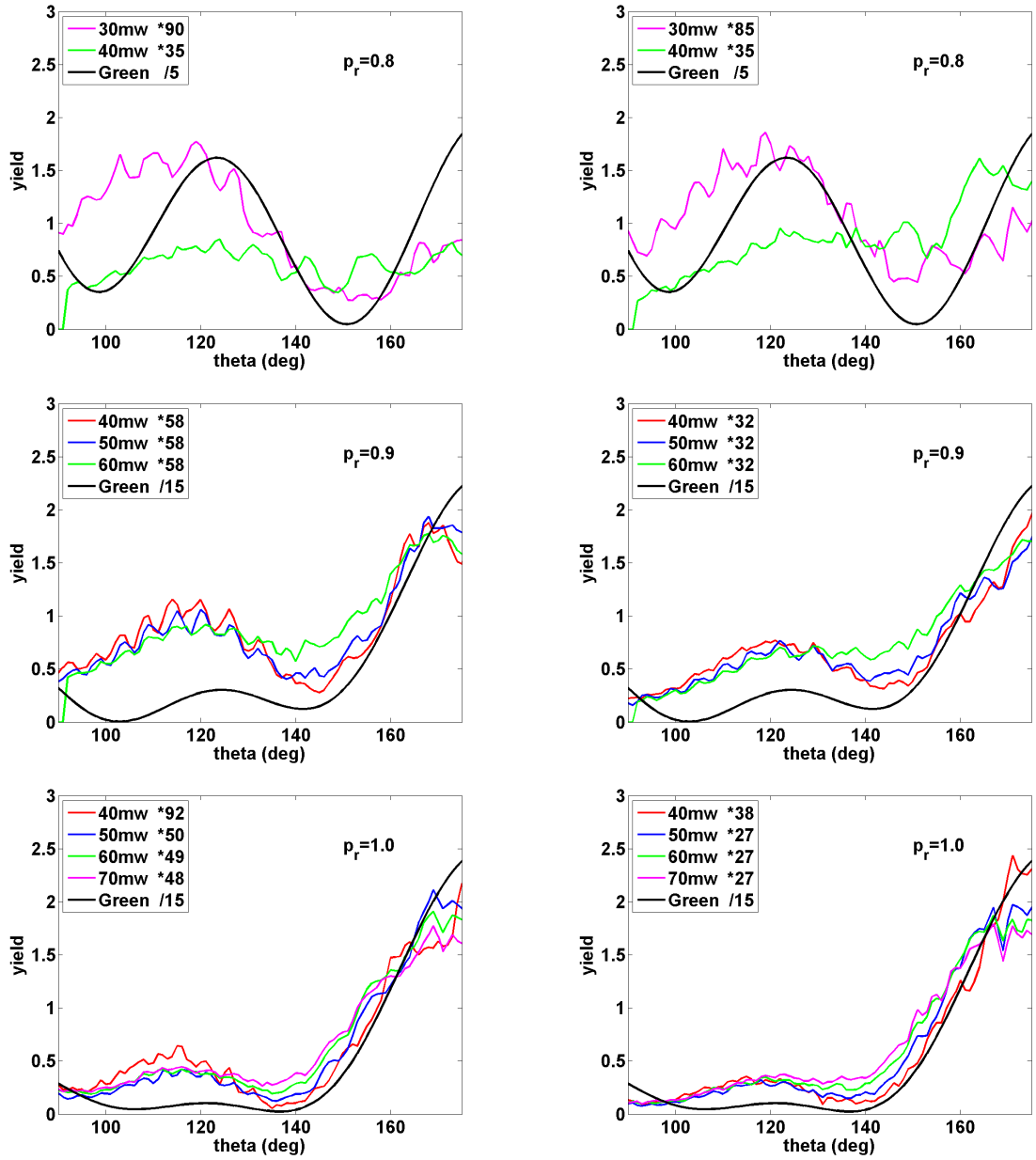

Figure 3.16: *Similar to Fig 3.14 shows angular distributions extracted from the data of Fig 3.12 and Fig 3.12 and Fig 3.13. The solid black lines show the theoretical DCS and color coded solid lines represent experimental data at different intensities. The left panel shows comparison of theoretical DCS from Green's potential with experimental data without Jacobian transformation, and right panel shows comparison with the same data but Jacobian transformed. The momenta of the back scattering electrons, p_r, are, from top to bottom, 0.8, 0.9, and 1.0 a.u. (continued in Fig 3.17)*

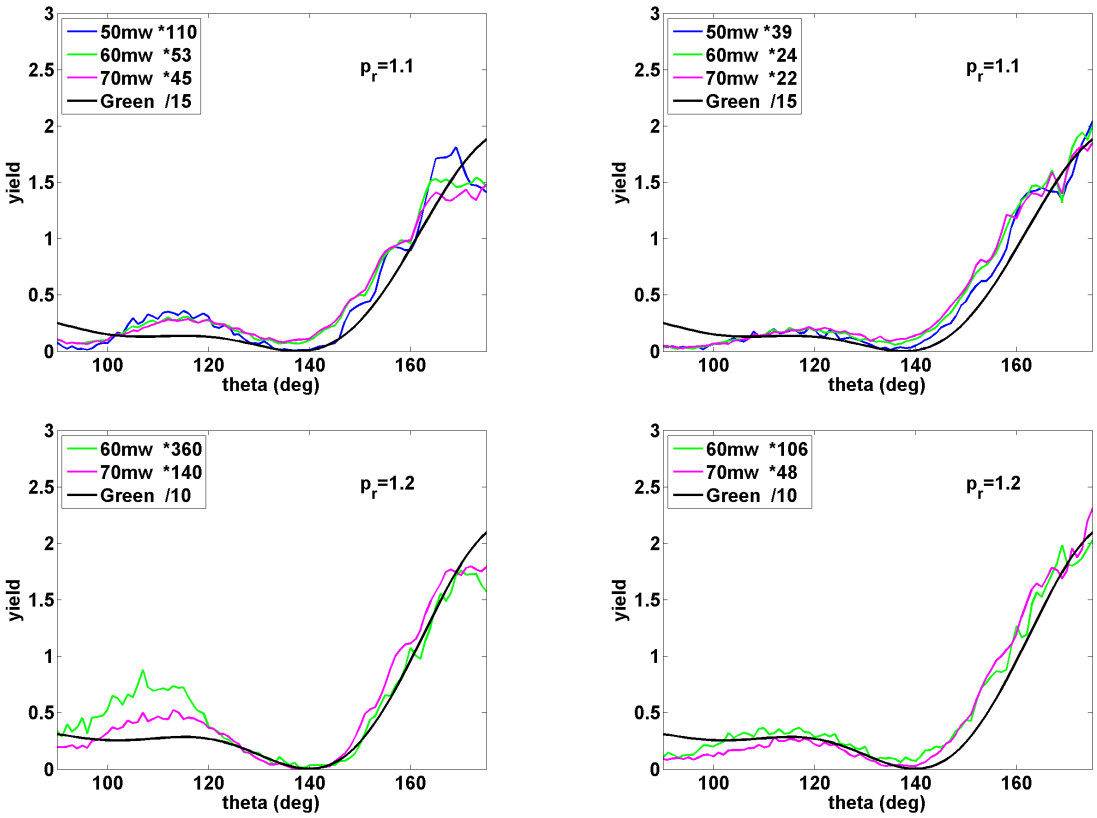

Figure 3.17: *(continued from Fig 3.16) The momenta of the back scattering electrons, p_r, are, from top to bottom, 1.1, and 1.2 a.u.*

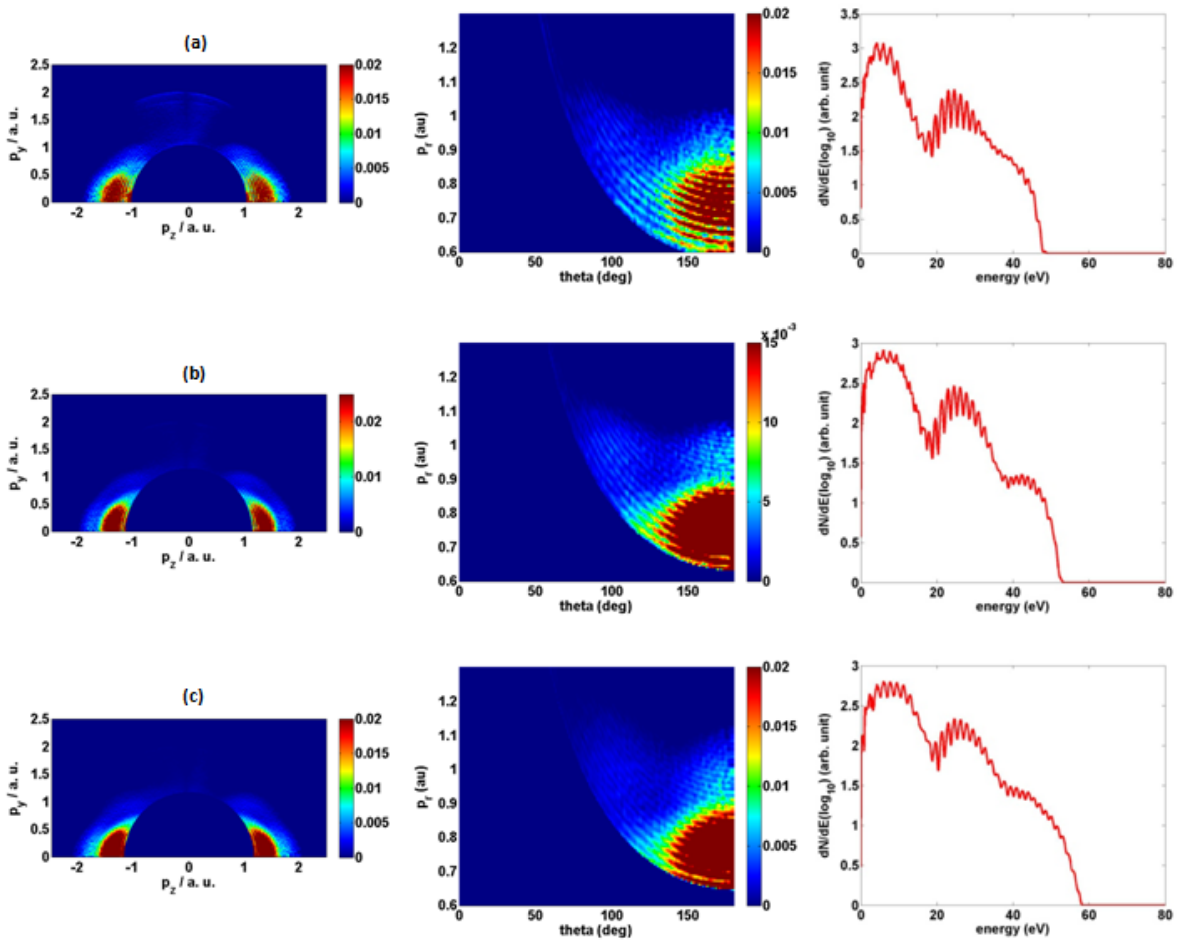

Figure 3.18: *Similar to Fig 3.12 a compilation of photoelectron momentum images for Ar target at different intensities. First column: p_z-p_y momentum distributions, second column: p_r-θ plots, and third column presents: photoelectron energy spectra. The intensities (in units of ^{13} W/cm^2) and corresponding values of experimental power measured (in mW) are, respectively, (a) 6.6, 40; (b) 7.7, 50; and (c) 8.8, 60.*

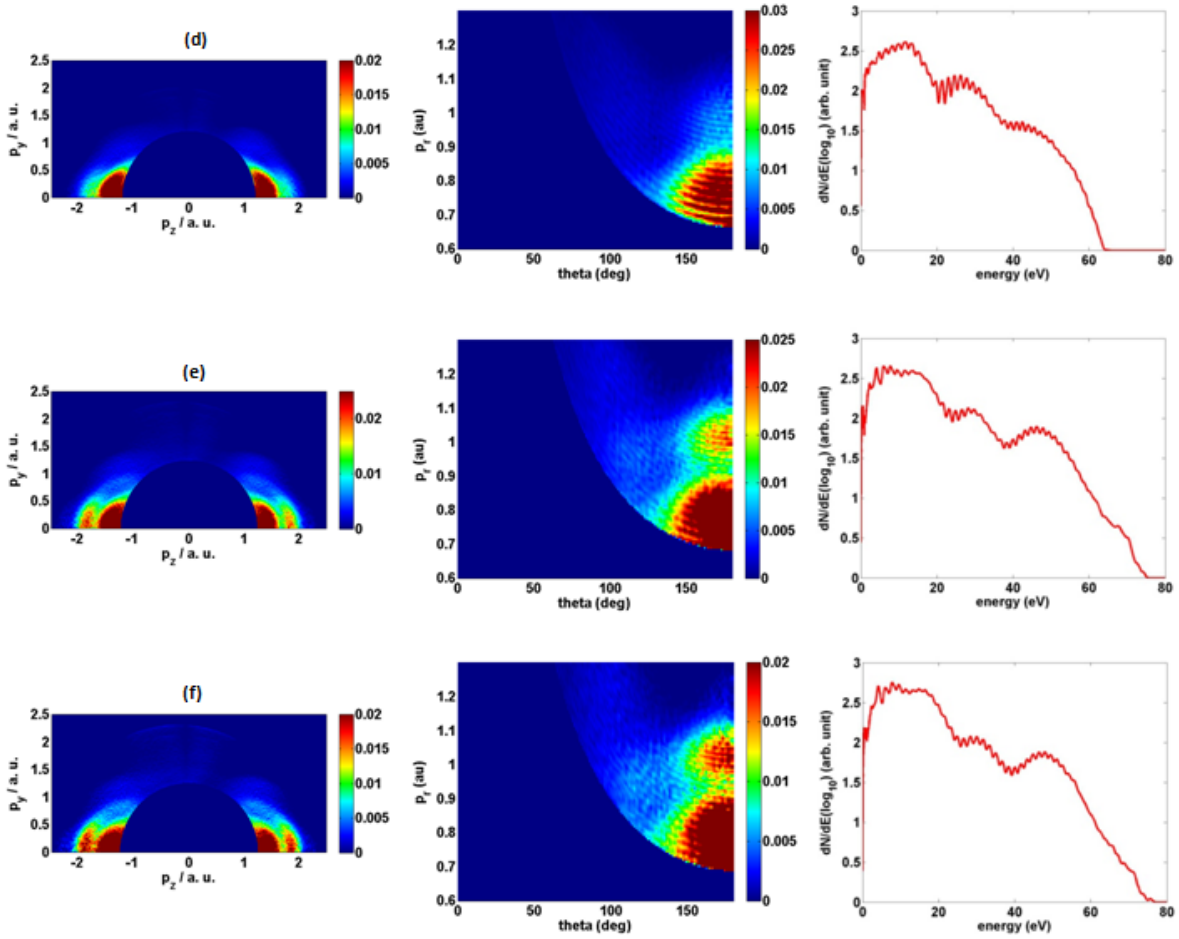

Figure 3.19: *(continued from Fig 3.18) The intensities (in units of* ^{13} *W/cm^2) and corresponding values of experimental power measured (in mW) are, respectively, (d) 10.0, 70; (e) 11.4, 80; and (f) 12.8, 90.*

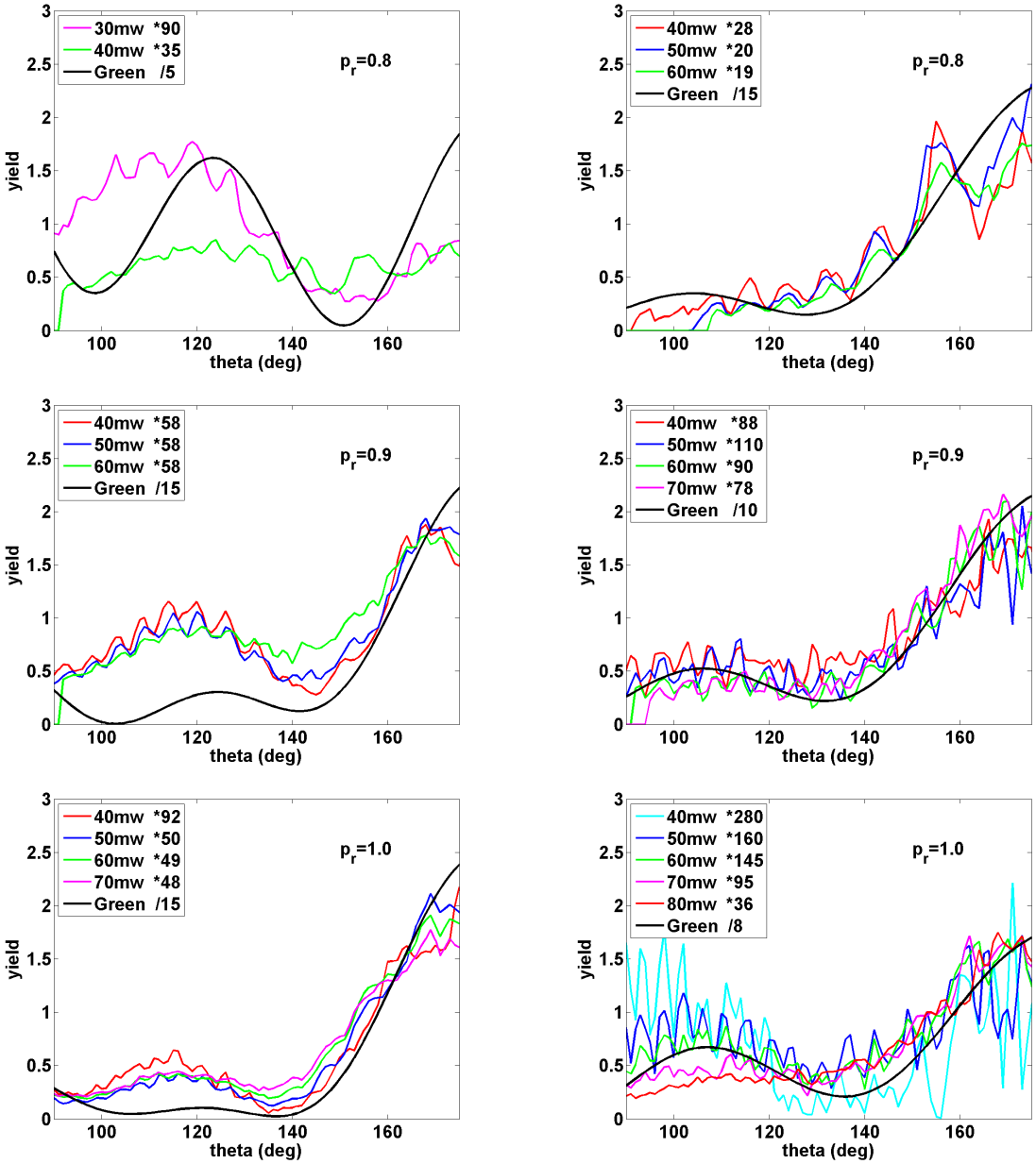

Figure 3.20: *Experimental angular distributions extracted from the data of Fig 3.12 and Fig 3.13 with that of Fig 3.18 and Fig 3.19. The solid black lines show the theoretical calculations of differential elastic scattering cross sections for free electrons from Xe^+. Each column shows comparison of DCS from Green's potential with experimental angular distribution for the same target atom, (left): Xe, and (right): Ar. The momenta of the back scattering electrons, p_r, are, from top to bottom, 0.8, 0.9, and 1.0 a.u.The vertical scale is the theoretical one in atomic units and the data have been normalized to match the theory (continued in Fig 3.21).*

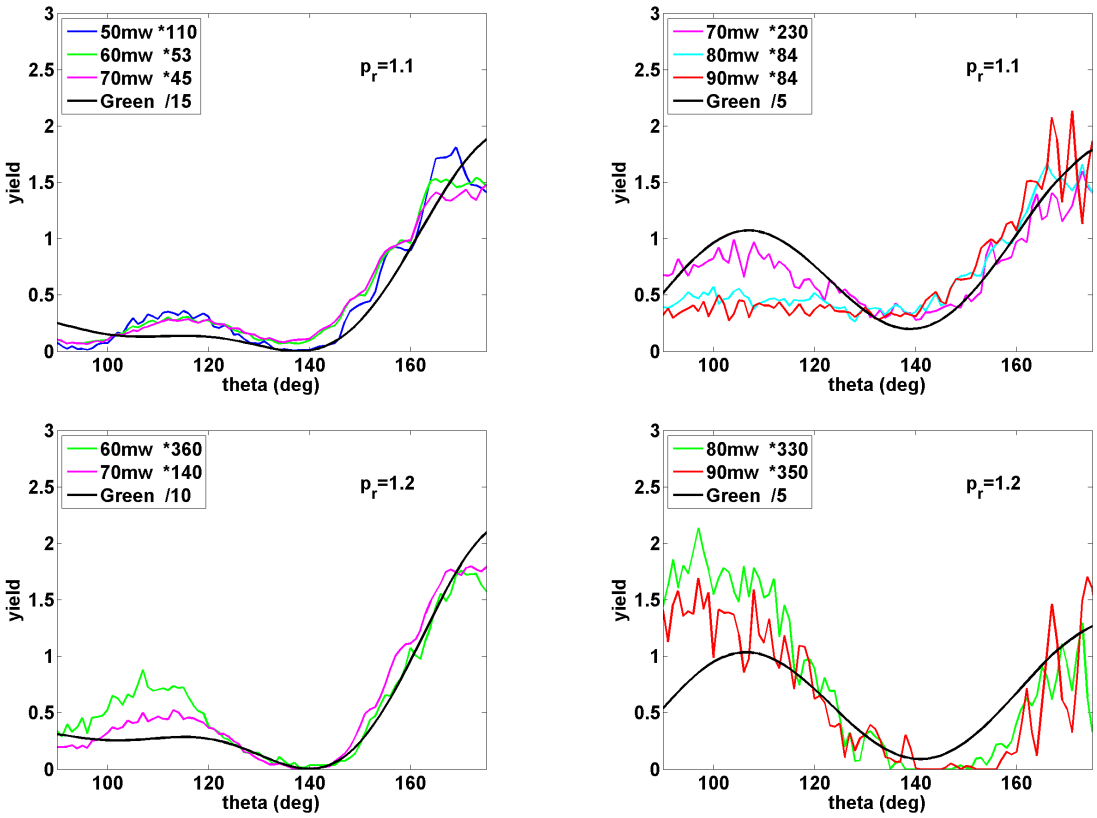

Figure 3.21: *(continued from Fig 3.21) The momenta of the back scattering electrons, p_r, are, from top to bottom, 1.1, and 1.2 a.u.*

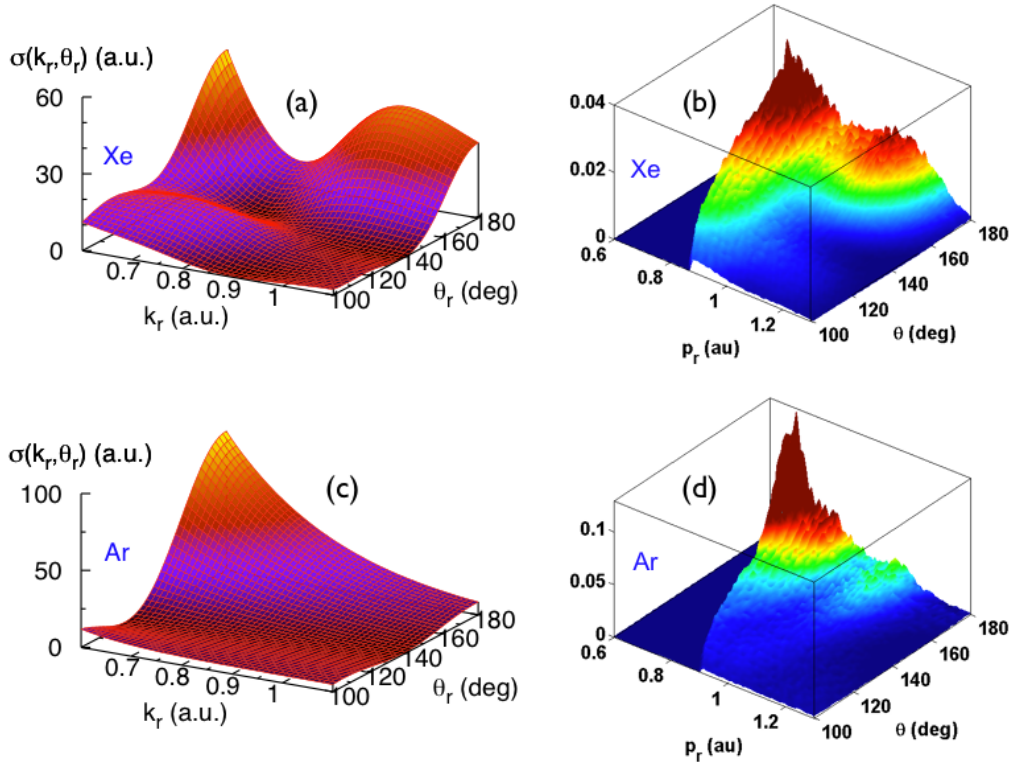

Figure 3.22: *Comparison of the theoretical DCS distribution with the experimental p_r-θ distributions for Xe and Ar. The left panel shows the DCSs and right panel the p_r-θ distributions. The DCSs are shown for (a) Xe and (c) Ar, the experimental p_r-θ distributions are shown in (b) Xe and (d) Ar. The angle θ_r in the theoretical plot is the same scattering angle as θ discussed in the text.*

Chapter 4

Complete Characterization of Two-color Pulses from Photoelectron Momentum Spectra

4.1 Abstract

The asymmetry of electron emission from single atoms by intense few-cycle 800 nm pulses is well known and forms the basis of the stereo-phasemeter method[9] of measuring the carrier-envelope phase of short pulses.In this chapter we present experiments which demonstrate a similar asymmetry caused by the superposition of two colors (800 and 400 nm) forming many-cycle pulses. We obtain Xe spectra as a function of the phase between the two colors. The spectra exhibit a pronounced asymmetry as a function of phase in both the "direct" and the "plateau" regions of electron energy. Recently established quantitative rescattering theory (QRS) allows us to analyze momentum images of the rescattering (plateau) high-energy electrons. Using QRS theory we attempt to determine accurately the laser peak intensity and the absolute phase of the two-color electric field.

4.2 Introduction

In the previous chapter the discussion has been focused on the interaction of atoms with a laser pulse with equal effective electric field amplitudes in both directions along the polar-

ization. If the shape of the pulse can be controlled such that the electric field directionality is preferentially one way or the other, the pulse can in turn be expected to influence the spatial direction of emission of the fragments from the laser-matter interaction. Thus a shaped laser pulse can be used to control the dynamics of light-induced processes. Such control experiments have been demonstrated in recent years using Carrier-Envelope Phase (CEP) locked few-cycle ultrashort laser pulses in study of both electrons[48] and ionic fragments[49]. A 5 fs laser pulse consists of less than two optical cycles. For such a pulse the phase of the carrier with respect to the envelope determines the directionality of the electric field. The electric field of the pulse can be written as

$$E(t) = E_0(t)\cos(\omega t + \phi) \tag{4.1}$$

where ϕ is the "absolute phase" between the carrier and envelope. For a standard commercially available pulsed laser source ϕ is usually random from pulse to pulse. Recent technological development however has enabled the stabilization and control of this "absolute phase".

The intuitive idea that the ionized fragments from an interaction of target atoms with such an asymmetric pulse will exhibit preferential emission in a certain direction forms the basis of such control studies (Fig 4.1). Before the advent of CEP stabilization similar coherent control experiments were demonstrated by creating pulse shaping using a relatively simpler tool: combining a laser pulse of central frequency ω with a second pulse with its central frequency at a higher harmonic (2ω or 3ω) and controlling the phase between the two to control the pulse asymmetry[8,50]. In this section we present experiments using such "two-color" ($\omega + 2\omega$) pulses. We combine 45 fs 800 nm and 400 nm pulses and control the relative phase between the two to generate an asymmetric pulse shape [Sec 2.2.3]. The total electric field can be expressed as

$$E(t) = E_1(t)\cos(\omega t) + E_2(t)\cos(2\omega t + \phi) \tag{4.2}$$

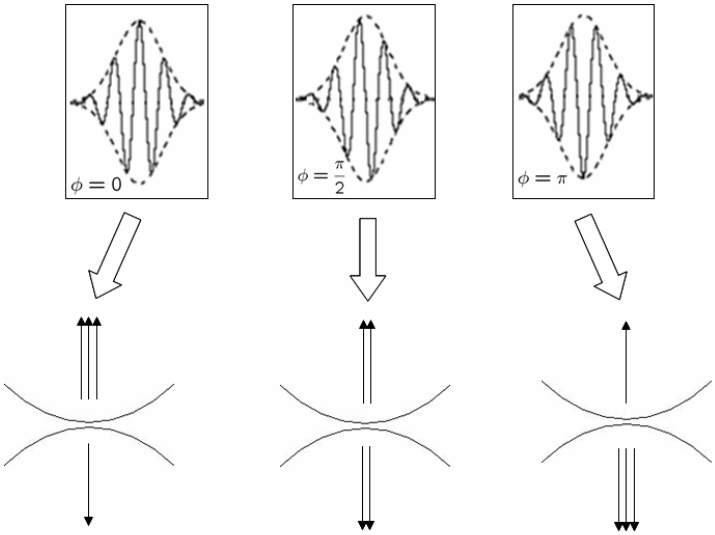

Figure 4.1: *Schematic figure depicting asymmetric ejection of charged fragments from atomic target on interaction with few-cycle CEP locked pulses. Figure modified from:G. G. Paulus, Laser Physics, 15, 6 (2005).*

where E_1 and E_2 are the envelope functions for 800 and 400 nm respectively, and ϕ is the relative phase between the two with respect to the second harmonic field. Fig 4.2 shows the two-color field (Eq. 4.2) and the vector potential at different values of the phase ϕ. The convention used throughout our discussion of two-color is that ϕ=0 depicts the maximum electric-field to be pointed along $+z$-direction.

The two-color method has proved to be a very reproducible and robust way to do electron localization experiments[51–53]. Field-free molecular orientation of simple heteronuclear molecules has also been successfully demonstrated using a two-color pump pulse[54]. This latter application has the potential to form the basis of future molecular-frame experiments. Thus "two-color" promises to be an extensively used tool in the near future. In order to use this tool it is vital to have a detailed characterization of the two-color pulse. The three components that determine the pulse shape are:(i) the peak electric field of 800nm E_1, (ii) the 800 nm and 400 nm electric field ratio E_2/E_1, and (iii) the *absolute* phase ϕ between the two colors .

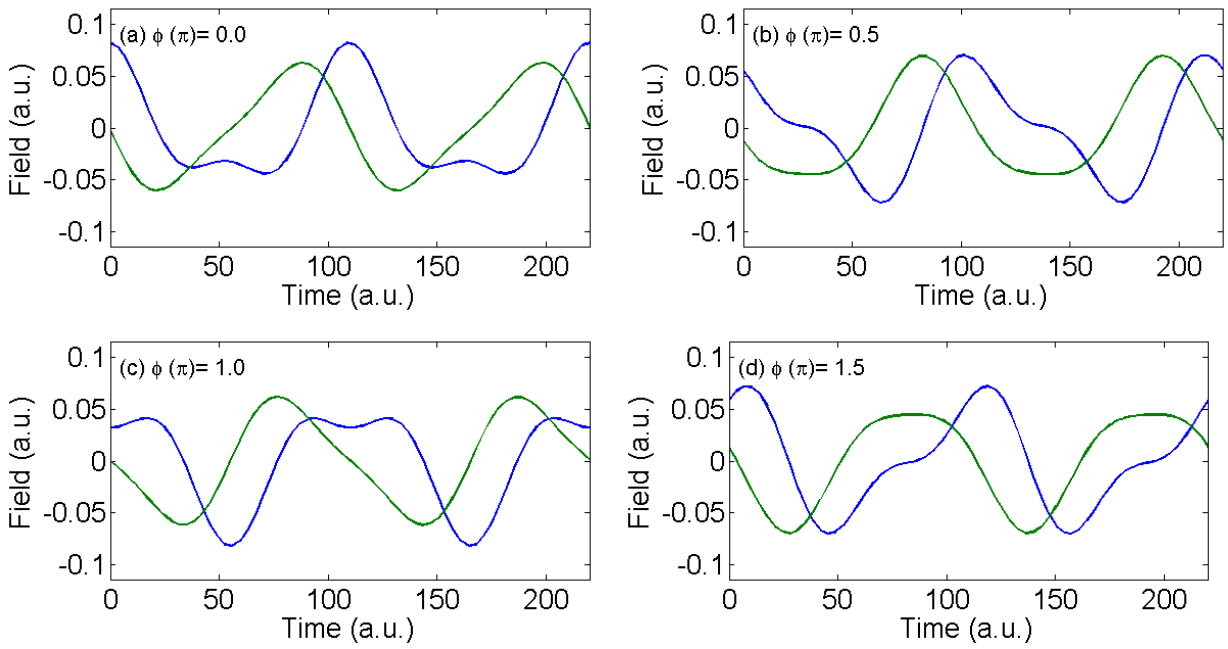

Figure 4.2: *Plots of the two-color electric field (blue) and vector potential (green) for two-color phase ϕ:(a) 0.0, (b) 0.5π, (c) 1π, and (d) 1.5π. The phase ϕ=0.0 corresponds to maximum electric field directed towards +z-direction.*

Prior attempts to calibrate the absolute phase of the two-color pulse were based on the measurement of asymmetric emission of the direct electrons from laser-atom interactions[8,55]. It appears intuitive that maximum emission of electrons to the left will occur when the two-color field is shaped so that it provides a maximum peak force on the electron and this force points to the left. Unfortunately, this intuitive idea is incorrect. The direction in which the electrons will finally go depends not on the field direction at the time of emission but the vector potential direction at this time. We can deduce from Sec 3.2.1 that the momentum gained by a direct electron in the laser field is equivalent to the vector potential at its birth phase (following Eq. 3.4, if we assume the electron to be initially at rest, and the vector potential at $t \to \infty$ to be zero, the momentum is found to be equal to vector potential at the birth phase). From Sec 3.2.1 it is also evident that maximum emission of direct electrons occurs when the electric field is maximum. At this time, however, the vector potential is zero [Fig 3.3]and thus an electron emitted at this time will classically have zero final ve-

locity. Any left-right asymmetry in the emission of electrons from a two-color field, phased to produce maximum field asymmetry, must result from small differences in the size of the vector potential before and after the field maximum. This makes it difficult to interpret the two-color phase from any intuitive interpretation of the direct electron behavior. Moreover the calculations of direct electrons[55] to compare with experiment in order determine the phase were done assuming $E_1 = E_2$, which was an approximation. To realize such equal peak fields experimentally an interferometric setup needs to be employed to control the two intensities separately. Another approach to calibrate the two-color absolute phase is to pass the two-color pulse through a second non-linear crystal (say KD*P) and measure the voltage generated across the crystal due to the non-linear process. This method also faces the problem that although it is an effective optical method to determine the phase it has limitations in predicting correctly the individual electric fields of the two-colors which will heavily depend on being able to accurately correlate the voltage variation to intensities. In this chapter, we propose to use our understanding of the rescattering phenomena in the laser-matter interaction and the recently developed quantitative rescattering theory[7] which numerically predicts this behavior to accurately determine the absolute phase of the two-color pulse and their individual peak intensities. We experimentally study the dependence of high-energy electron momentum spectra from Xe target on the phase of the two-color pulse. Comparison of the experimental spectra to the theoretical spectra generated using the QRS theory enables us to assign the experimental phase and peak intensities of the two-color pulse.

4.2.1 Semi-Classical Theory

By changing the two-color phase, the peak electric field and vector potential evolve smoothly. Thus the response of the photo-electrons ionized from a target atom interacting with the two-color pulse can also be expected to vary. One can predict the photoelectron energy to go through a maximum and minimum as a function of the two-color phase (Fig 4.4).

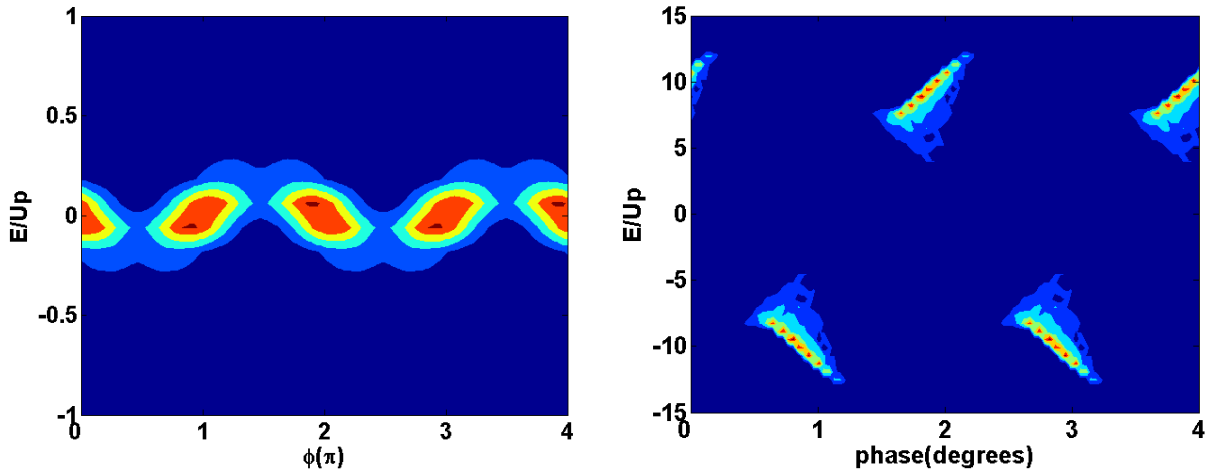

Figure 4.3: *Semi-classical calculation of photoelectron energy spectra as a function of two-color phase ϕ for electrons emitted in both positive and negative z-direction from an atomic hydrogen target. The positive E/U_p values represent electrons ejected towards the z-direction, and negative E/U_p values are electrons ejected in +z-direction (electrons are negatively charged). At $\phi = 0$ the peak electric field points in +z-direction. The image on the left shows the direct electrons, and image on the right shows the rescattered electrons.*

The probability of electron ionization depends on the amplitude of the electric field at the birth phase of the electron (given by ADK-rate), while the total energy gained by a rescattered electrons also depends on the value of the vector potential at the time of return (see Sec 3.2.1). Since both these factors play a role in determining the final energy the rescattered electron acquires on interaction with the two-color pulse, one cannot expect the asymmetry in electron emission to directly follow the direction of the force on the electron at the time of emission. So the critical question that needs to be addressed is: At what phase of the two-color field does the emitted electron acquires the maximum energy?

In order to get an insight into this issue a semi-classical calculation for the ADK-rate weighted ionization of the electrons as a function of the phase of the two-color field is carried out for both direct and rescattered electrons following the treatment discussed in Sec 3.2.1 (see Fig 4.3). The calculation of the rescattered electron involves the following steps: For a fixed phase ϕ of the two-color pulse the ADK-rate weighted electron emission probability for each birth phase is calculated. Now depending on the birth phase an electron

will have a particular return momentum and return time. Knowing the return momentum and the field vector potential at the return time, the rescattering energy of the electron can be calculated and an energy spectrum generated for that value of ϕ. Such an energy spectrum can now be calculated for different two-color phases ϕ to generate a energy vs. ϕ density plot of the electron yield.

The plot in the right panel of Fig 4.3 shows the results of this model calculation for a 800nm peak intensity of 1×10^{13} W/cm^2 and the E_2/ E_1 ratio of 0.33. The positive half of the E/U_p scale depicts electrons emitted along -z-direction while the negative half indicates electrons emitted in +z-direction (since the electron is negatively charged). We see the emission of electrons oscillate between +/- z-direction as a function of the two-color phase ϕ. The plot clearly indicates that the energy of the electrons ejected in -z-direction peak at a phase slightly away from $\phi = 0$: at about 50° (0.3π) of the two-color phase ϕ. After the maximum energy peak there is a sudden gap in the electron yield when the emission direction of the electrons is seen to switch abruptly.

The plot in the left panel of Fig 4.3 presents the distribution of direct electrons under the same conditions. The distribution shows a very high yield at an energy of zero. This is because most of the electrons are emitted when the field is maximum (governed by ADK rate) and the energy of the electron emitted at that time will be zero. The most interesting information that the model reveals is that there can be no asymmetry in electron emission for electrons emitted at ϕ=0,1π, 2π,... , ie when the field points maximally in any one direction. Rather the maximum asymmetry of the electrons is found to be generated at ϕ=$\pi/2$, $3\pi/2$, ... etc. At these phases there are many fewer electrons emitted, which would make it even harder to interpret any asymmetry response of direct electrons in experiments.

4.2.2 Quantum mechanical approach

A detailed theoretical simulation of the energy distribution of the photoelectrons ionized from Xe gas as a function of the two-color phase ϕ has been done by Z. J. Chen using the QRS model (see Sec 3.2.2). The photoelectron momentum spectrum for electrons backscattered at 180 ° was calculated for the modified electric field of the two-color pulse (Eq. 4.2) for a fixed phase. The energy spectrum was derived in turn from the momentum distribution. Such an energy spectrum was calculated for different values of the two-color phase ϕ to generate an energy vs. ϕ density plot of the electron distribution.

4.3 Experimental observation

We generate a two-color field using a collinear setup, as described in detail in Sec 2.2.3. A horizontally polarized 45 fs pulse with central wavelength at 800 nm is passed through a BBO crystal which generates a second harmonic 400 nm component due to its nonlinear properties. This 400 nm field has vertical polarization, and also is delayed from the 800 nm pulse by about 60 fs. Both 800 nm and 400 nm pulses are subsequently passed through a zero-order quartz plate which acts as half wave-plate for 800 nm and rotates its polarization by 90 °, but acts as full wave-plate for 400 nm. So the beam exiting the quartz plate has both components with polarization along the vertical. A birefringent calcite crystal is placed between the BBO and quartz plate to compensate the delay between the two pulses such that they exactly overlap where the beam is focused on the gas jet. The relative phase between the 800 nm and 400 nm is controlled by rotating the calcite crystal about an optical axis using a motorized rotation stage in steps of 0.05 fs (see Fig 2.2).

A spherical mirror of focal length 75 mm is used to focus the pulses to intensities of 0.5-2X10^{14} W/cm^2 onto a neutral Xe gas jet. The ionized electrons are momentum imaged onto a MCP-phosphor assembly of the VMI chamber (Sec 2.4). The momentum images are averaged over many shots by a camera sitting outside the chamber looking at the phosphor screen.

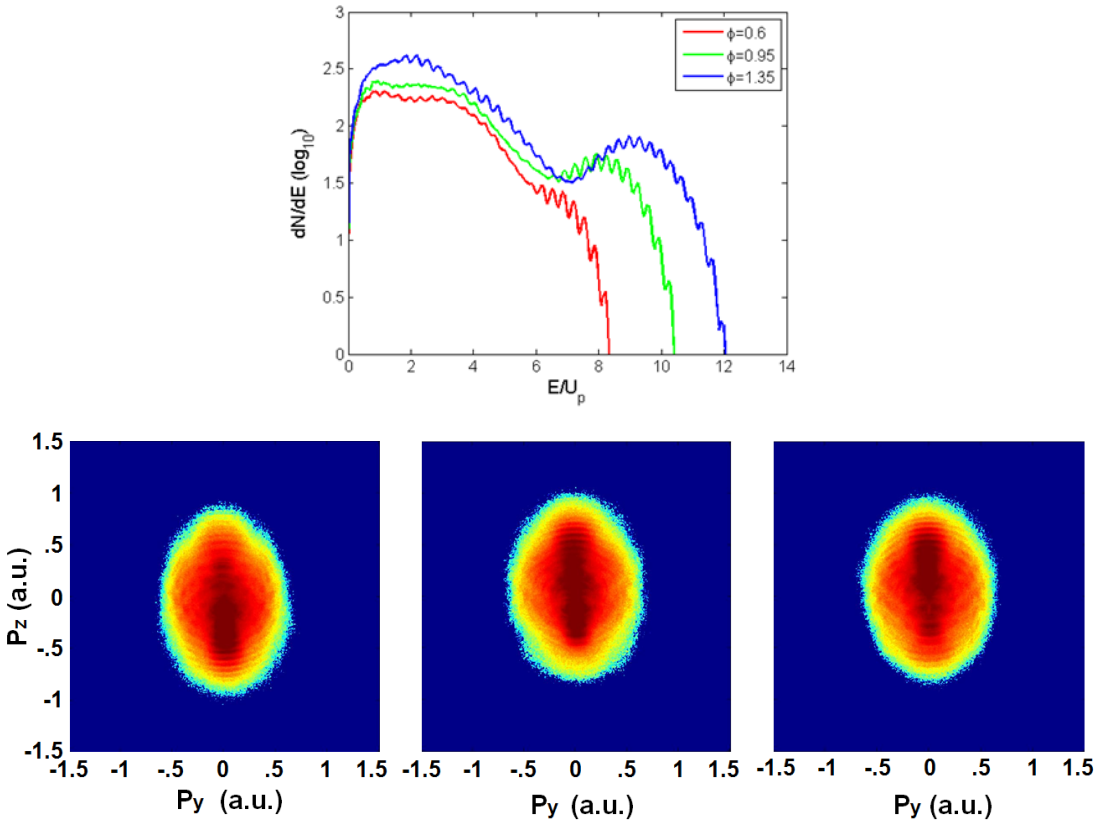

Figure 4.4: *The upper panel shows electron energy spectra from a Xe target integrated over 10° angle around the polarization direction. The three spectra are at three different values of the 800 nm - 400 nm relative phase (in units of π) which gives maximum (blue), minimum (red), and zero asymmetry of electron ejection in the -z-direction. The lower panel shows corresponding VMI images of electron momentum spectra at the same relative phases creating maximum asymmetry in (a) -z (corresponds to blue plot on energy spectra), (c) +z-direction (red graph) ,and (b) zero asymmetry at a phase in between (green plot).*

A typical photoelectron momentum spectrum from a Xe target as imaged in a VMI arrangement is shown in Fig 2.10 where the laser polarization is along z-axis. As we scan the phase between 800 nm and 400 nm the electron distribution maximizes alternately towards '+' and '-' z-directions as a function of the phase as shown in Fig 4.4. To be consistent with our axis-convention throughout, the two-color phase ϕ=0 corresponds to the peak electric field pointing maximally in +z-direction.

The raw image as acquired on the phosphor screen is a 2D projection of the interaction

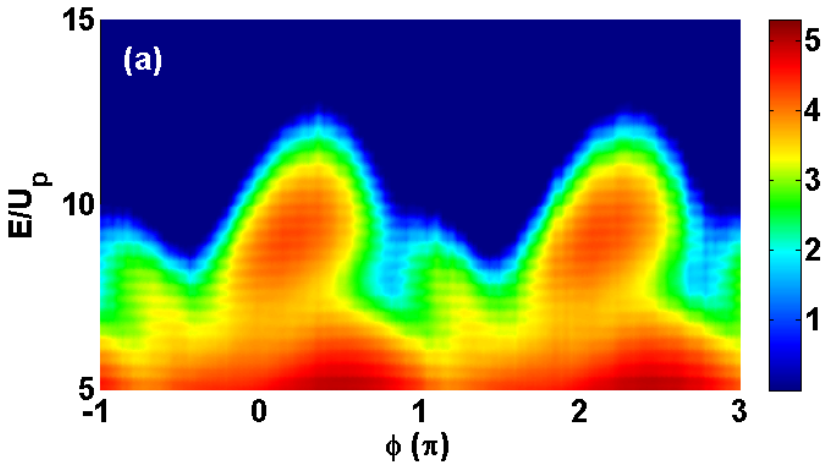

Figure 4.5: *Density plot showing dN/dE distribution of rescattered electrons from Xe gas as a function of absolute phase ϕ between 800 nm and 400 nm in the -z-direction.*

momentum distribution. The p_z-p_y momentum slice is extracted from the projection using an iterative inversion algorithm [Section 2.4.3]. The photoelectron momentum distribution is integrated over an angle of 30 ° about the z-axis at each phase step. The energy spectrum (dN/dE) is calculated for each phase. A compilation of such spectra for different phases generates a dN/dE distribution plot as a function of energy and phase (ϕ). [Fig 4.5] shows the resulting spectrum for photoelectrons ejected in the -z-direction. It is sufficient to focus on the variation of the rescattering towards any one side (say -z-direction) in order to compare it with theoretical predictions and retrieve the field characteristics from it.

4.4 Results and discussions

Fig 4.6 shows a comparison between theoretical calculations and the experimental distribution of rescattered photoelectrons from a Xe target in the two-color field, over the range of $5U_p$ to $15U_p$, ejected towards -z-direction. Fig 4.6(a) is the same spectrum shown in Fig 4.5, Fig 4.6(b) shows a TDSE calculation for a peak intensity of 0.6 $\times$ 10^{14} W/cm^2 of 800nm pulse and E_2/E_1 ratio of 0.3, and Fig 4.6(c) presents the volume integrated QRS calculation

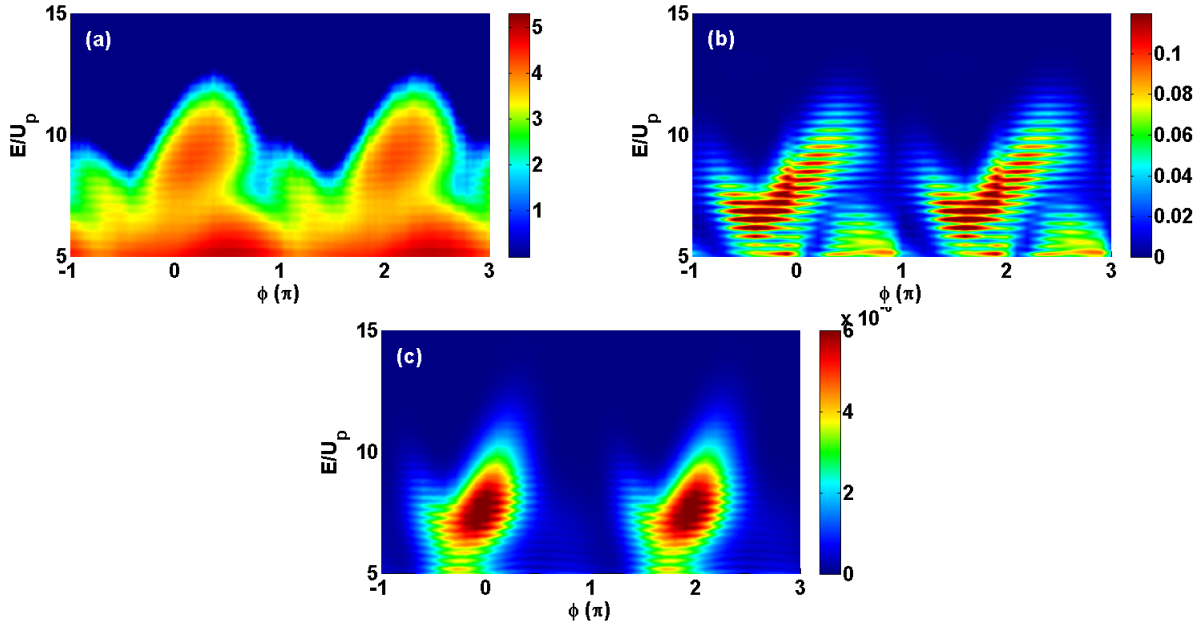

Figure 4.6: *Density plot showing dN/dE distribution of rescattered electrons (over the energy range of 5 to 15 U_p) from Xe gas as a function of absolute phase ϕ between 800 nm and 400 nm in the -z-direction acquired from: (a) experiment (same as Fig 4.5); (b) TDSE calculation for an intensity of 0.6 × 10^{14} W/cm^2, and (c) QRS theory for a peak intensity of 0.76 × 10^{14} W/cm^2 (volume integrated).*

of the same at a peak intensity of the 800 nm component of 0.76 $\times 10^{14}$ W/cm^2.

The QRS theory is an approximation involving interaction of the electron wave packet with the atomic potential. Thus it is valid for the high energy rescattered electrons only. The distribution of the low energy electrons generated by QRS calculation should not be compared to the experimental direct electron distribution. Thus the comparison of the three spectra is done only for the high energy electrons ($5U_p$ to $15U_p$). The QRS spectra are calculated at each two-color phase only for electrons rescattered along 180°, while the experimental data is integrated over 30° angle about the polarization. The validity of this comparison is checked by comparing rescattered electron spectra for different scattering angles at a fixed two-color phase. The energy spectra for different scattering angles less than ±15° are found to be identical, thus rendering an angle integration redundant.

The theoretical spectrum for a given peak intensity cannot be exactly compared to exper-

iments. Due to the tight focusing of the laser pulse onto the gas jet, the total contribution in the spectra is due to a range of intensities present within the interaction volume. A more realistic spectrum can thus be generated by assuming a spatial intensity distribution of a Gaussian beam and volume integrating the theoretical spectra over a small volume. This volume integration has been taken into account for the QRS calculation.

The TDSE calculation is, however, extremely tedious. In order to do a volume integration the generation of spectra for many intensities is necessary. It is not practically feasible to do so for the TDSE calculation, so the volume effect is not taken into account. However it needs to be noted that the maximum yield contribution from such a Gaussian beam interaction with a gas volume does not occur from the peak intensity of the pulse, but comes from a lower intensity. In fact, the electron yield contribution from the peak intensity is close to zero since it covers a very small volume and thus interacts with negligible gas volume. The yield distribution as a function of intensity for a given peak intensity has been calculated (Fig 4.8). A similar calculation for a peak intensity of 0.76×10^{14} W/cm^2 shows that the "effective intensity" is 0.6×10^{14} W/cm^2. The TDSE calculation is carried out for the effective intensity in order to achieve best agreement with the experiment.

The oscillatory feature of the emission of rescattered electrons from atom by the two-color field as predicted by semi-classical model is reproduced by QRS and TDSE calculations. The salient features in all three calculations agree. As predicted by the classical calculation the energy of the electrons peaks at a phase $\phi > 0$ (approximately at 0.4π). An abrupt gap in the electron yield is seen over the phase of 0.7π to π (shortly after the energy maximum is reached). This feature, also seen in the classical calculation was attributed to a sudden switch in the direction of electron ejection. A clear energy minimum is observed at 1.7π, well defined by a clear trough in the electron yield. All of the above features are also seen in the experimental spectrum.

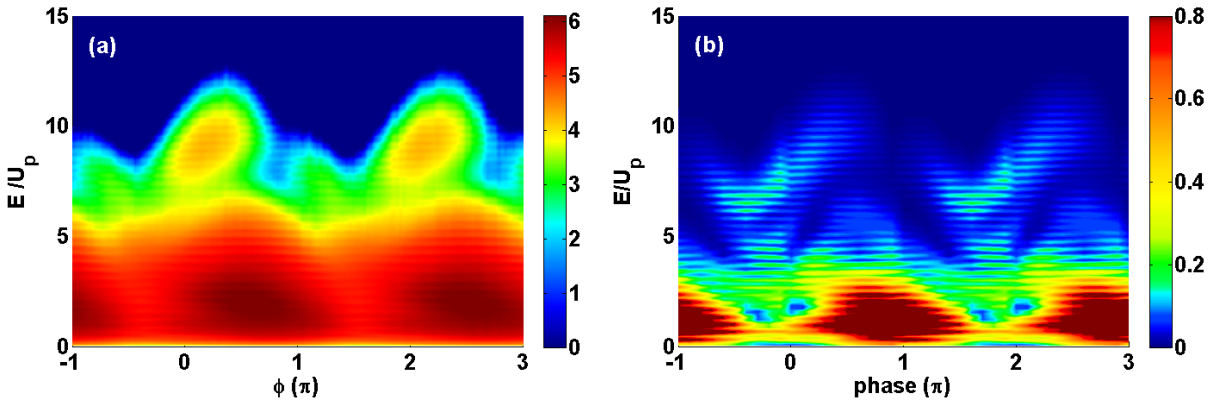

Figure 4.7: *Density plot showing dN/dE distribution of both direct and rescattered electrons (0 to 15 U_p of electron energy) from Xe gas as a function of absolute phase ϕ between 800 nm and 400 nm in the -z-direction acquired from: (a) experiment (same as Fig 4.5); (b) TDSE calculation (same as Fig 4.6).*

4.4.1 Discussion of low energy electrons by comparison with TDSE calculations

As mentioned earlier, the QRS theory was developed for rescattering electrons only and cannot generate the direct electrons. In order to do a self-consistency check we compare the experimental distribution of direct and rescattered electrons with the same from TDSE calculation.

Fig 4.7 shows the experimental Xe two-color spectrum (same as Fig 4.5)) for the energy range of 0 to 15U_p and (b) a TDSE calculation over the same range (same as Fig 4.6). The low energy peaks for the TDSE calculation appear near ϕ=π, 3π. The phase assigned to the experimental data by aligning the energy maximum and minimum for the rescattered electrons to the QRS simulation also makes the experimental low energy peak appear slightly below ϕ= π, 3π.

The TDSE calculation reproduces all the major features of the experiment for both the low and the high energy electrons. The differences in the two plots can be due to the fact that the TDSE calculation is not volume-integrated over all the intensities present in the focal volume. The calculation is done for a single intensity of 0.6 $\times$ 10^{14} W/cm^2. Also the pulse

length is assumed to be 10 fs for the calculation since the TDSE calculation for a longer pulse require much more computational time. In the experimental plot the direct electrons have energies all the way up to $5U_p$ while for the spectrum from TDSE the direct electrons appears to have energies up to $4U_p$. This is possibly due to the fact that the TDSE is done for the "effective intensity" that best reproduces the major features. But for the experimental spectrum there is also some contribution (however small and decreasing rapidly) from the higher intensities all the way up to the peak intensity. The relative contributions from the different intensities in the interaction volume is estimated theoretically as shown in Fig 4.8.

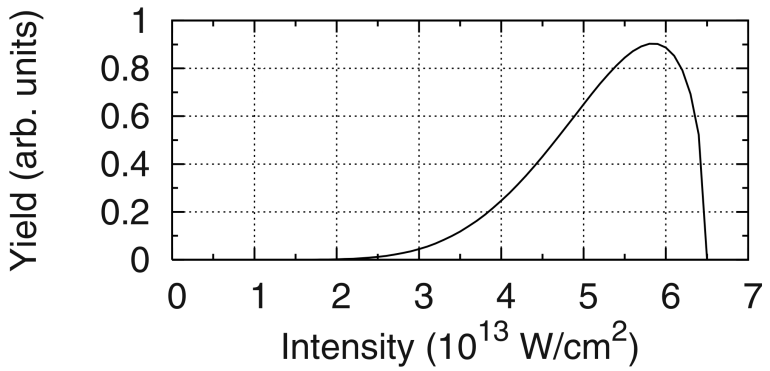

Figure 4.8: *The calculated relative contributions of different laser intensities in the laser volume to the electron yield from single ionization of Xe by a 8 fs laser pulse. For the laser peak intensity of* 0.65×10^{14} *W/cm*^{2}*, the maximum electron yield occurs from a volume where the intensity is 0.59* $\times$ 10^{14} *W/cm*^{2}

.

4.4.2 Complete pulse characterization

In order to assign the correct absolute phase to the experimental dataset we compare the major features of the experimental and QRS electron distributions. Now an appropriate offset phase adjustment is made to the experimental spectrum so that the phase of the maximum energy and the minimum energy features matches those of the theory plot.

The determination of the electric field peak ratios is more of an iterative process. From the

maximum and the minimum of the rescattering energy oscillation a mean can be obtained. The cutoff corresponding to this mean spectra should approximately indicate the $10U_p$ cutoff of the 800nm field. Now the approximate E_2/E_1 field ratio can also be estimated from the size of the energy oscillation and a final accurate match is usually obtained after a few iterations.

Fig 4.6 shows the experimental electron distribution from Xe for certain pulse parameters and compares it with its QRS equivalent. The QRS plots reproduces the experimental data well. The absolute phase scale has already been assigned to the experimental plot. From the QRS calculations we can also conclude that the pulse parameters used for the experiment are: $0.6X10^{14}$ W/cm^2 peak intensity of 800nm, and E_2/E_1 ratio of 0.3.

4.4.3 Validity of QRS theory for two-color pulses and discussion of approximations

The comparison of experiment, TDSE and QRS theory [Fig 4.6] confirms that the QRS theory effectively reproduces the behavior of the high energy rescattered electrons. The necessity of an iterative process to determine the peak ratios for a given two-color scan emphasizes the need of a fast method of numerical calculation without having to compromise on accuracy. The two-color pulse parameters can be determined fairly quickly using QRS theory. Further, QRS theory has the advantage of being able to do a volume-integral to account for the contribution from the different intensity profiles in the spatially inhomogeneous laser focus. This on the contrary would be extremely tedious and impossible for all practical purposes in case of a TDSE calculation.

However our calculations are based on a major assumption that the two colors focus the same way having the same focal waist. In reality, if the two colors have the same collimated beam diameter at infinity the 400nm pulse focuses tighter. This approximation was verified by doing QRS calculation for a one set of pulse parameters considering the actual spatial intensity distribution. The result was found to be only a small correction on the approximate calculation and thus can be left out.

4.4.4 Conclusions

Prior attempts at determining the absolute phase of the two-color field involved a detailed study of the yield of the low energy direct electrons. Extensive study and interpretation of the behavior of ionization fragments in a two-color field were done by Sheehy *et al*, and Thompson *et al*[8,56] under the basic assumption that direct electron ejection follows the electric field. They assumed that at ϕ=0 the electrons will be maximally directed in the direction of the force at the time of emission.

The semi-classical calculation for direct electrons has revealed that maximum electrons are ejected when the field is at a maximum but the drift energy of these electrons is zero. The calculation shows symmetric electron ejection at ϕ=0,π. A very low yield of higher energy direct electrons are produced at a phase away from ϕ=0. This low yield can be expected to pose problems in detecting them experimentally. Although the zero energy symmetric electron ejection about ϕ=0 predicted by classical calculation does not agree with experiment or the quantum mechanical calculation, and thus should not be taken too seriously, the fact remains that the zero vector potential when maximum direct electrons are born makes it difficult to interpret their final outcome. This emphasizes the danger of focusing on the direct electron ejection for the two-color phase calibration purpose.

Moreover TDSE and QRS calculation (and also our experiment after phase assignment from rescattered electrons) corroborate that the assumption that the electrons will be preferentially observed along the direction the force points at the time of emission is incorrect. Thus all the discussion about "intuitive electron ejection and "non-intuitive direction of ion ejection are based on an incorrect premise. Interestingly Schumacher *et al.*[55] claimed to have experimentally observed the ejection of low energy electrons along the electric field similar to others, but also observed the emission of high energy electrons at phases away from ϕ=0. They vaguely attributed this observation to "three-step-model"-type phenomena but were not well equipped yet to do a thorough calculation. Charron *et al.*[57] also did calculations which showed a phase shift between the field phase and the asymmetry in the ion emission

but did not have any experiments to verify their claim.

Present day experimental techniques and computing abilities have allowed us to study the high energy rescattered electron behavior in the two-color field and compare them with detailed theoretical calculations. The rescattered electrons have shown robust response to the variation of the two-color field. The features are reproduced both by semi-classical and quantum calculations. Quantitative Rescattering Theory allows us to use the rescattered electron behavior to calibrate all two-color experiments and also characterize the pulse parameters.

4.5 Summary

We have measured the variation in the ionization of a Xe gas in an intense two-color field as a function of the absolute phase of the field. Major features of the rescattered electron response are reproduced by a quantum mechanical calculation using the recently developed QRS theory. The features can be well understood with the help of the classical "three-step model". The detailed QRS calculation enables us to accurately characterize the pulse parameters.

Chapter 5

Asymmetric dissociation of H_2 and D_2 molecules by a two-color field

5.1 Abstract

We measure the ionization of D_2 and H_2 molecules using a linearly polarized two-color (800 nm and 400 nm) pulse. The ion yields ejected in opposite directions along the polarization vector show clear asymmetry as a function of two-color phase. The asymmetry effect was found to be quite different in the different ion-energy regions traditionally known as bond softening, above-threshold dissociation and rescattering. The simulation of time-dependent Schrödinger equation reproduces the experimental results.

5.2 Introduction

In the previous chapters we have focused on the interaction of atoms with short intense laser fields. Interaction of the same laser field with molecules is, in general, a much more complex phenomenon. Short, intense laser pulses can fragment molecules via a variety of mechanisms. Controlling the fragmentation pathways by controlling the shape of the laser pulse has drawn immense interest in present day ultrafast research[8,49,56,58–60]. Rather than steering the motion of the ionized electron already in the continuum, as has been discussed in the previous chapter, now we attempt to steer the bound electron during the dissociation process thereby controlling the outcome of the dissociation itself.

It is often useful to restrict ourselves to the simplest of molecules for such intense laser-matter studies. The hydrogen and deuterium molecules and their molecular ions thus have served as the most commonly studied molecules both experimentally and theoretically[60–64]. In spite of being the simplest of molecules, D_2 (or H_2) has revealed a variety of intriguing processes when excited with an intense laser field. A lot of research has been invested in trying to shed light on the different fragmentation mechanisms possible in these molecules. Research dedicated for over two decades towards understanding these fragmentation pathways has been successful in revealing the mechanisms involved, such as: bond softening (BS)[65], above-threshold dissociation (ATD)[65], charge resonance enhanced ionization (CREI)[66,67], and rescattering ionization (RES)[25,68]. Fig 5.1 depicts schematically the pathways corresponding to the above processes. Through single ionization the wave packet can be launched on the g potential and allowed to propagate. When the wave packet reaches close to the outer edge of the curve it can absorb a single IR photon and dissociate through the u curve (orange line) giving rise to ion emission through the bond-softening (BS) channel. This is the lowest energy channel. Alternately it can absorb three photons and emit one photon to dissociate via g curve (above-threshold ionization). This channel creates ions with a slightly higher energy (ATD; green curve). Finally, the wave packet can be excited early on due to recollision with the returning electron and subsequently dissociate via the u curve creating

the highest energy ions (RES). Double ionization can occur through laser-induced further ionization when the wave packet is near the outer turning point. This produces a broad Coulomb explosion peak (CREI) (from two D^+ ions) with an ion energy between that for RES or ATD.

Equipped with this thorough understanding of the intrinsic processes we now attempt to control the dissociation pathways by using a shaped laser pulse. Attempts have been made, as early as a decade ago, to demonstrate control in the dissociation of molecules using a two-color pulse[8,56]. Asymmetric ejection of ions in opposite directions along the laser polarization from molecular targets was observed successfully establishing such control. Sheehy *(et al.)*[8] observed such an asymmetry in HD with long(ps) pulses. A similar result was found by Thompson *et al.*[56] with much shorter (100 fs) pulses and high intensities. Both groups reached the same inference that the ions seemed to be preferentially emitted when the two-color phase is such that the electric field at the time of emission was maximum and directed opposite the favored ion emission direction ("non-intuitive" direction). This conclusion was based on the assumption that the (low-energy) electron emission was in the "intuitive direction[55]. Moreover the conclusion was drawn based on the overall directionality of ions ejected at all energies without attempting to understand any dependence on the dissociation mechanism. A physical explanation for the same was proposed by Posthumous *et al.*[58]. More complete theoretical analyses[57,69] explained the observation that the electrons and ions were observed to be emitted in the same direction, but concluded that it was the electrons, not the ions, which were emitted in the "non-intuitive direction. These calculations also showed that the ion emission asymmetry was expected to be very ion-energy dependent, but there was no data on this issue with which to compare this aspect of their theoretical results.

A more recent experiment by Kling *et al.*[49] using few-cycle CEP-locked pulses revealed a strong asymmetry in the emission of D^+ ions from D_2 molecules. The ions exhibiting asymmetry were found to be quite high energy and the creation of the these ions was attributed

to the rescattering process, which is known to produce D^+ ions with high energy. But no asymmetry was observed in the low energy channels.

The key questions that arise on reviewing these studies are: (i) What is the ion-energy dependence of the asymmetric dissociation? (ii)Should we expect to see any asymmetry in the low-energy channels? These are the motivations behind the work presented this chapter. Here we present experiments using two-color laser field to produce asymmetry in the emission of D^+ (and H^+) ions from D_2 (and H_2) molecules, with a focus on the ion-energy dependence of the asymmetric ejection.

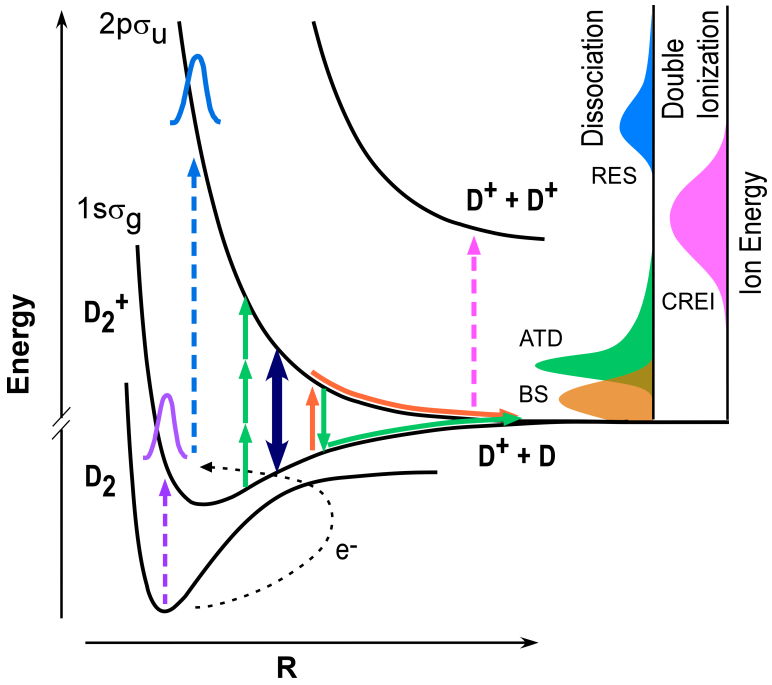

Figure 5.1: *Schematic of dissociation processes for D_2 (not to scale). Traditional BS and ATD processes are indicated by thin arrows. The additional process enabled by the second harmonic is indicated by the thicker double ended arrow. Rescattering is indicated by a blue dashed arrow.*

5.2.1 Theory

The D_2^+ ion created by single ionization of the D_2 molecule consists of two identical nuclei and one electron. Since the motion of the electron is much faster than that of nuclei, the nuclei can be considered stationary when describing the motion of the electron. This approximation, called the Born-Oppenheimer (or adiabatic) approximation[70], allows us to treat the nuclear motion and the behavior of the electron in the nuclear potential separately. Thus the full wavefunction for the D_2^+ ion in terms of its lowest-lying electronic states can be expressed as

$$\Psi(\mathbf{r}, R, t) \approx \Phi_g(\mathbf{r})\chi_g(R, t) + \Phi_u(\mathbf{r})\chi_u(R, t) \tag{5.1}$$

where R is the internuclear distance, $\mathbf{r}$ is the electronic coordinate, $\Phi_g(\mathbf{r})$ and $\Phi_u(\mathbf{r})$ correspond to the two lowest-lying $1s\sigma_g$ and $2p\sigma_u$, and $\chi_{g,u}(R, t)$ are the two corresponding nuclear wavefunctions. Both $\Phi_g(\mathbf{r})$ and $\Phi_u(\mathbf{r})$ depend parametrically on R.

The potential curves V_g and V_u (for $1s\sigma_g$ and $2p\sigma_u$) under the BO-approximation can be expressed as

$$V_{g,u} = \frac{1}{R}\frac{(1+R)\exp(-2R) \pm (1-2R^2/3)\exp(-R)}{1 \pm (1+R+R^2/3)\exp(-R)} \tag{5.2}$$

where '+' corresponding to V_g represents a bound state and '-' correspond to V_u gives a repulsive one. A schematic of these potential curves for $1s\sigma_g$ and $2p\sigma_u$ is drawn in Fig 5.1. The dissociation of D_2^+ is described by a theoretical model calculation. The procedure is very similar to that used Charron *et al.*[57] and Chelkowski *et al.*[69].The time-dependent Schrödinger equation is solved for χ_g and χ_u

$$i\frac{\partial}{\partial t}\begin{pmatrix} \chi_g \\ \chi_u \end{pmatrix} = \begin{pmatrix} T_R + V_g(R) & D_{gu}(R)E(t) \\ D_{gu}(R)E(t) & T_R + V_u(R) \end{pmatrix}\begin{pmatrix} \chi_g \\ \chi_u \end{pmatrix} \tag{5.3}$$

where $T_R = -\frac{1}{2\mu}\frac{\partial^2}{\partial R^2}$, $E(t)$ is the two color electric field, and μ is the reduced mass of the nuclei. The dipole coupling between g and u states is given by $D_{gu} =< \Phi_g|er|\Phi_u >$. The g and u components of the dissociative wave function were derived and projected onto the '+' and '-' atomic states

$$\chi_+(R) = \frac{1}{\sqrt{2}}\left[\chi_g(R) + \chi_u(R)\right] \tag{5.4}$$

$$\chi_{-}(R) = \frac{1}{\sqrt{2}} \left[\chi_g(R) - \chi_u(R)\right] \tag{5.5}$$

The specific calculations shown in this thesis were carried out by Dr. Feng He[71,72] using the formalism introduced above. The neutral molecule is ionized and the wave packet is launched onto the 1sσg curve almost at the peak of the laser field. Only two wave packets from two successive electric field peaks directed in opposite directions along the polarization are launched, with relative weights given by the ADK ionization rate. The resulting probabilities are added incoherently, under the assumption that the ionized electron destroys the phase coherence of the nuclear wave packets. The energy spectrum is obtained by Fourier transforming the wave functions going to the '+'-direction and '-'direction. The asymmetry parameter is defined as

$$A = \frac{|\tilde{\chi}_{+}|^2 - |\tilde{\chi}_{-}|^2}{|\tilde{\chi}_{+}|^2 + |\tilde{\chi}_{-}|^2} \tag{5.6}$$

The asymmetry in the rescattering energy region cannot be calculated directly from this model-calculation. However, with some further modeling to account for the additional excitation by electron-scattering it is possible the calculate the response of this region. In this modified version, the same wave packet discussed above is launched onto the 1sσg curve and is allowed to evolve for 2/3 of an optical cycle (the return time for the rescattering electron) before moving it up suddenly to the 2pσu potential curve. Solving the same two-state Schrödinger equation starting with this wave packet produces an evolving wave packet on the coupled g and u potentials, resulting in dissociation from both curves. The two-color electric field coupling the potentials will determine the amplitude ratio on the two curves. This mechanism follows the same idea as the explanation proposed in Kling *et al.*. In short, as the dissociation proceeds, the electron wave function becomes "localized" on one side or the other when the interatomic barrier rises sufficiently to block further oscillation back and forth[73,74].

The theoretical density plot of the results shows much complicated fine structure within each major peak, producing a very complex asymmetry map not easy to interpret. To make

it more realistic and comparable to the experimental conditions, volume averaging for the contribution of the range of intensities from a Gaussian profile is incorporated. This removes all the fine structure and the overall effects are then compared to experiment.

5.3 Experimental observation

We generate a two-color field using the collinear setup described in Sec 2.2.3. The vertically polarized 800 nm and 400 nm pulses from the output of the two-color optics set-up are focused by the back- focusing mirror onto the molecular gas target. The 800nm pulse intensity is varied from 1-3X10^{14} W/cm^2. The ion fragments are momentum imaged onto a MCP-phosphor assembly of the VMI chamber. A fast HV transistor switch is used to gate on ion-fragments with a specific mass- to-charge ratio. To be able to do that the time-of-flight spectrum is observed in real time on the oscilloscope. By adjusting the delay of the HV switch with a Stanford Delay Generator with respect to a trigger pulse (picked up from scattered laser pulse with a photodiode) the switch timing is adjusted to gate on the desired fragments. The momentum images of D^+ (or H^+) are captured averaged over 30 s by the camera focused through a glass window on to the back of the phosphor screen from outside the vacuum chamber (Sec 2.4.1).

A typical D^+ momentum image is shown in Fig 5.2. The laser polarization is along z-axis pointing vertically up. The electric field maximum peaks towards the +z direction at $\phi = 0$ of two-color phase; the y-axis along the horizontal is the laser propagation direction and the x-axis is directed into the image plane, which is consistent with the fact that the fragments fly towards the detector along the positive x-axis. This is consistent with our axis convention throughout the thesis.

The p_z-p_y momentum spectrum is extracted from the 2D projection as acquired on the phosphor screen using Abel-inversion algorithms (Section 2.4.3). The dN/dE-distributions of D^+ (or H^+) ions are plotted as a function of phase ϕ integrated over an angle of 30 °

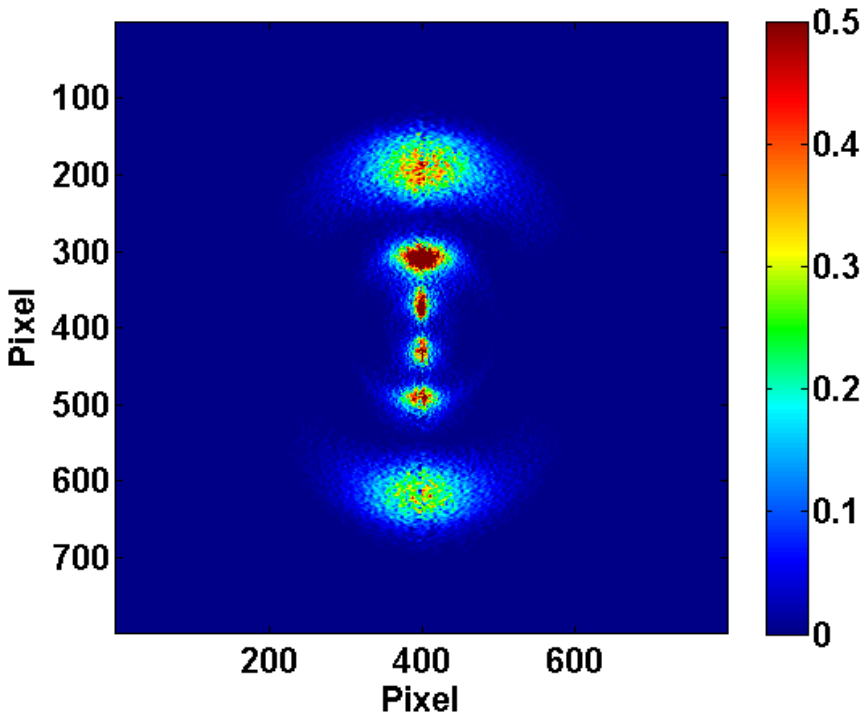

Figure 5.2: *VMI images of D^+ momentum spectra at an arbitrary two-color phase of the two-color field. The co-ordinate system is indicated. The positive z-axis, and therefore peak electric field $\phi = 0$, points vertically up; the y-axis, that is laser propagation direction, is towards the left; and the x-axis points inward.*

about the polarization axis from the momentum image at each phase step.

Keeping in mind that this is a 2D projection of the 3D interaction distribution (Section 2.4) it can be pointed out that the symmetry center of the image represents the interaction center. So the upper half of the image consists of fragments ejected in +z-direction while the lower half are those ejected in -z-direction from the interaction region. For a symmetric electric field of the laser pulse the yield along either end of the polarization vector, i.e. along '+' and '-' z-direction, have equal probability. When a two-color pulse interacts with the target the overall shape and directionality of the electric field varies as a function of the phase and subsequently the ion yields in the +/- z directions can also be expected to vary accordingly. An effective way to look at this up-down asymmetry in yield along the

polarization is to measure the difference between the +z/-z yield normalized to the total yield as a function of ϕ and ion-energy E:

$$A(E,\phi) = \frac{Y_+(E,\phi) - Y_-(E,\phi)}{Y_+(E,\phi) + Y_-(E,\phi)} \tag{5.7}$$

where Y_+, and Y_- are yields along +z and -z-directions respectively. The absolute phase ϕ between the two colors was assigned from the measurement and analysis of backscattering electrons yield from Xe as described in the previous chapter.

5.4 Results and discussions

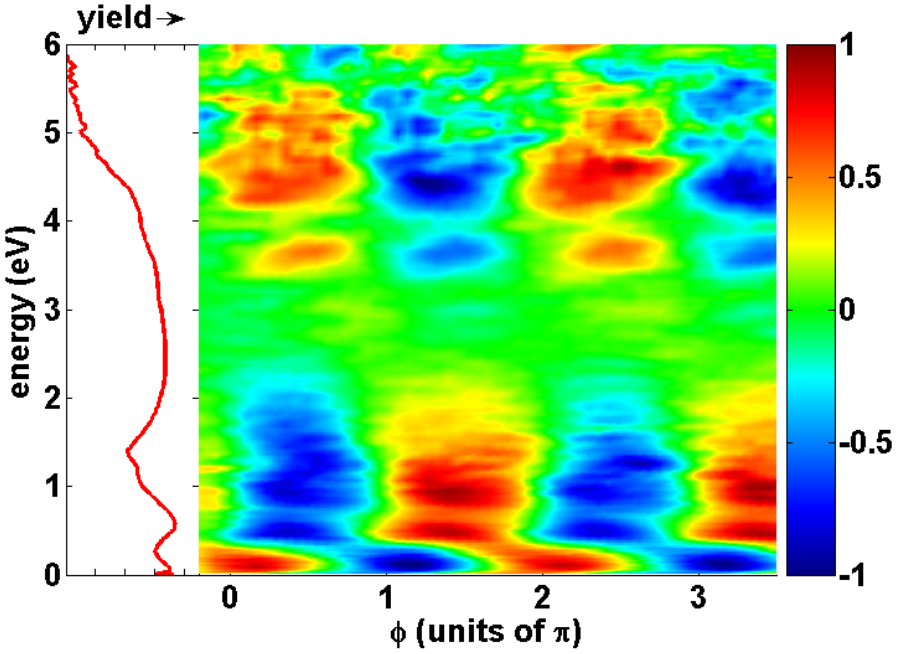

Figure 5.3: *The left hand panel shows the energy spectrum (log plot): the total ion yield as a function of ion energy with decades indicated by tick marks. The density plot represents the asymmetry of D^+ ion emission from D_2 as a function of ion energy and phase ϕ between 800 and 400 nm radiation.*

The density plot in Fig 5.3 shows the asymmetry of D^+ ions over the entire energy range of 0 to 6 eV. The left panel indicates an energy spectrum of D^+ ions, with the yield

integrated over 2π phase. The different peaked features in this plot correspond to the different mechanisms described in Fig 5.1: the "one photon" or BS (0-0.3 eV), the "two photon" or ATD (0.3-2 eV), the rescattering (4-6 eV) and the broad "enhanced ionization" (2-4 eV) regions. The density plot shows clear asymmetry features in the "one-photon", "two-photon" and rescattering regions of the ion-energy spectrum. A very interesting fact to be noted here though is that the maximal asymmetries in these three regions occur at different phases. The asymmetry in the "one-photon" and "two-photon" regions appear to have nearly a π phase shift, while the asymmetry feature in the rescattering region seems roughly π out of phase with "two-photon" and in phase with "one-photon" asymmetry. The broad CREI peak centered at 3 eV is due to double ionization and thus cannot be expected to show asymmetry. However, although the CREI peak seem to extend almost all the way up to 5 eV, part of the ion yield from about 4 eV and higher is accounted for by the rescattering mechanism. Though the ion-yield due to the rescattering mechanism might not be very strong the degree of asymmetry in the yield indeed is.

5.4.1 Focussing on the low energy channels

The asymmetry in the rescattering range has been observed and studied extensively earlier by Kling et. al (ref: Kling) using few-cycle CEP locked pulses. The mechanism of asymmetry in this region is also well interpreted. Thus we focus on the low-energy asymmetry features which are observed for the first time in an energy resolved manner and are quite intriguing. We plot the asymmetry of emission of D^+ ions in the 0 to 2 eV ion-energy range in Fig 5.3 and study the variation of these features at varying laser intensities. Fig 5.4.1 shows the asymmetry plots from 0 to 2 eV range at three different intensities, 1-3 $\times$ 10^{14} W/cm^2. The major features are seen to persist through all the intensities. The sharp discontinuity in the asymmetry at an energy of 0.3 eV, thereby creating to two distinct energy regions, persists at all intensities: 0-0.3 eV (BS), and 0.3-2 eV (ATD). The lower panel on each plot shows the asymmetry integrated over these two regions: BS in red, and ATD in

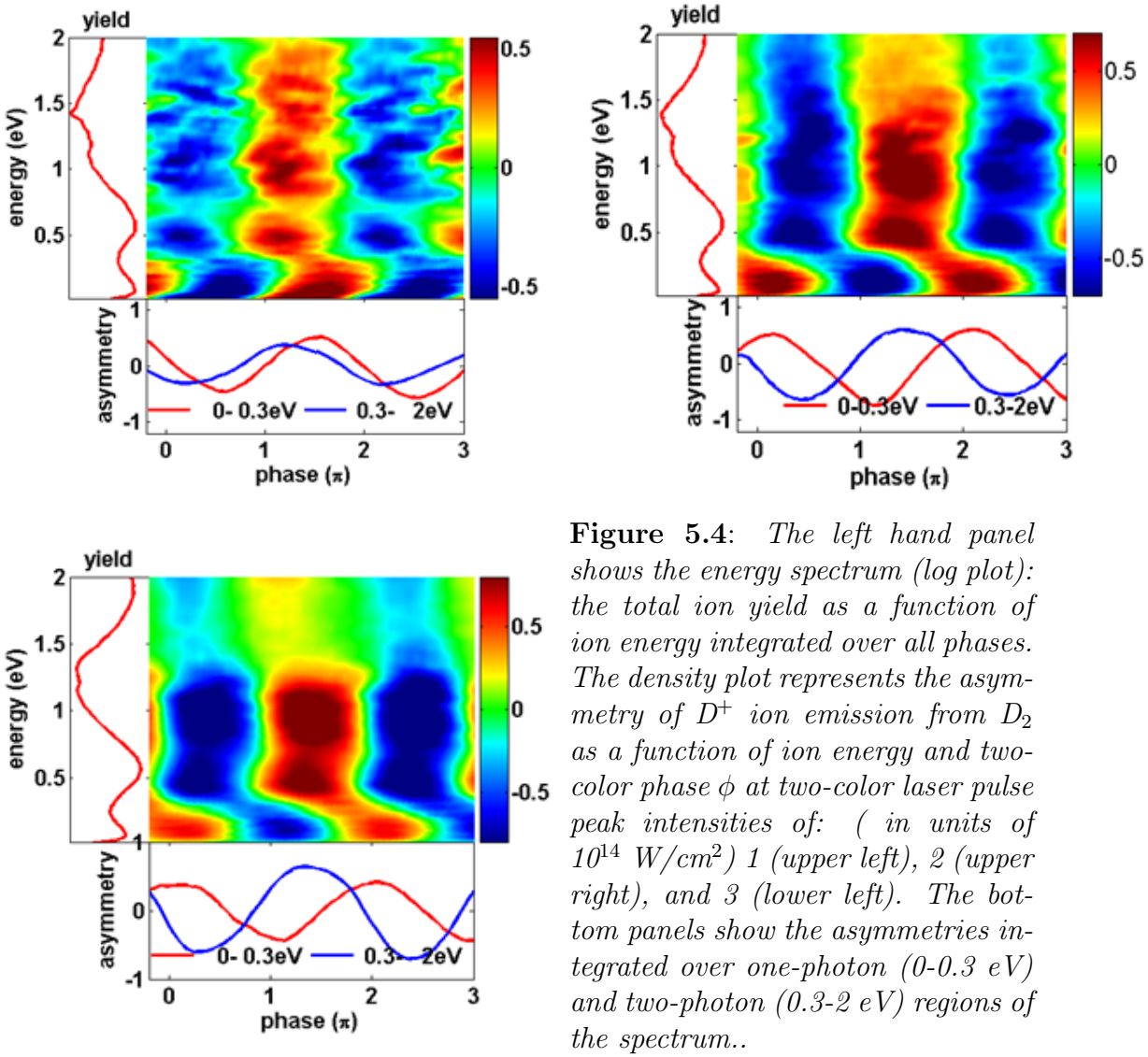

Figure 5.4: *The left hand panel shows the energy spectrum (log plot): the total ion yield as a function of ion energy integrated over all phases. The density plot represents the asymmetry of D^+ ion emission from D_2 as a function of ion energy and two-color phase ϕ at two-color laser pulse peak intensities of: (in units of 10^{14} W/cm^2) 1 (upper left), 2 (upper right), and 3 (lower left). The bottom panels show the asymmetries integrated over one-photon (0-0.3 eV) and two-photon (0.3-2 eV) regions of the spectrum..*

blue. The phase delay between the asymmetry features in the one and two-photon regions is seen to reduce with decreasing intensity, as shown in the integrated plots in the bottom panel.

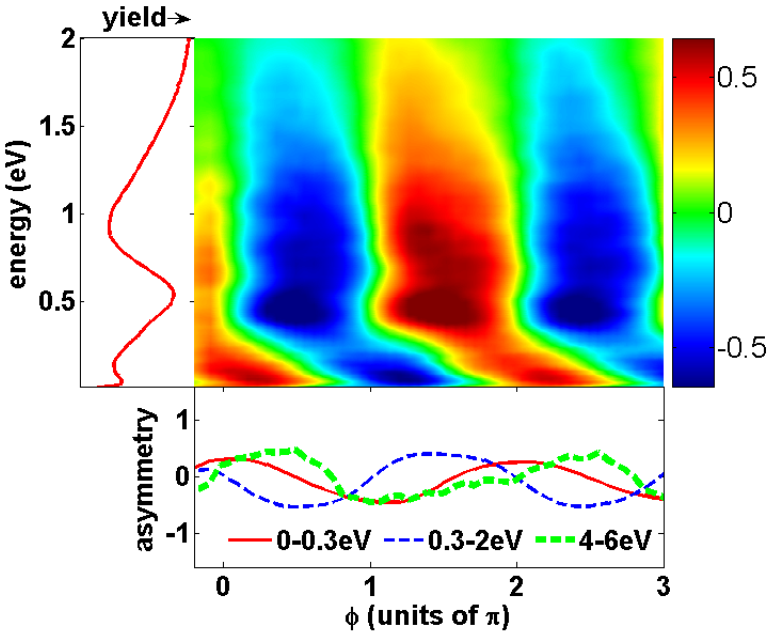

Figure 5.5: *The left hand panel shows the energy spectrum (log plot): the total ion yield as a function of ion energy with decades indicated by tick marks. The density plot represents the asymmetry of H^+ ion emission from H_2 as a function of ion energy and phase ϕ between 800 and 400 nm radiation for a laser peak intensity of $2 \times$ ^{14} W/cm^2)*

5.4.2 D^+ vs. H^+ asymmetry

H^+ ion asymmetry maps show nearly identical asymmetry to those for D^+ at all intensities, as shown in Fig 5.4.2. Intuitively one can expect the phase of the asymmetry for H^+ to be different than D^+ since the former is much lighter and the wave packet moves faster on the potential curve. But this is not observed in the data and theory also corroborates that.

5.4.3 Comparison with theory

Fig 5.4.3 shows a comparison of the low-energy part (0-2 eV) of Fig 5.3 and the theoretical calculations as described in Sec 5.2.1. The model calculation is not directly applicable to the rescattering region and that is why the comparison is kept to 0-2 eV in this figure. Apart from a slight phase shift between experiment and theory in the "two-photon region, the overall agreement is quite good. The most remarkable feature of the clear separation

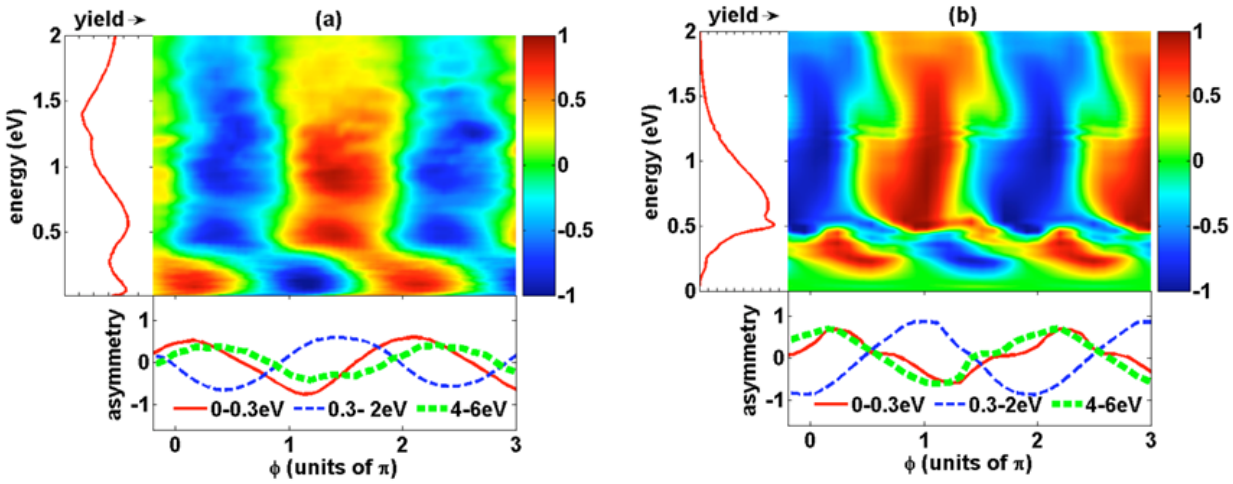

Figure 5.6: *Similar to Fig 5.3; comparison of experiment (a) and theory (b) for the one and two-photon regions of ion energy (0-2 eV). The left hand panels show log plots of the measured (calculated) energy spectrum integrated over all phases, while the bottom panels show the asymmetries integrated over one-photon (0-0.3 eV) and two-photon (0.3-2 eV) regions of the spectrum. Also shown in the bottom panels are plots measured and calculated for the rescattering region from Fig 5.3 (4-6 eV).*

between "one-photon" and "two-photon" regions remain robust in both and through all intensities. In fact, the discontinuity from the ion-energy of 0.3 to 0.4 eV is very abrupt, particularly in the theory. The phase drift of the "two-photon" with respect to "one-photon" is slightly different in the theory. Also the intensity dependence of the phase drifts between the asymmetry features of the different energy regions are somewhat more pronounced for the theoretical simulations.

5.4.4 A simple interpretation

We discuss the asymmetry features in the low-energy channels in terms of photon coupling. In order to observe asymmetry at any ion-energy the fundamental requirement is the presence of two competing pathways of dissociation resulting in both g and u dissociation at the same ion-energy. In the range of 0-0.3 eV we have already discussed the existence of the "one-photon" coupling, bond-softening, that leads to u-state ions. This alone cannot

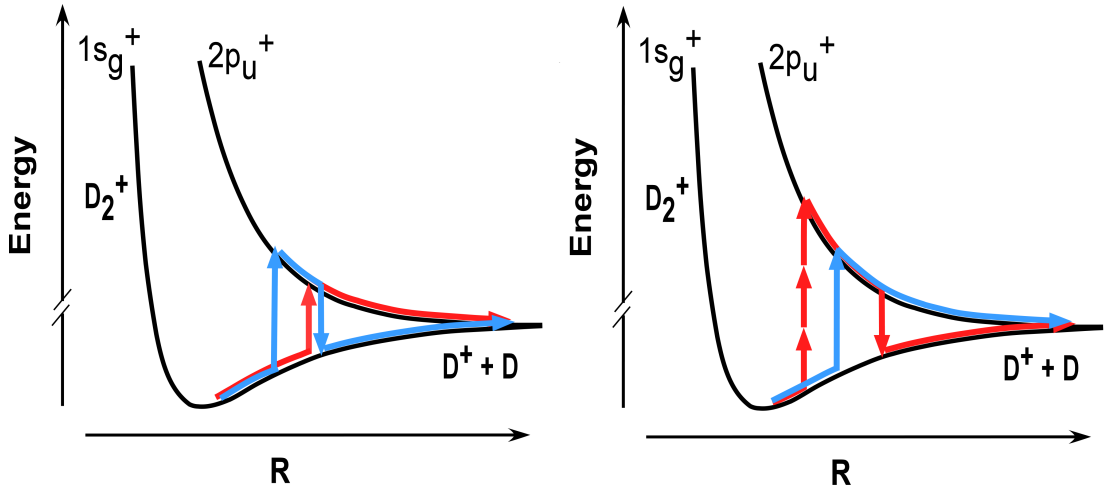

Figure 5.7: *Schematic diagram of ω and 2ω photon coupling between the $1s\sigma_g$ and $2p\sigma_u$ potentials describing two competing pathways of dissociation for each energy channel (a) BS region and (b) ATD region.*

produce asymmetry. In the presence of two-color field a second dissociation pathway can be present: the molecule can absorb one 2ω photon and then emit one ω photon and dissociate in the 1sσg channel. Both these routes produce ions with energy in the 0-0.3 eV range as shown in Fig 5.4.4 (a). Similarly, in the 0.3- 2 eV energy range (Fig 5.4.4 (b)), the "two-photon" transition creates ions in the1sσg channel: it involves the molecule absorbing three ω photons and emitting one ω photon to dissociate in the 1sσg channel. An alternative pathway producing ions in similar energy range can be thought of as a single 2ω transition and subsequent dissociation in the 2pσu channel. Since different mechanisms are involved in creating asymmetry in the two energy ranges 0-0.3 eV and 0.3-2 eV the discontinuity in the asymmetry between these two regions are understandable. Since each pathway is favored by a different relative contributions of the 800 nm and 400 nm fields, it is natural that the transition amplitudes vary differently with phase. Subsequently the asymmetry amplitudes in the two energy ranges will also vary differently and independently from each other. A simple classical argument might also be applicable to explain the phase responses in the two energy-ranges. For example, the time the nuclear wave packet takes to reach the

localization distance (near 6 a.u.) is different for these two regions and thus the location of the oscillating electron wave packet which is frozen when this distance is crossed would be expected to be different, giving rise to different asymmetries.

5.4.5 Conclusion

We have measured the asymmetry of the ion emissions in the dissociation of D_2 by a two-color field over the entire energy range of 0 to 6 eV and have found that the phase of the asymmetry is very ion-energy dependent. It is evident that the mechanisms involved in creating the interfering dissociative wavepackets in the different energy channels are very different and independent from each other. Thus the attempt to assign a general direction of overall expected D^+ ion emission, integrated over all energies, as a function of two-color phase[8,56–58] appears hopeless. To be able to predict the phase response of ion emission, a knowledge of the ion-energy and complete understanding of the dissociation mechanism involved with that energy is required.

We answer the key question posed at the very beginning: We found ion asymmetry in the low-energy channels. Also we show clearly that the ion emission direction at a given two-color phase depends on the dissociation mechanism. However we also came across some phenomena that we could not explain. These include: H_2 and D_2 show identical asymmetry responses; the relative phases of the asymmetry between different ion-energy channels are seen to vary as a function of the laser intensity.

5.5 Summary

We observe asymmetry effects in D^+ ions using a two-color pulse. The phase of the asymmetry is found to depend on the ion-energy. Part of this behavior can be attributed to the different ionization mechanisms which are involved for different ion energies. The experimental results are found to be in good agreement with the theoretical simulation. No simple

correlation between the phase of the asymmetry and the two-color phase can be established. Thus the discussion of "intuitive" direction of ion emission from molecules suggested in previous journals does not seem appropriate. The relative phase of the ion asymmetry between the "one-photon" and "two-photon" channels is seen to vary as a function of laser intensity. Finally, H^+ ions shows an identical asymmetric response to D^+.

Bibliography

[1] F. Fabre, G. Petite, P. Agostini, and M. Clement, Journal of Physics B: Atomic, Molecular and Optical Physics **15**, 1353 (1982).

[2] G. Petite, F. Fabre, P. Agostini, M. Crance, and M. Aymar, Phys. Rev. A **29**, 2677 (1984).

[3] P. Agostini, F. Fabre, G. Mainfray, G. Petite, and N. K. Rahman, Phys. Rev. Lett. **42**, 1127 (1979).

[4] A. Scrinzi, M. Geissler, and T. Brabec, Phys. Rev. Lett. **83**, 706 (1999).

[5] V. Keldysh, Sov. Phys. JETP **20**, 1307 (1965).

[6] M. V. Ammosov, N. B. Delone, and P. V. Krainov, Sov. Phys. JETP **64**, 1191 (1986).

[7] Z. Chen, A.-T. Le, T. Morishita, and C. D. Lin, Phys. Rev. A **79**, 033409 (2009).

[8] B. Sheehy, B. Walker, and L. F. DiMauro, Phys. Rev. Lett. **74**, 4799 (1995).

[9] G. G. Paulus et al., Nature **414**, 182 (2001).

[10] T. Osipov, *Experimental study of photoelectron diffraction from two-center molecules by means of the COLTRIMS technique*, PhD thesis, Kansas State University, Manhattan, Kansas, U.S.A., 2003.

[11] A. T. J. B. Eppink and D. H. Parker, Rev. Sci. Instrum. **68**, 3477 (1997).

[12] M. J. J. Vrakking, Rev. Sci. Instrum. **72**, 4084 (2001).

[13] A. S. Alnaser et al., Phys. Rev. A **70**, 023413 (2004).

[14] T. Zuo, A. D. Bandrauk, and P. B. Corkum, Chem. Phys. Lett. **259**, 313 (1996).

[15] M. Spanner, O. Smirnova, P. B. Corkum, and M. Y. Ivanov, Journal of Physics B: Atomic, Molecular and Optical Physics **37**, L243 (2004).

[16] S. X. Hu and L. A. Collins, Phys. Rev. Lett. **94**, 073004 (2005).

[17] M. Lein, J. P. Marangos, and P. L. Knight, Phys. Rev. A **66**, 051404 (2002).

[18] S. N. Yurchenko, S. Patchkovskii, I. V. Litvinyuk, P. B. Corkum, and G. L. Yudin, Phys. Rev. Lett. **93**, 223003 (2004).

[19] G. G. Paulus, W. Nicklich, H. Xu, P. Lambropoulos, and H. Walther, Phys. Rev. Lett. **72**, 2851 (1994).

[20] G. G. Paulus, W. Becker, W. Nicklich, and H. Walther, Journal of Physics B: Atomic, Molecular and Optical Physics **27**, L703 (1994).

[21] D. N. Fittinghoff, P. R. Bolton, B. Chang, and K. C. Kulander, Phys. Rev. Lett. **69**, 2642 (1992).

[22] K. J. Schafer, B. Yang, L. F. DiMauro, and K. C. Kulander, Phys. Rev. Lett. **70**, 1599 (1993).

[23] B. Sheehy et al., Phys. Rev. A **58**, 3942 (1998).

[24] G. L. Yudin and M. Y. Ivanov, Phys. Rev. A **63**, 033404 (2001).

[25] H. Niikura et al., Nature (London) **417**, 917 (2002).

[26] A. L'Huillier and P. Balcou, Phys. Rev. Lett. **70**, 774 (1993).

[27] J. J. Macklin, J. D. Kmetec, and C. L. Gordon, Phys. Rev. Lett. **70**, 766 (1993).

[28] M. Lewenstein, P. Balcou, M. Y. Ivanov, A. L'Huillier, and P. B. Corkum, Phys. Rev. A **49**, 2117 (1994).

[29] P. B. Corkum, Phys. Rev. Lett. **71**, 1994 (1993).

[30] T. Morishita, A.-T. Le, Z. Chen, and C. D. Lin, Phys. Rev. Lett. **100**, 013903 (2008).

[31] D. Ray et al., Phys. Rev. Lett. **100**, 143002 (2008).

[32] B. Yang et al., Phys. Rev. Lett. **71**, 3770 (1993).

[33] W. Becker, A. Lohr, and M. Kleber, Journal of Physics B: Atomic, Molecular and Optical Physics **27**, L325 (1994).

[34] G. G. Paulus, W. Becker, and H. Walther, Phys. Rev. A **52**, 4043 (1995).

[35] M. P. Hertlein, P. H. Bucksbaum, and H. G. Muller, Journal of Physics B: Atomic, Molecular and Optical Physics **30**, L197 (1997).

[36] G. G. Paulus et al., Phys. Rev. Lett. **80**, 484 (1998).

[37] M. J. Nandor, M. A. Walker, and L. D. V. Woerkom, Journal of Physics B: Atomic, Molecular and Optical Physics **31**, 4617 (1998).

[38] J. Z. Kamin-acuteski and F. Ehlotzky, Phys. Rev. A **55**, 4625 (1997).

[39] J. Zhang et al., Journal of Physics B: Atomic, Molecular and Optical Physics **35**, 4809 (2002).

[40] M. B. Gaarde et al., Phys. Rev. Lett. **84**, 2822 (2000).

[41] F. Grasbon et al., Phys. Rev. Lett. **91**, 173003 (2003).

[42] T. Morishita, A.-T. Le, Z. Chen, and C. D. Lin, New Journal of Physics **10**, 025011 (2008).

[43] E. Rutherford, Philosopical Magazine **21**, 669 (1911).

[44] C. Liao et al., Phys. Rev. A **59**, 2773 (1999).

[45] X. M. Tong and C. D. Lin, Journal of Physics B: Atomic, Molecular and Optical Physics **38**, 2593 (2005).

[46] R. H. Garvey, C. H. Jackman, and A. E. S. Green, Phys. Rev. A **12**, 1144 (1975).

[47] S. Micheau et al., Phys. Rev. Lett. **102**, 073001 (2009).

[48] D. B. Milošević, G. G. Paulus, and W. Becker, Phys. Rev. Lett. **89**, 153001 (2002).

[49] M. F. Kling et al., Science **312**, 246 (2006).

[50] S. Watanabe, K. Kondo, Y. Nabekawa, A. Sagisaka, and Y. Kobayashi, Phys. Rev. Lett. **73**, 2692 (1994).

[51] D. Ray et al., Phys. Rev. Lett. **103**, 223201 (2009).

[52] B. Moser and G. N. Gibson, Phys. Rev. A **80**, 041402 (2009).

[53] K. P. Singh et al., Phys. Rev. Lett. **104**, 023001 (2010).

[54] S. De et al., Phys. Rev. Lett. **103**, 153002 (2009).

[55] D. W. Schumacher, F. Weihe, H. G. Muller, and P. H. Bucksbaum, Phys. Rev. Lett. **73**, 1344 (1994).

[56] M. R. Thompson et al., Journal of Physics B: Atomic, Molecular and Optical Physics **30**, 5755 (1997).

[57] E. Charron, A. G. Suzor, and F. H. Mies, J. Chem. Phys. **103**, 7359 (1995).

[58] J. H. Posthumus, M. R. Thompson, A. J. Giles, and K. Codling, Phys. Rev. A **54**, 955 (1996).

[59] V. Roudnev and B. D. Esry, Phys. Rev. A **76**, 023403 (2007).

[60] X. M. Tong and C. D. Lin, Phys. Rev. Lett. **98**, 123002 (2007).

[61] A. S. Alnaser et al., Phys. Rev. A **72**, 030702 (2005).

[62] I. A. Bocharova et al., Phys. Rev. A **77**, 053407 (2008).

[63] A. D. Bandrauk and S. Chelkowski, Phys. Rev. Lett. **84**, 3562 (2000).

[64] T. D. G. Walsh et al., Phys. Rev. A **58**, 3922 (1998).

[65] A. Zavriyev, P. H. Bucksbaum, H. G. Muller, and D. W. Schumacher, Phys. Rev. A **42**, 5500 (1990).

[66] T. Zuo and A. D. Bandrauk, Phys. Rev. A **52**, R2511 (1995).

[67] A. D. Bandrauk, Comments At. Mol. Phys **1**, 97 (1999).

[68] H. Niikura et al., Nature (London) **421**, 826 (2003).

[69] S. Chelkowski, M. Zamojski, and A. D. Bandrauk, Phys. Rev. A **63**, 023409 (2001).

[70] M. Born and R. Oppenheimer, Ann. Physik **84**, 457 (1927).

[71] M. Magrakvelidze, F. He, T. Niederhausen, I. V. Litvinyuk, and U. Thumm, Phys. Rev. A **79**, 033410 (2009).

[72] T. Niederhausen and U. Thumm, Phys. Rev. A **77**, 013407 (2008).

[73] F. He, C. Ruiz, and A. Becker, Phys. Rev. Lett. **99**, 083002 (2007).

[74] F. He, A. Becker, and U. Thumm, Phys. Rev. Lett. **101**, 213002 (2008).

Appendix A

Intensity calibration

An estimation of the laser peak intensity is vital for the experimental studies discussed. There are several possible methods of calibrating the intensity. A discrepancy between the estimation reached by these different methods has been an open ended problem for a long time in this lab. I have attempted to revisit this issue, and systematically compare the intensities estimated by the different methods. We hope to get a better understanding of the limitations in the different methods therefore giving us a clear idea as to which method gives the answer closest to the real intensity.

We calibrate the peak intensity of the laser pulse by three different procedures: (i) From first principles using the equation given in Sec 2.5. (ii) Assigning intensities by comparison of branching ratios of different fragmentation channels of D^+ (or H^+) ions to similar analysis done previously. Fig A.1 shows time-of-flight spectra of H_2 at different laser peak intensities where the intensities have been determined by comparison with theory. We compare the branching ratios from our experimental spectra to that in Fig A.1 to estimate the intensities. (iii) From energy spectra of photoelectrons from atomic or molecular targets the $10U_p$ cut-off can be estimated. The intensity can then be derived knowing the relation $U_p = I/4\omega^2$. The intensities found by the two 'atomic' methods using the VMI is shown in Fig A.3. The momentum spectra of D^+ ions taken in VMI are shown in Fig A.2. We assign a peak intensity to each dataset by comparison of the branching ratios of different fragmentation channels in each dataset to the same from the plots in Fig A.1. The total DC power of

the laser is linearly proportional to the laser intensity, so the straight line plot for power vs. intensity (Fig A.3) from the 'D^+ ion branching ratio' plot is expected. The intensities calculated from Xe cutoff are however seen to not follow a linear relation with the DC power. This can be due to the saturation effects.

Similar calibration is done for data taken in the phasemeter as shown in Fig A.4. The intensities calculated from the first principle are also plotted here.

When we assume a Gaussian profile to calculate the peak intensity as discussed in Sec 2.5, it needs to be kept in mind that it is absolutely the best possible condition on can ever achieve in experiments. In practice that is rarely achieved. One can thus always expect the first principles calculation to be high, indicative of the maximum peak intensity achievable for the corresponding DC power. This is seen to hold true in Fig A.4. Also by first principles we are calculating the 'peak' intensity. In experiments, however the gas volume is interacting with a range of intensities present on the beam profile and the ionization contribution is maximum from an intensity lower than the peak intensity. All calibrations from experiment thus will predict a lower intensity due to this volume effect.

From all the systematic comparison shown in the plots, we conclude that the intensities predicted by the D^+ ion fragmentation branching ratio predicts the intensities closest to the real 'effective intensities' in the experiment.

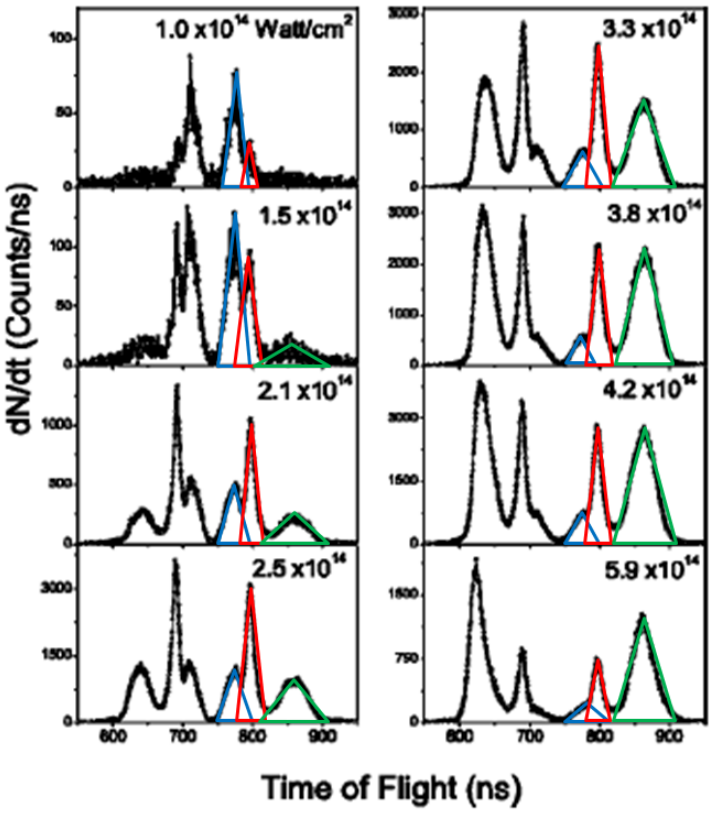

Figure A.1: *Time-of-flight spectra of H_2 at different laser peak intensities. The branching ratios of the different fragmentation channels are sensitive to laser peak intensities. The plots are used to assign intensities to the D^+ ion spectra shown in Fig A.2.*

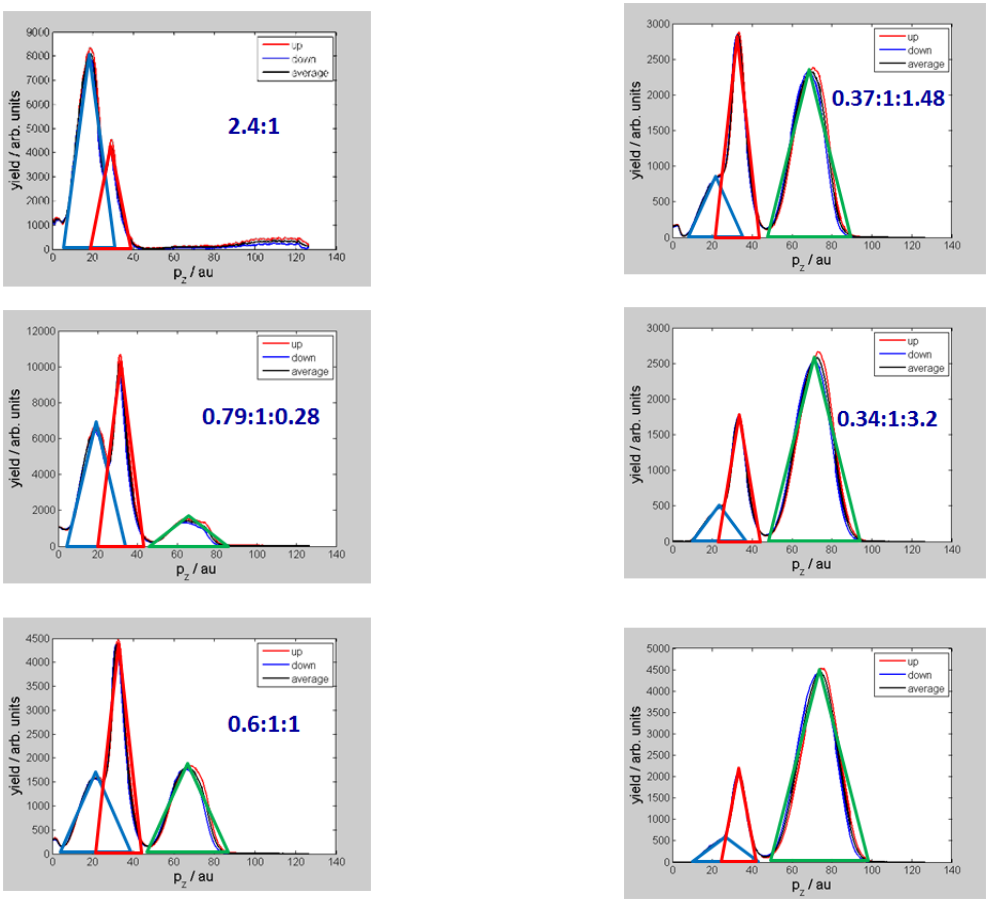

Figure A.2: *Momentum spectra of D^+ ion at different laser intensities. The ratio of area under each peak, BS(blue):ATD(red):CREI(green), is calculated. The branching ratios of different fragmentation channels are established to be a function of laser peak intensity.*

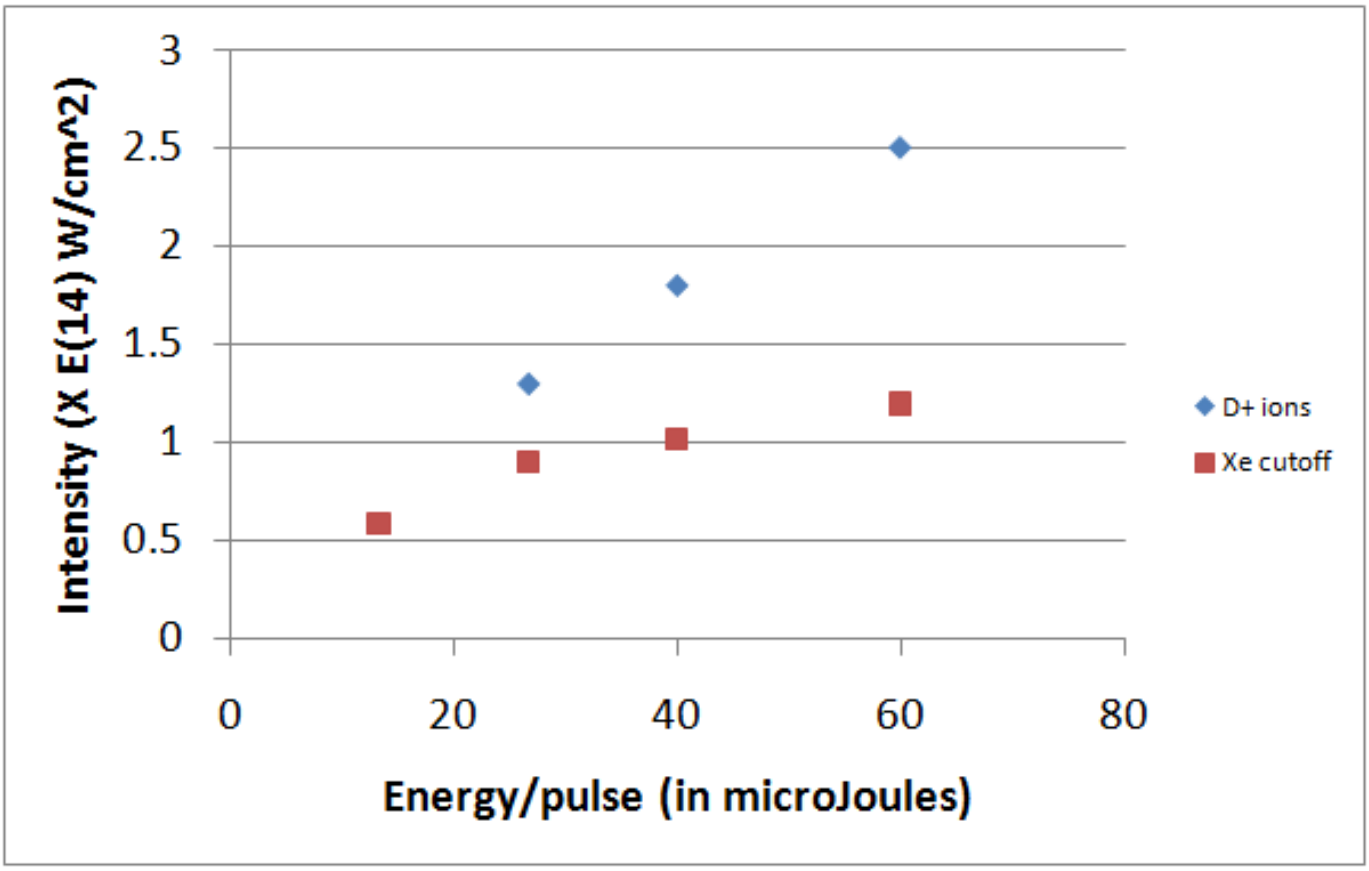

Figure A.3: *Intensity calibration is done experimentally measuring: (i) the photoelectron energy spectra from atomic targets (Xe and Ne) at different intensities and estimating the intensity from the energy cutoff, and (ii) the relative ion yield via BS, ATD and CREI channels from D^+ ions at different intensities. The intensities calculated from first principle are not shown.*

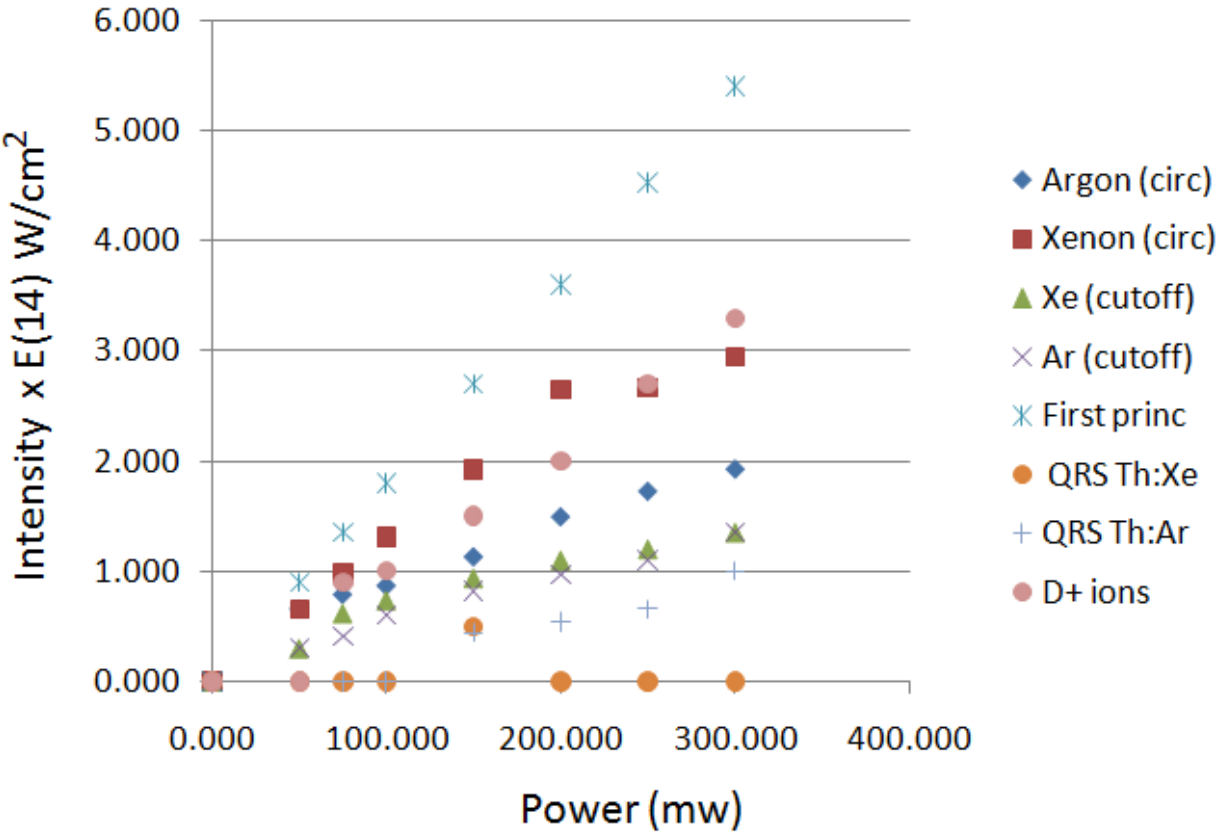

Figure A.4: *Intensity calibration is done by experimentally measuring: (i) the photoelectron energy spectra from atomic targets (Xe and Ne) at different intensities and estimating the intensity from the energy cutoff, and (ii) the relative ion yield via BS, ATD and CREI channels from D^+ ions at different intensities, and also (iv) separation of symmetric peak created by donut shaped electron emission from circularly polarized laser field at different intensities. Intensities calculated from first principle are also plotted.*